Spin Dependent Transport in Continuous and Discontinuous CoFeB/MgO Heterostructures

PhD Thesis in Physics

by

Khalid Mehmood Bhutta

Fakultät für Physik

Universität Bielefeld

September 24, 2009

Declaration

I declare that this thesis was written by me and used none other than the indicated sources.

Bielefeld, September 24, 2009

(Khalid Mehmood Bhutta)

Reviewers:

Prof. Dr. Günter Reiss

Prof. Dr. Armin Gölzhäuser

Date of submission: September 24, 2009

Abstract

This thesis is devoted to the study of spin dependent transport between CoFeB electrodes through an MgO barrier in ordered and disordered multilayer systems. The local electrical integrity of the MgO barrier was studied using Ru and CoFeB bottom electrodes by a modified conducting atomic force microscopy. The quality of the MgO barrier was characterized by measuring the hotspot density and using a statistical model proposed by F. Bardou for different thicknesses of MgO. This model studied the variations in tunneling transmission due to inhomogeneity of the barrier. The results show a decrease of the density of the hotspots with the thickness of MgO barrier and that a perfectly insulating barrier is obtained at 1 nm thickness. For the study of the disordered systems, discontinuous multilayers of CoFeB/MgO were prepared by sequential sputtering of CoFeB and MgO from the individual targets. The granular tunneling magnetoresistance (g-TMR) and transport properties were studied between 1.25 K and 330 K. The transport of charge between CoFeB in this system was dominated by hopping processes which obeyed different tunneling laws in different temperature regions. The enhanced g-TMR value observed at low temperature was attributed to higher order tunneling. The study also focused on the variations in g-TMR, electrical resistivity and microstructures by post deposition annealing. The magnetic properties of this system were also investigated between 5 K and 350 K. A superparamagnetic transition was found with a blocking temperature of 130 K.

Contents

Chapter 1

Introduction

Spintronics is the study of phenomena related to the spin of electrons and of devices that take advantage of the spin of the electron along with its charge. In conventional electronic devices the spin of the electron has been ignored and these devices relied only on the transport of electrical charge carriers. Spintronics is a newly emerging technology in which the spin of electrons along with their charge is manipulated to fabricate novel devices like magnetic sensors, MRAM and read heads for the hard disk. In these devices spin dependent effects arise by the interaction of the spin of electrons with the magnetic moments of the materials. Nonvolatile nature, increased data processing speed, decreased electric power consumption and increased integration densities are the advantages of spintronics devices over the conventional semi-conductor devices. These advantages make the spintronics devices attractive for high density memory storage devices and magnetic sensors applications.

Several experimental groups at different universities and in electronic industry are involved in the study of new spintronics materials and geometry for the application purposes. A number of examples for the application of these devices can be quoted here. One of them are hard disks, where the magnetoresistive read heads convert information stored in high density recording media by a small magnetic stray field into electrical signal with a high spatial resolution [1, 2, 3]. Another example is the combination of tunnel magnetoresistance elements in read heads with perpendicular recording which steeply increases the storage density [4]. Magnetic random access memory (MRAM), magnetic field sensors, lab-on-chip and reconfigurable magnetic logic are a few examples among a number of novel spintronics

devices.

In 1988, the group of Peter Grünberg and Albert Fert discovered the Giant Magnetoresistance effect in Fe/Cr trilayers and multilayers by resistivity measurement [5, 6]. The GMR effect is due to the spin dependent scattering of conduction electrons in the vicinity of the interface of magnetic and nonmagnetic spacer layers. Due to the large magnetoresistance value compared to the usual anisotropic magnetoresistance (AMR) this effect is refered as giant magnetoresistance. The discovery of the GMR effect was a great breakthrough in the field of spin dependent transport and thin film magnetism. Because of their large effect and sensitivity to a small magnetic field, GMR based sensors have replaced the AMR based read heads in hard drives and also found their applications in cars for monitoring of rotation of wheels, current monitors and velocity and acceleration measuring sensors [7, 8, 9]. Peter Grünberg and Albert Fert both were awarded the Nobel Prize of 2007 in Physics for their discovery.

In 1992, two groups in USA also observed the GMR effect in granular systems of ultrafine ferromagnetic particles dispersed in non-magnetic matrix [10, 11]. The individual particles in the granular systems are either not free but are coupled with each other or have a large anisotropy so they are magnetically hard. Due to this magnetic hardness, a large magnetic field is required to achieve the saturation magnetization of these particles. This feature makes the technical applications of granular systems limited.

Julliere had already discovered tunneling magnetoresistance (TMR) effect in tunnel junctions in which two ferromagnetic layers were separated by a thin insulating layer [12]. The TMR effect was due to the spin dependent tunneling of electrons from one ferromagnetic layer to an other through an insulating barrier. This effect has been extensively studied in Al_2O_3 based MTJs since the discovery of room temperature TMR effect [13, 14]. In these MTJs a TMR ratio up to 70% has been experimentally achieved at room temperature [15].

Like the GMR effect, the TMR effect is also observed in granular systems (disordered system) of magnetic particles (Co, Fe, Ni) embedded in insulating matrices (Al_2O_3, SiO_2 and MgO). The applications of granular films include high coercive films for information storage, high permeability and high resistivity films for shielding and bit writing at high frequencies [16, 17, 18].

The biggest breakthrough during the last five years was the discovery that the spin polarization of the tunnel current depends not only on the electronic properties of the magnetic layers but is also influenced by the choice of the material of barrier layer [19, 20]. By changing the barrier material from a thin amorphous layer of aluminum oxide (Al_2O_3) to a crystalline layer of magnesium oxide (MgO), the degree of spin polarization of the current increases from 50% to 90% for the same magnetic electrode material (CoFe). Therefore, the TMR value correspondingly increases from 70% to 500% at room temperature [1, 21].

In recent years, therefore, Al_2O_3 barrier has been replaced by MgO because of the following reasons:

1) Al_2O_3 based MTJs have not been free from unwanted factors like electrode barrier interface roughness, incomplete or excessive oxidation of Al which result in remaining Al or oxidation of the underlying ferromagnetic electrode [22, 23]. These factors reduce the TMR ratio. On the other hand, such problems are not faced in the case of MgO because of e.g., direct sputtering of MgO from a target.

2) MgO based tunnel junctions are more reliable than Al_2O_3 based tunnel junction because the MgO tunnel barriers are more hydrogen tolerant than Al_2O_3 tunnel barriers. Furthermore, MgO tunnel barriers have ten years longer life time than Al_2O_3 tunnel barriers [24].

3) The ultrahigh TMR value in MgO based MTJs is due to coherent tunneling of electrons through the MgO barrier. However, the tunneling of electrons through Al_2O_3 barrier is not (completely) coherent.

The high TMR value in MgO based MTJs encouraged the industry to replace spin valve field sensing devices by MTJs devices. The Al_2O_3 barrier should be only nonconductive and free from pinholes for the realization of high TMR value. However, the MgO barrier needs to be crystallized in a certain crystal orientation. This is required for occurrence of coherent tunneling processes necessary for an ultrahigh TMR value. This crystal orientation is obtained by tight control of deposition conditions and annealing parameters. Therefore, the study of MgO barrier in tunneling processes is an important area of research in these days.

The study of spin dependent transport through MgO barrier in continuous and discontin-

uous CoFeB/MgO heterogenuous structures is the main goal of this thesis. For this purpose a continuous layers structure of CoFeB/MgO has been prepared and studied by conducting atomic force microscopy and the results have been compared to the properties of magnetic tunnel junctions. For discontinuous CoFeB/MgO heteroguous structures a granular system of CoFeB/MgO has been studied. The transport through MgO was studied under different annealing conditions and at different temperatures.

This thesis is organised as follow: The second chapter includes the basics of ferromagnetism and spin dependent transport phenomenon. The tunneling of electrons is discussed in ordered system of magnetic/non-magnetic metallic multilayers and disordered system of discontinuous multilayers. The role of the barrier in coherent tunneling is also included in this chapter. In the third chapter a short introduction of experimental methods and techniques used in this thesis are given. This includes the fabrication of samples and characterization tools. In order to address certain physical questions prevailed at the beginning of this investigation the structure of MgO barriers is studied by conducting atomic force microscopy (CAFM) in the forth chapter. Initially, Ru under the barrier is used to investigate the electrical integrity of the MgO tunnel barrier. For the comparison of results with ordered systems like magnetic tunnel junctions, half finished magnetic tunnel junctions with different thicknesses of the MgO barrier are also investigated. The fifth chapter is meant for the study of disordered system. To study the role of CoFeB and MgO barrier in disordered system, a granular system of CoFeB/MgO has been prepared and investigated. Different thicknesses of MgO and CoFeB were investigated to optimize the spin dependent transport in this system. Spin dependent transport in connection with the tunneling laws have also been included. The role of the barrier in connection with crystallization is a part of this chapter.

Chapter 2

Theoretical Background

In this chapter different theories related with this work will be discussed which will be helpful to understand the work done in this thesis. It will start with a small introduction of ferromagnetism and spin dependent transport phenomena in magnetic materials. A detail of the spin dependent transport in heterogenuous systems in special references with ordered and disordered system will be discussed.

2.1 Ferromagnetism

Magnetic materials exhibit a bulk magnetization due to the interaction of magnetic moments among individual atoms and/or ions. This interaction tends to align or anti-align the magnetic moments of the atoms. If the magnetic moments are aligned with each other the material is called ferromagnetic material. Thermal excitations try to randomize the alignment of the magnetic moments. The temperature at which these thermal excitations overcome the alignment of the magnetic moments is called Curie temperature T_c.

The origins of the magnetic moment of an atom are the orbital and spin magnetic moments of its electrons; the magnitude of the magnetic moment depends on the number and elecrtonic states of electrons in the atom. All free atoms have net magnetic moments if their sub shells are not fully occupied. However, ferromagnetism is found rarely in nature because most of the atoms lose their net magnetic moments when integrated into a solid [25]. In a solid, electrons are delocalized because of the overlapping of their wave functions with the

neighboring atoms. This is one of the main reasons for the loss of magnetization in a solid. However, according to Heisenberg's model, the wave function of electrons in neighboring atoms should only slightly overlap each other for ferromagnetism to exist [26]. Furthermore, the symmetry of the potential acting on an electron due to the neighboring atoms in a solid is lower than that in an atom. The reduction in potential symmetry of electrons is another reason of the loss of magnetization in solids. Other than that the coupling between the magnetic moments of individual atoms is also very important for the magnetization. This coupling depends on the type of bonds and atomic distances [27].

Ferromagnetism exists only for the middle part of the 3d-elements (e.g., Co, Fe, and Ni) and for Gd and Dy. The electronic band structure for these elements is complicated. In these ferromagnets the electrons with different spins populate the band structure differently due to the exchange splitting. Fig. 2.1 shows the schematic representation of the band structure of a normal metal and a ferromagnetic metal. In the normal metals both bands have equal numbers of spin up and spin down electrons. In ferromagnetic metals, however, the two separate bands are shifted in the energy with respect to each other. This shift is called exchange energy and gives rise to unequal filling of bands and acts as a source of net magnetic moment.

The magnetization and spin polarization of a ferromagnetic material can be found from its band structure because both are determined by the density of spin up and spin down electrons and given by the following relations

$$M \propto (N_{\uparrow} - N_{\downarrow}) \tag{2.1.1}$$

$$M \propto \frac{(N_{\uparrow} - N_{\downarrow})}{(N_{\uparrow} + N_{\downarrow})} \tag{2.1.2}$$

Where $N_{\uparrow}$ and $N_{\downarrow}$ are the densities of electrons with spin up and down, respectively. The magnetization, structure, spin polarization and Curie temperature of ferromagnetic elements are given in the table

Element	Structure	T_c(K)	M_s(emu/cc)	Spin Polarization(%)
Fe	bcc	1044	1719	44
Co	hcp	1388	1400	45
Ni	fcc	628	509	33

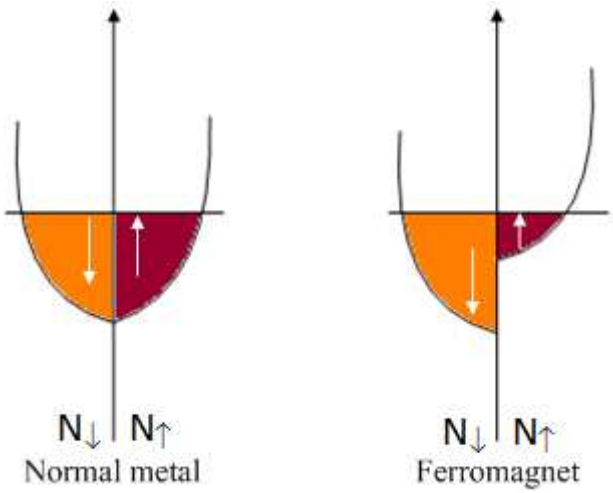

Fig. 2.1: A schematic representation of the band structure of a normal metal and a ferromagnetic metal. In ferromagnetic metal the minority spin band is shifted upwards by the exchange energy. [28].

2.2 Spin Dependent Transport

Electrons are spin-1/2 fermions and therefore they constitute a two states system with spin up and spin down. A transport phenomenon which manipulates or uses the spin of the electron is a spin dependent transport phenomenon. The spin dependent transport can occur only in those materials for which there is an unequal population of spin at the Fermi level [28]. We know that the ferromagnetic materials have two separate bands for spin up and spin down electrons in the DOS at the Fermi level. These bands are shifted in the energy with respect to each other as shown in Fig. 2.1. This shift gives rise to unequal filling of the bands and causes a net spin polarization. Therefore, ferromagnetic materials show spin dependent transport.

The change in the electrical resistance of a normal or magnetic metal by an applied external magnetic field was first observed by William Thomson in 1856-57 [29]. This change is referred to as magnetoresistance. The magnetoresistance is said to be positive if it increases or negative if it decreases with the external magnetic field. The reason of the magnetoresistance in normal metals is the Lorentz force which the magnetic field exerts on moving electrons. The value of this magnetoresistance is relatively small and referred to as ordinary

magnetoresistance (OMR). However, a large value of magnetoresistance is obtained in ferromagnetic materials due to the spin polarization of the electrons in the presence of an external magnetic field.

Since long the spin of electron has not been intensively investigated by the experimentalist and researchers in the transport phenomena. In 1971, Tedrow and Meservey conducted series of tunneling experiments using a Al_2O_3 barrier between a very thin superconducting and ferromagnetic films in a high magnetic field and showed that tunneling is spin dependent [30, 31]. The spin dependent splitting of the quasi particle density of states in a superconductor by the application of magnetic field has been used to analyze the spin polarization of the tunneling current for ferromagnetic films [32, 33].

Three different types of magnetoresistance have been observed in magnetic materials: AMR (Anisotropic Magnetoresistance), GMR (Giant Magnetoresistance) and TMR (Tunneling Magnetoresistance).

2.3 Spin Dependent Transport in Bulk Materials

A sizable MR was observed in bulk ferromagnetic metals (Co, Fe, Ni) and alloys (permalloys) at room temperature in 1970s. The MR depends on the direction of the spontaneous magnetization and is due to the change of magnetization under the external field. This magnetoresistance is referred to as Anisotropic Magnetoresistance (AMR) [34]. The resistivity is maximum when the current is parallel to the magnetization direction, $\rho_{||}$, and it is minimum when the current is perpendicular to the magnetization direction, $\rho_{\perp}$,. This is due to the scattering produced by the spin-orbit interaction. The electrons which travel parallel to the magnetization scatter stronger than those which travel perpendicular to the magnetization. The definition of AMR is given by:

$$AMR(\%) = \frac{\rho_{||} - \rho_{\perp}}{\rho_{\perp}} \times 100 \tag{2.3.1}$$

Although the relative change in the resistivity due to AMR is small, i.e., only 2% - 4% in permalloys, it has very important technical applications in the field of magnetic sensors [34]. These are used as speed/position sensors and read head sensors for magnetic storage

devices.

2.4 Spin Dependent Transport in Ordered Systems

A highly sensitive read head with a large MR ratio is required for ultrahigh density recording media. Therefore, a large MR effect at room temperature is highly desirable for technical applications. Two kinds of magnetoresistance effects have been observed in ordered multilayers systems. These are the Giant Magnetoresistance (GMR) and the Tunneling Magnetoresistance (TMR) which are explained in the following paragraphs.

2.4.1 Giant Magnetoresistance

A huge magnetoresistance in Fe/Cr multilayers system was found by Biabich et.al., (group of A. Fert) and Binasch et.al., (group of P. Grünberg) in 1988 [6, 5]. The value of this magnetoresistance is 50% at room temperature. However, a much larger value up to 220% at 1.5 K has been observed in this system [35]. Due to its large value, it is referred to as Giant Magnetoresistance (GMR). Such a large value cannot be expected from the normal magnetoresistance caused by Lorentz forces or from the anisotropic magnetoresistance caused by the spin orbit interaction. Fe/Cr multilayer systems exhibit an antiferromagnetic coupling between two ferromagnetic Fe-layers through a nonmagnetic chromium interlayer. Therefore, at zero magnetic field the Fe layers are aligned antiparallel to each other and the resistance is very high. When a magnetic field is applied, the alignment of the Fe layers changes from antiparallel to parallel and the resistance drops significantly. The GMR amplitude is defined by:

$$GMR(\%) = \frac{R_{AP} - R_P}{R_P} \times 100 \tag{2.4.1}$$

Where R_{AP} is the resistance for antiparallel alignment of the adjacent ferromagnetic layers and R_P is the resistance for parallel alignment. The Fig. 2.2 represents the change in resistance due to magnetic field in Fe/Cr multilayer systems with different number of Fe/Cr bi-layers at 4.2K. The relative orientation of field has also been depicted in the figure.

The origin of the GMR is the scattering of the conduction electrons due to the relative

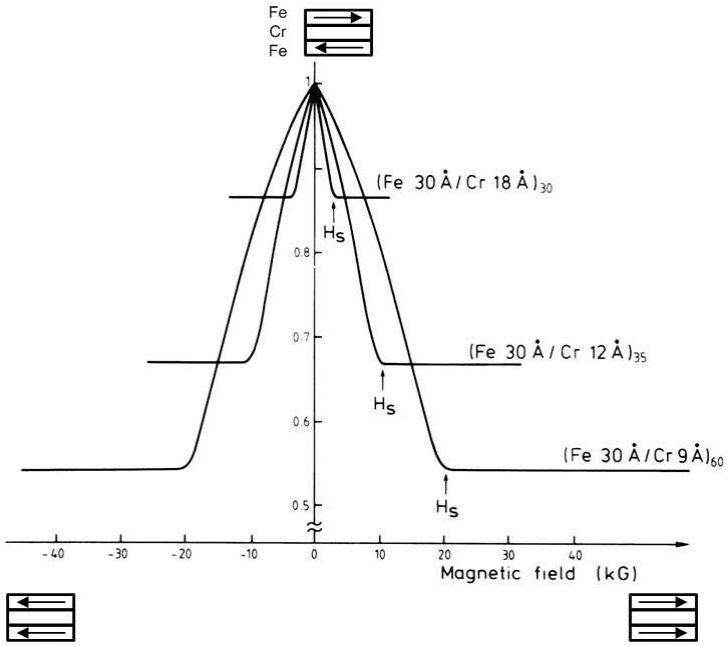

Fig. 2.2: GMR of Fe/Cr multilayer system when current and magnetic field are in same plane. The change in resistance is due to the orientation of Fe layers by the applied magnetic field [6]

alignment of the magnetic layers. The scattering of the electrons is larger in case of antiparallel alignment than in case of parallel alignment of magnetization. The electrical transport in the layers can be divided in two spin-channels. Electrons with their spin opposite to the local magnetization direction experience more scattering and thus higher resistance than electrons with their spin parallel to the magnetization. In case of parallel magnetizations, one current channel acts as a shunting current but in case of antiparallel magnetization both channels suffer high resistance.

This effect has also been observed in variety of other multilayer systems e.g., Co/Cu, Ni/Ag and Fe/Cu [36, 37, 38, 39, 40, 41]. As explained earlier, this effect is observed in those multilayer systems in which there is antiferromagnetic arrangement of the magnetizations. This arrangement can be achieved by different ways such as pinning of one ferromagnetic layer or by using layers having different coercivities. The antiparallel alignment in trilayers is achieved by pinning of one the ferromagnetic layers' magnetization by the "exchange bias" effect. The other ferromagnetic layer's magnetization is kept free to rotate with an

external applied field [42]. Such a trilayer system is often referred to as a spin-valve. The antiparallel alignment can also be achieved by using multilayers in which consecutive layers have different coercivities [43]. In 1992, it was proven that this effect is not limited to only multilayers systems, the magnetic clusters in a nonmagnetic matrix or combination of layers and clusters also display the GMR effect due to a non-parallel magnetization in the ground state [35, 36].

2.4.2 Tunneling Magnetoresistance

The tunneling magnetoresistance was first observed by Julliere in 1975 but at that time it was not possible to have a reproducible effect at room temperature [12]. In 1995, Moodera et al. at MIT and Miyazaki and Tezuka in Sendai found a reproducible large TMR value at room temperature using an amorphous AlO_x barrier [13, 14]. This tunneling magnetoresistance is obtained when the current flows in a magnetic tunnel junction (MTJ). A simple MTJ includes two ferromagnetic layers of different coercivities separated by a thin insulating barrier. The magnetization of one of the ferromagnetic layers is hard and that of other is kept soft. The resistance of the MTJ is low or high depending on the relative orientation of the soft layer's magnetization (parallel or anti-parallel) with respect to the hard layer. The magnetization of the soft layer can be made parallel or anti-parallel to the hard layer by the application of a magnetic field. By applying a magnetic field, the change in the relative orientation of the two ferromagnetic layers' magnetization having different coercivities can be explained as follow:

Starting at high negative magnetic field the magnetization of both layers are parallel in the field direction and the resistance is $R = R_{\uparrow\uparrow}$. Upon increasing field, the magnetization of the soft layer reaches it saturation and switches to anti parallel alignment and the resistance increases to $R = R_{\uparrow\downarrow}$. Further increase in the field results in a switching of the hard layer and the resistance drops to its original value. Now on decreasing the field, the same is repeated in reverse direction as shown in the Fig. 2.3. The TMR ratio is defined by:

$$TMR(\%) = \frac{R_{\uparrow\downarrow} - R_{\uparrow\uparrow}}{R_{\uparrow\uparrow}} \times 100 \tag{2.4.2}$$

where $R_{\uparrow\downarrow}$ is the resistance when the soft and the hard layers are antiparallel to each other and $R_{\uparrow\uparrow}$ is the resistance when the soft and the hard layers are parallel to each other. The

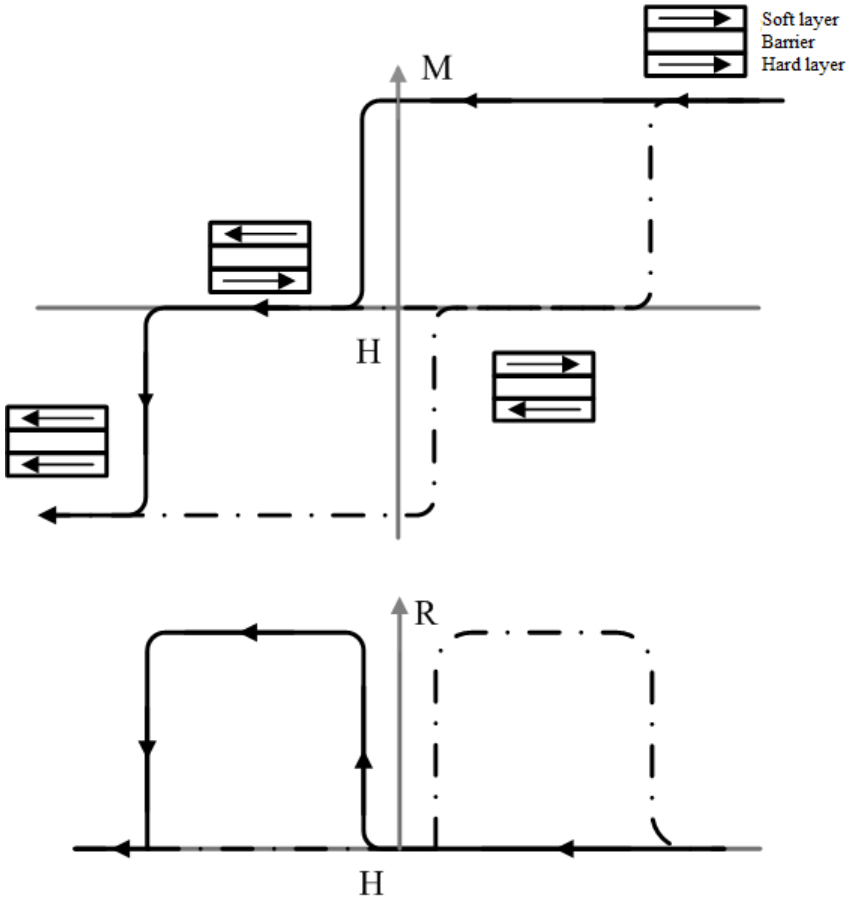

Fig. 2.3: Hysteresis loop (top) and corresponding magnetoresistance loop (bottom) of an MTJ with so called "hard-soft architecture".

origin of the TMR effect lies in the spin-dependent tunneling probability of electrons from one magnetic electrode to the other across an insulating barrier. It can be explained by using Julliere's model, according to which the spin of the electron is conserved during the tunneling process and the conductance for a particular spin orientation is proportional to the product of the densities of states of the two ferromagnetic layers. This means that the tunneling of the spin up and spin down electrons are two independent processes. Therefore, the transport occurs in two independent spin channels.

When the magnetization of the two ferromagnetic layers M_1 and M_2 are parallel, the spin up electrons (from M_1) can easily tunnel through the barrier because many unoccupied spin up states are available in the second ferromagnetic layer (M_2). Therefore, the junction

offers minimum resistance and maximum current flows through it. When the magnetization of the two ferromagnetic layers M_1 and M_2 are antiparallel, usually, fewer spin up states are available in the second ferromagnetic layer (M_2) which suppresses the tunneling. In this case the junction offers maximum resistance and minimum current flows through it.

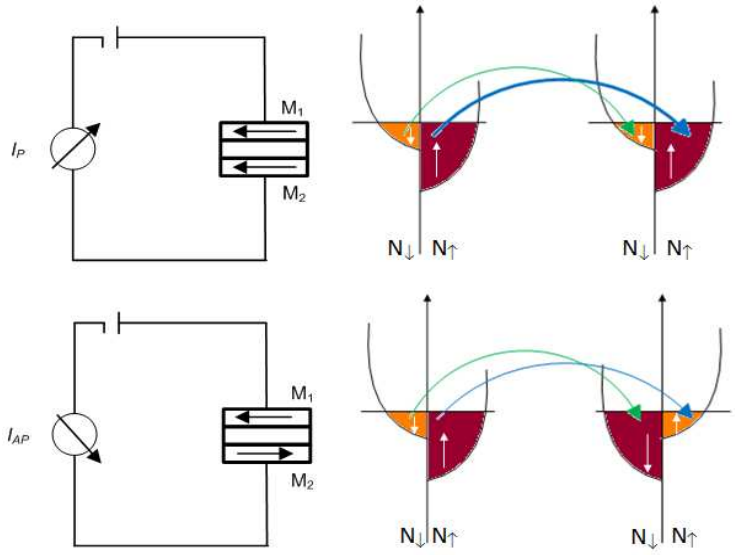

Fig. 2.4: Schematic representation of tunneling of electrons between the two ferromagnetic electrodes (M_1 and M_2) for paralle (above) and anti paralle (below) magnetization orientation. The arrows (left) show spin conserving tunneling of spin up and spin down electrons in spin resolved densities of states of ferromagnetic metals.

2.5 Spin Dependent Transport in Disordered Heterogeneous Systems

The magnetoresistance is not only observed in ordered systems, but also in disordered heterogeneous system. A granular system is an example of a disordered hetrogeneous system in which electrons can tunnel from one magnetic cluster to another through a material of the insulating matrix.

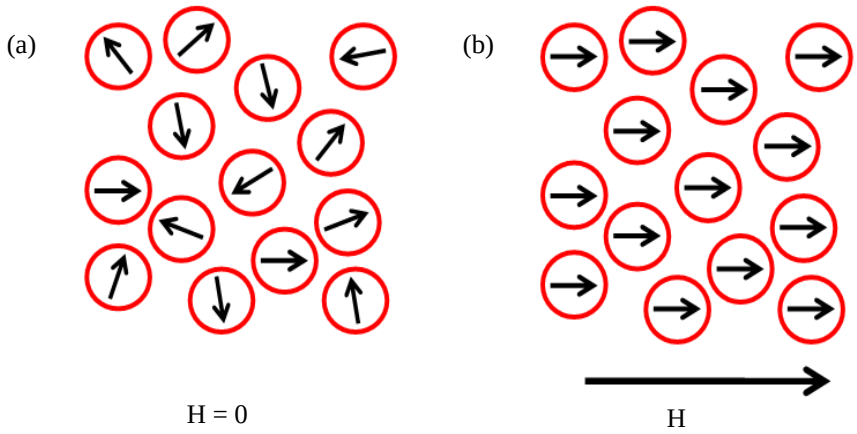

Fig. 2.5: The schematic representation of magnetic granules embedded in an insulating matrix at zero field (a) and at saturation field (b).

Generally, a granular system consists of magnetic particles embedded in immiscible metallic or non-metallic (insulator) matrix with a size distribution of the granules of a few nanometers to hundreds of nanometers. The material of the matrix separates magnetic granules from each other; this avoids the metallic percolation and protects them from environmental degradation (e.g. oxidation) [44]. A schematic representation of a granular system in zero field and saturation field is shown in Fig. 2.5. The granules magnetization are randomly distributed in zero field and they are aligned in the direction of field when a field is applied.

The magnetoresistance in ferromagnetic-insulator granular system is due to the tunneling of spin polarized electrons between the grains through the insulating materix. At zero field, the moments of the magnetic grains are randomly oriented while they become more aligned by the application of external field. This alignment increases the probability of electron tunneling through the barrier material and a decrease in the resistance is observed. The complete phenomenon is explained in the following Fig. 2.6. The g-TMR is given by:

$$g - TMR(\%) = \frac{\rho_o - \rho_H}{\rho_H}.100 \tag{2.5.1}$$

Where ρ_0 is the resistivity at zero field and ρ_H is the resistivity at maximum applied external field.

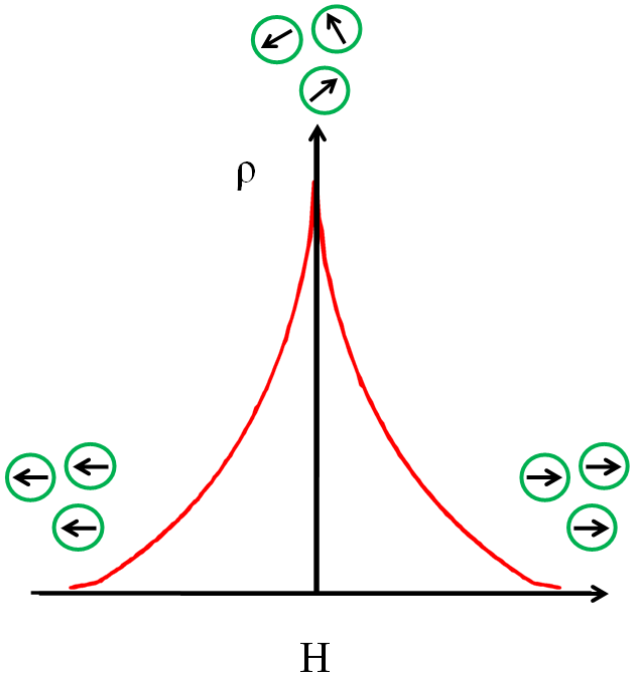

Fig. 2.6: The resistivity versus field in a magnetic/insulator granular system is shown. The resistivity is maximum in the zero field and it decreases with the field.

2.6 Role of the Barrier in Spin Dependent Tunneling

Magnetic tunnel junctions with amorphous Al-O barrier have been extensively studied since the discovery of the room temperature TMR effect. The biggest breakthrough during the last five years was the discovery that the spin polarization of the tunnel current was not only influenced by the electronic properties of the magnetic electrodes, but also by the barrier material [19, 20]. By changing the barrier material from a thin amorphous layer of aluminum oxide (Al_2O_3) to a crystalline layer of magnesium oxide (MgO), the degree of spin polarization increases from 50% to 90% for same magnetic electrode material (CoFe). As a result, the TMR ratio has increased from 70% to 500% at room temperature [1, 21]. The major reason of this large increase is the coherent spin dependent tunneling in epitaxial MTJ with crystalline MgO tunnel barriers.

In Al_2O_3 based MTJs, no crystallographic symmetry exists in the barrier because of its amorphous nature. Furthermore, ferromagnetic electrodes have various Bloch electronic

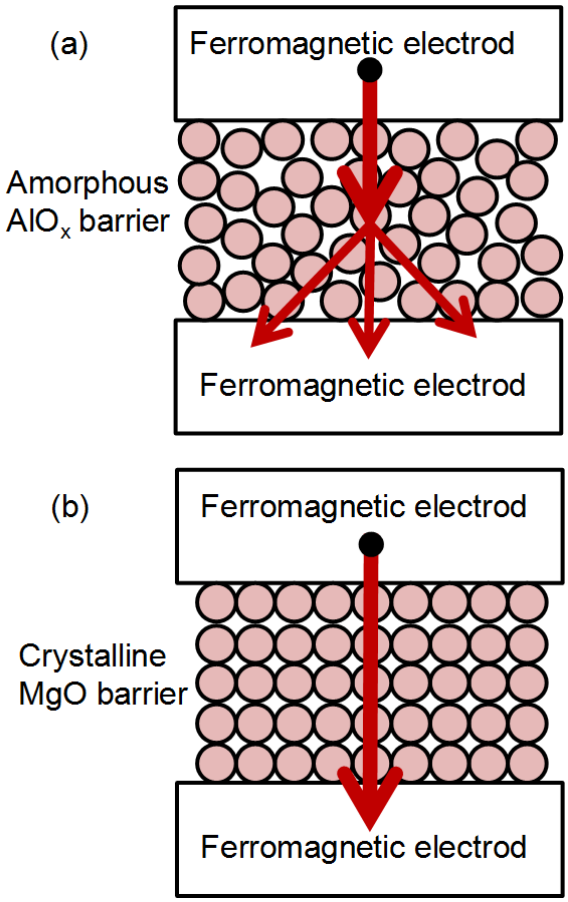

Fig. 2.7: Schematic representation of electron tunneling through an amorphous (a) Al-O barrier (electrons are scattered due to disorder atomic arrangement and (b) crystalline MgO (001) barrier (electrons move straight without any scattering). [20]

states with different symmetries of the wave functions. These Bloch states have finite tunneling probabilities through the barrier. This tunneling process is referred to as incoherent tunneling [45].

In 3d-ferromagnetic metals and alloys, Bloch states with Δ_1 symmetry have positive spin polarization at the Fermi energy, whereas, Bloch states with Δ_2 symmetry have negative spin polarization. It was assumed in Julliere's model that the tunneling probability is independent of the symmetry of the Bloch states. In light of this assumption, the momentum and coherency of Bloch states should not be conserved which gives rise to a complete incoherent

tunneling. However, this assumption is not valid in experimental MTJs, where the tunneling probability depends on the symmetry of the Bloch states. The Bloch states with large spin polarization (i.e.,Δ_1 states) have higher tunneling probability than the other states if the barrier acts as a symmetry filter [20]. This results in a positive net spin polarization of the ferromagnetic electrodes. The other Bloch states (i.e.,Δ_2 with P < 0) are also contributing to the tunneling current and therefore the spin polarization of the electrode is reduced to below 0.6. It should be noted that the actual tunneling through amorphous Al_2O_3 barriers is considered to be an intermediate process between the completely incoherent tunneling represented by Julliere's model and the coherent tunneling shown by the Fig. 2.7b.

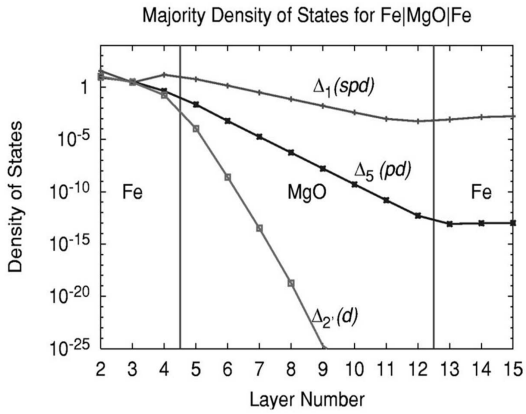

Fig. 2.8: Tunneling DOS (TDOS) for Fe (001)/MgO_{8ML}/Fe (001) for $k_{||}$= 0 of majority spin states with parallel alignment of the moments of two states. The MgO barrier has eight monolayers. The TDOS curves are labeled by the symmetry of the incident Bloch states in the left electrode [46].

In case of an ideal coherent tunneling, $Fe-\Delta_1$ states are theoretically expected to tunnel dominantly through the MgO (001) barrier by following mechanism [45]; for $k_{||}$ = 0, the tunneling probability is the highest and, three kinds of evanescent states, Δ_1, Δ_5 and Δ_2 exist in the band gap of MgO (001). When the symmetries of the tunneling wave functions are conserved, $Fe-\Delta_1$ Bloch states couple with $MgO-\Delta_1$ evanescent states, $Fe-\Delta_5$ Bloch states couple with $MgO-\Delta_5$ evanescent states and $Fe-\Delta_2$ Bloch states couple with $MgO-\Delta_2$' evanescent states. Butler et. al.[46], showed by the first principle calculations

that among these states, the Δ_1 evanescent states have the longest decay length in partial DOS in MgO barrier as shown in Fig. 2.8. Therefore, the $Fe - \Delta_1 \leftrightarrow MgO - \Delta_1 \leftrightarrow Fe - \Delta_1$ channel is the dominant tunneling channel in the parallel magnetic states.

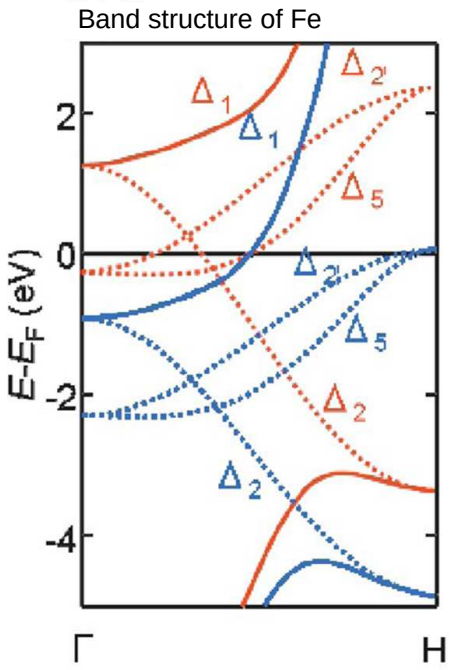

Fig. 2.9: Band structure of Fe calculated by layer-KKR method. Red lines show bands of minority spin and blue lines show majority spin. The majority spin has Δ_1 band at the Fermi level [47].

The band dispersion of bcc Fe in [001] ($k_{||}$= 0) direction is shown in Fig. 2.9. The net polarization of Fe is small because both majority-spin and minority-spin bands have many states at Fermi energy. However, $Fe - \Delta_1$ states are fully spin polarized at E_F (P = 1) and, therefore, a very large TMR effect in the epitaxial Fe/MgO/Fe is expected.

It should also be noted that even for antiparallel magnetic states, a finite tunneling current flows, which is called hotspots tunneling. The origin of this hotspot tunneling is the resonant tunneling between the interface resonant states. Although a finite tunneling current flows in AP states, the tunneling conductance in P states is much larger than that in AP states, therefore, a very high TMR is observed.

2.7 Granular Conductivity

In granular films, which consist of fine metallic grains (ferromagnetic) in any insulating matrix, the transport process is supposed to be controlled by the charging energy of the grains and the spin dependent tunneling of electrons between the grains. The electrical resistivity is thus a function of temperature and magnetic field [48]. According to P. Sheng et al the metallic grains are interconnected by their resistivity of the form

$$\rho \propto exp\left(2\kappa s + \frac{E_c}{2k_BT}\right) \tag{2.7.1}$$

where *s* is the thickness of the insulating layer between the grains, E_c is the charging energy $\kappa = (\frac{2m^*\varphi}{\hbar})$, m^* is the effective mass of electron, φ is the barrier height, $\hbar$ is the Plank's constant,k_B is Boltzman constant and T is the absolute temperature [49]. E_c is the amount of energy required to generate a pair of positively and negatively charged grains. It is assumed that electrons tunnel between the grains of the same sizes, i.e., cannot tunnel either to a smaller particle since the charging energy is larger or to a larger particle which further away since the tunnel resistance is larger. The tunneling of electrons at high temperature is mainly between the nearest neighbors. Sometimes it is also termed as nearest neighbor hopping. The condition necessary for the nearest neighbor hopping is the existence of large number of pairs of close neighbors in which one of them has empty sites. As the temperature decreases below a certain limit the number of empty sites among the nearest neighbors becomes small and hopping to the nearest site freezes out. Therefore, it is more favorable for electrons to hop beyond the region of nearest sites to find optimal energy sites [50]. This is called Mott Hopping (MH). The well known Mott's Law for hopping in three dimensional disordered systems is given by the equation

$$\rho = \rho_o exp\left(\frac{T_{oM}}{T}\right)^{1/4} \tag{2.7.2}$$

with

$$R_M \approx \frac{1}{\alpha}\left(\frac{T_{oM}}{T}\right)^{1/4} \tag{2.7.3}$$

and

$$T_{oM} \approx \frac{\alpha^3}{k_B n_(o)} \tag{2.7.4}$$

Where T_{oM} is a constant proportional to charging energy, ρ_{oM} is a pre-exponential factor, α is the inverse localization length R_{oM} is the hopping distance and $n_{(0)}$ is the density of state near the Fermi level. While deriving the equation of resistivity by Mott the effect of Coulomb interaction between the electrons was neglected. In this case the density of state (DOS) around the Fermi level is nearly constant. Efros and Shklovskii discussed the significance of the coulomb interaction and its influence on the DOS [51]. They proposed that if long range coulomb interactions between the localized states are taken into account then the DOS is reduced near the Fermi level or completely suppressed at the Fermi Level. The Efros Shklovskii Law at low temperature is then

$$\rho = \rho_{oA} exp \left(\frac{T_{oA}}{T}^{1/2} \right) \tag{2.7.5}$$

with

$$R_{ES} \approx \frac{1}{\alpha} \left(\frac{T_{ES}}{T} \right)^{1/2} \tag{2.7.6}$$

and

$$T_{ES} \approx \frac{\alpha e^3}{k_B \epsilon} \tag{2.7.7}$$

Where T_{ES} is a constant proportional to charging energy, ρ_{oM} is a pre-exponential factor, α is the inverse localization length, R_{ES} is the hopping distance and ϵ is the dielectric constant of the insulating material.

2.8 Experimental Investigations

In this work the structure and quality of MgO tunnel barrier in ordered system (MTJs) are investigated at the first stage and the role of MgO barriers in disordered systems (granular systems) is discussed in the second stage. Different bottom electrodes i.e., Ru and CoFeB, are used to analyze the MgO barrier in ordered system. The defect density in the barriers and resistance are analyzed with the help of Conducting Atomic Force Microscopy (CAFM). Different thicknesses of MgO are deposited on a Ru under layer and analyzed to optimize the CAFM setup. For the characterization of the MgO in MTJ's, half finished magnetic tunnel junctions (HFMTJ) are prepared. HFMTJs are the junctions in which a normal layer stack

of MTJ is used but the deposition is stopped after the barrier layer. The results are compared with complete MTJs.

In the second stage of this work the spin dependent transport in disordered system (granular system) of CoFeB/MgO is investigated. The transport properties of the system are studied by changing the thickness of individual MgO and CoFeB layers. The role of MgO barriers in disordered systems is studied and the results of disordered system are compared with their structures. Effects of annealing on the microstructures and the electrical and magnetoresistance properties are discussed at room temperature. The temperature dependent measurements down to to 1.25 K provide a deep insight into the transport mechanisms in this system. A short comparison of CoFeB/MgO with other disordered systems highlights the importance of this disordered system.

Chapter 3

Experimental Techniques

This chapter includes the experimental techniques for the fabrication of multilayers and granular systems. Different methods used for the characterization and analysis of these samples are also mentioned in this chapter. Only a brief explanation has been provided in most cases. The readers who are interested to learn more about these are recommended to refer the citations.

Two kinds of multilayer systems, ordered multilayer and disordered multilayer systems, have been investigated in this thesis. Disordered multilayer system has been deposited at room temperature by DC and RF magnetron sputtering on thermally oxidized Si wafers. Discontinuous layers are formed at the early stage of the film growth. Initially, the film grows in the form of clusters and the size of these clusters grows by the deposition of the film. These clusters then join up to form a complete layer. An ordered multilayer system is formed by the deposition of complete layers. All samples investigated in this thesis have been fabricated by a Leybold Dresden *CLAB600* sputtering system.

3.1 Magnetron Sputtering

The basic principle of sputtering is to bombard the target material with high energy plasma ions (Ar ions), accelerated due to the high potential of the target (e.g. 100V to 1000V) and to deposit the atoms which have been knocked out of the target on the substrate placed above the target. This is schematically represented in Fig. 3.1. *CLAB600* has six magnetron sources

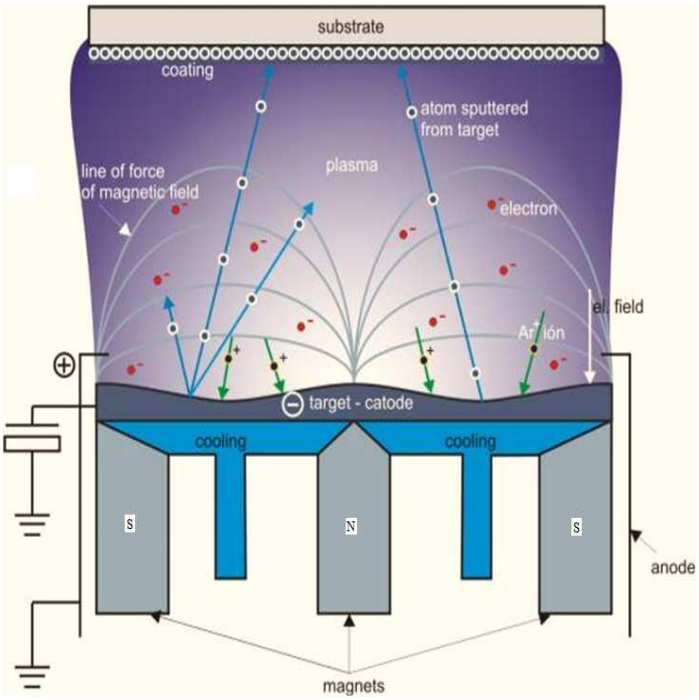

Fig. 3.1: Schematic representation of a sputter sourace [55].

of 4 inch diameter. Two of them are capable of sputtering magnetic materials. One source is operated in RF mode for sputtering insulating materials and the other three sources are used for sputtering non-insulating and non-magnetic materials. The distance between target and substrate is kept at 11.5 $\pm$ 0.3 mm, depending on the target thickness. The thickness of the deposited material is controlled by the power applied to the source and the deposition rate. The deposition rate of each material is calculated by the X-Ray reflectometery measurements of extra deposited samples of the corresponding material. Detail of the deposition process can be found in Ref. [52, 53, 54].

The samples for CAFM studies were prepared on the Si wafers without mask. The samples of disordered multilayer system of CoFeB/MgO were sputtered through masks in the form of of rectangular bars of dimension 2 mm $\times$ 15 mm for the electrical measurements. However, they were also sputtered in the form of sheets for XRR and magnetic measurements.

3.2 Annealing

The sputtered deposited films are generally not in saturated equilibrium and under residual stress. This is removed by moderate annealing. The samples are annealed in a computer programmable vacuum furnace. The base pressure of the furnace is 2 $\times 10^{-8}$ m bar. with the maximum attainable temperature of 550^{o} C. For annealing, samples are moderately pressed on 2 inch$\times$ 4 inch copper plate which is connected to the heating filament; pipes are used for cooling down with compressed air. The annealing is always started at 1×10^{-7}m bar.

3.3 DC Resistivity and Magnetoresistance Measurements

For electrical and electromagnetic characterization of the granular samples, the resistivity and g-TMR measurements are done at room temperature and temperatures down to 1.25 K. For room temperature measurements a measuring device optimized for magnetic tunnel junctions is used. It is possible to apply a maximum voltage of $\pm$ 2 V by this device. The current is measured by an electrometer with 6 amplification ranges (10 mA, 1 mA, 100 μA, 10 μA, 1 μA and 100 nA). The magnetic field is applied by using two coils energized by two BOS/S-36V-12A power supplies with an error of $\pm$ 1 Oe. The maximum magnetic field produced by this equipment is $\pm$ 3500 Oe. For the more details of setup see Ref. [56]. The DC resistivity and the g-TMR are measured by using conventional 4-contact technique. The contact to the granular layers under a top MgO capping layer is obtained by pressing a sharp end gold needle on the sample surface.

The temperature dependent resistivity and g-TMR measurements are carried out in an Oxford Instruments closed cycle *He* cryostat, which provides a temperature down to 13 K. The current-voltage setup is the same as above but the maximum magnetic field of this setup is $\pm$ 1770 Oe. For more details of the experimental setup see Ref. [57]. For low temperature measurements, four Au electrodes in rectangular shape are sputtered on the sample surface. The dimension of these electrodes is 100 $\mu m \times$ 1.5 mm and they are 100 μm separated from each other. These electrodes are contacted by Au-wire bonding.

For measurement of the Coulomb gap energy, a ^{4}He cryostat constructed by O. Schebaum

during his Diploma thesis is used [58]. It consists of two Dewar vessels containing liquid *N* in the outer vessel and liquid *He* in the inner vessel. Both Dewar vessels, made of glass, are silvered inside to protect against the external radiation heating. The sample is introduced in the liquid *He* with the help of a Dip -Stick. At normal atmospheric pressure the boiling point of He is 4.21 K and Nitrogen is 77 K. By pumping out the *He* gas atoms having largest Kinetic Energy (K.E.), the average K.E. of the *He* is reduced. Therefore, the pressure and as a consequence the temperature of the *He* bath is reduced. The temperature of the *He* bath can be reduced to 1.2 K.

3.4 Scanning Electron Microscope (SEM)

For surface studies of the samples and to take the images of the conducting tips a LEO 1530 Scanning Electron Microscope (SEM) is used. The SEM allows investigation of samples over a wide range of magnifications down to a resolution of a few nanometers. The basic principle of a scanning electron microscope is to focus a fine electron beam on a sample and scan over the area of interest. To obtain an image, the backscattered electrons as well as secondary electrons resulting from inelastic scattering from the electron beam in the sample can be detected.

3.5 Alternating Gradient Magnetometer (AGM)

The magnetization of the granular samples is measured by an Alternating Gradient Magnetometer (AGM) MICROMAG 2900 from the PRINCETON MEASUREMENT CORPORATION. The maximum magnetic field, generated by an electromagnet, is 14 kOe at an air gap of 12 mm. The sensitivity goes down to 10 pAm^2 with an accuracy of 2%. The sample is mounted at the end of vertical quartz rod, the other end of which is attached to the bottom of a piezoelectric sensor Fig. [59]. A large electromagnet is used to produce an external magnetic field up to 14 kOe. Two small electromagnets produce an alternating magnetic field gradient across a region in which the sample is placed. The alternating field gradient exerts an oscillatory force on the sample. This force induces a mechanical deflection in the

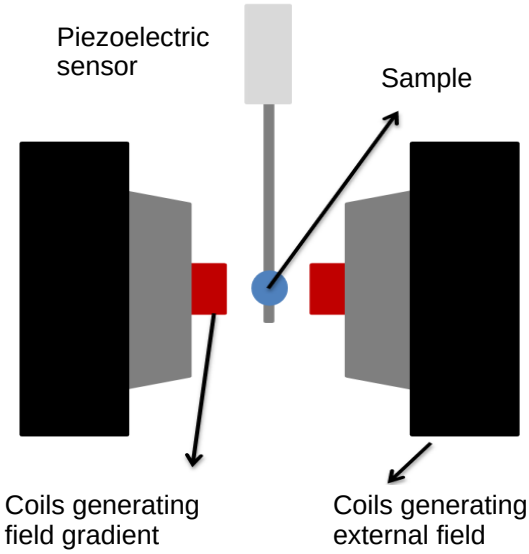

Fig. 3.2: Schematic representation of alternating gradient magnetometer (AGM).

quartz rod, which is transmitted to the piezoelectric sensor. The bending of the piezoelectric sensor then produces a voltage signal proportional to the amplitude of the oscillation. From this signal the magnetic moment of the sample is determined because the oscillatory force is proportional to the product of the magnetic moment times the field gradient. To calculate the magnetization of the sample one needs to know the volume of the magnetic layers in the sample. More details of AGM are available in Ref. [60]

3.6 High Resolution Transmission Electron Microscopy

High resolution transmission electron microscopy (HRTEM) is a suitable tool for the study of nanoparticles and nanostructures in bulk materials. It is used for direct measurement of three dimensional images, crystal structures and elemental composition. Usual diffraction techniques, X-Ray Diffraction and Neutron Diffraction collect structural information from a large number of unit cells (typically 10^{15}) so they give an average structure. On the other hand, HRTEM directly measures microstructures in solids on the nanometer scale. Therefore, many local structures on this scale can be observed by HRTEM. The HRTEM operates on the same working principle as that of a light microscope. However, the high resolution

is obtained by using electrons instead of photons. As we know that the resolution is proportional to the wavelength of the particles used and the wavelength associated with the electron is thousand times smaller than that of usual light. Therefore, the resolution of a HRTEM is thousand times better than that of the light microscope. An electron source at the top of the HRTEM emits electrons that travel through vacuum in the column of the HRTEM. Electromagnetic lenses are used to focus the electrons into a very fine beam. The focused electron beam transmits through the specimen and interacts with the material of the specimen. Depending on the density of the material, a fraction of electrons is transmitted through the specimen. An image is formed by the transmitted electrons. This image is magnified and focused onto an imaging device, such as a fluorescent screen, on a layer of photographic film, or to be detected by a sensor such as a CCD camera. The working of a TEM is shown in the Fig. 3.3. For more details of HRTEM the references can be consulted [61, 62, 63].

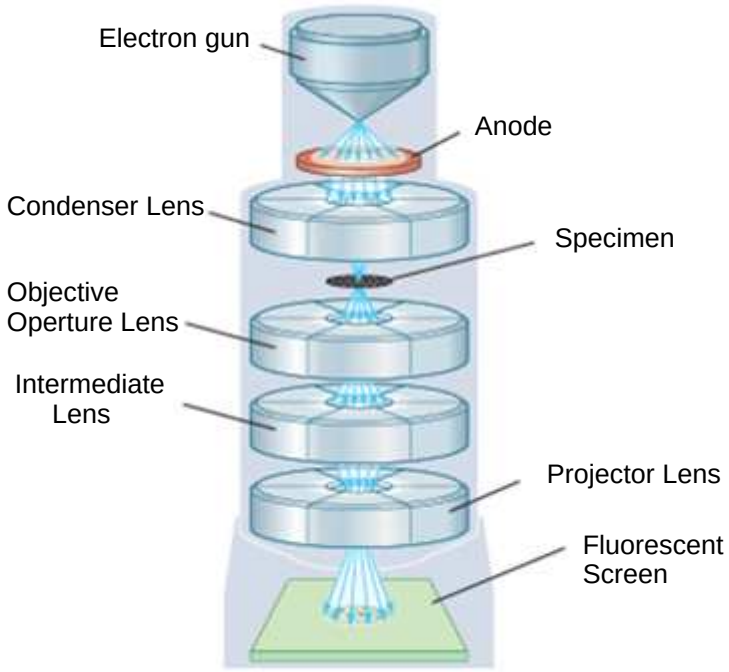

Fig. 3.3: Schematic view of Transmission Electron Microscope [55].

3.7 Atomic Force Microscopy

Atomic force microscopy is a powerful tool for analyzing the surface of a sample. It is used here to probe the surface of multilayers accurately and deduce the valuable information from its topography. AFM operates by scanning a very sharp and tiny tip attached at the end of a cantilever across the sample surface. The tip approaches the surface of the sample and interacts with it via van der Waals forces in case of large distances . For small distances, repulsive Pauli-Forces occur. The interaction translates in a cantilever deflection or a change in the cantilever oscillating frequency, depending on the operational mode of the AFM. Changes on the deflection or the frequency of the cantilever are detected by an optical system consisting of a laser beam which is reflected on the cantilever and arrives to a four quadrant photodiode detector which measures the vertical as well as the horizontal deflection. The displacement of the cantilever in three dimensions is done by means of a piezoelectric scanner, combining independently operated piezo electrodes for X, Y and Z direction into a single tube. The AFM used in our experiments is an "Explorer" made by Topometrix. It operates in two modes.

1) Contact mode

2) Non-Contact mode

3.7.1 Contact Mode

In this mode the tip is brought into direct physical contact with the sample surface (i.e., in the range of repulsive forces). The tip applies a force on the sample surface and this force is controlled by the feedback loop. During the measurements this feedback loop keeps the force constant. As the probe scans, varying topographic features of the sample surface cause deflections of the tip. A light beam from a small laser bounced off the cantilever is reflected on to the four sections photo detector. The amount of deflection of the cantilever can then be calculated from the difference in light intensity on the sectors of photodiode and fed back into the feedback loop which maintains constant deflection. The Contact AFM is the simplest AFM method, involving least instrument variables for gathering topographic information.

3.7.2 Non-Contact Mode

As the tip moves across the sample surface, it may cause damage to soft or fragile samples such as biological specimens or polymers. To avoid this sometimes non-contact scanning is preferable. In non-contact mode, the cantilever is oscillated above the sample at its resonance frequency. As the tip get closer to the sample surface, the attractive force between the tip and the sample will change the oscillation amplitude and phase of the vibrating cantilever. Either the changes in amplitude or the changes in phase can be detected and used by the feedback loop to produce topographic data. A detailed information about the operation of the AFM can be found in the literature [64].

3.8 Conducting Atomic Force Microscope

Conducting Atomic-Force Microscopy (C-AFM) is an advantageous method for a local electrical characterization of e.g., barrier materials at the nanometer scale. In this technique, a conductive tip is used to scan the sample surface in contact mode. An additional electronics is used to provide a bias voltage between sample surface and tip and the resulting current tunneling between the thin barrier and the AFM tip is recorded. Therefore, topographic and current measurements can be recorded simultaneously. The details of electronics are given below:

3.8.1 Power Supply

A DC bias voltage is applied between the tip and the sample by a homemade power supply which can apply a minimum voltage of 5 mV $\pm$ 1 mV and a maximum of 5 V.

3.8.2 I/V Convertor

The flowing current is amplified by using a current amplifier LCA-1K-5G made by Femto. This current amplifier is a low noise (3fA$/Hz^{1/2}$), high gain (5 $\times 10^9$) and fast response (400 μs rise/fall time) device with a minimum detectable current of 1 pA and saturation current of

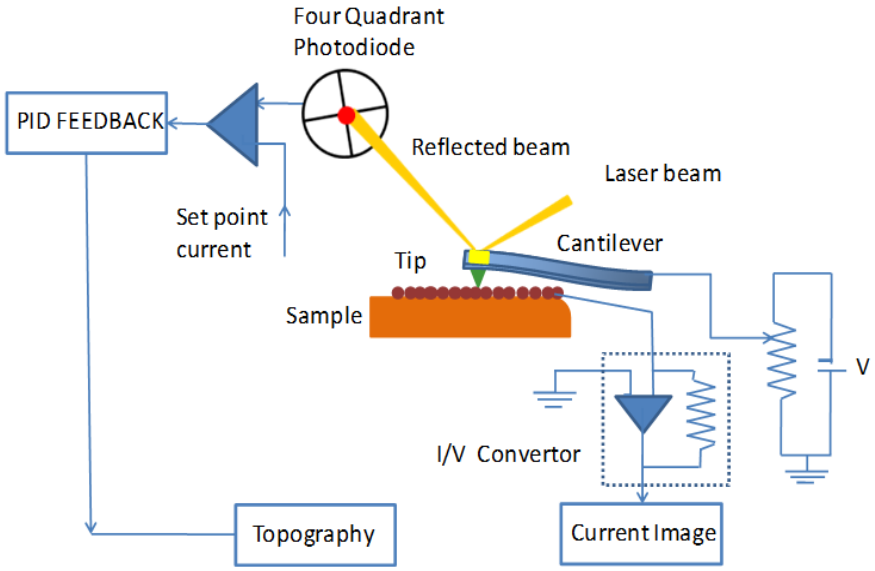

Fig. 3.4: Schematic representation conducting atomic force microscope

$\pm$ 2 nA. When connected to the AFM, the noise of the current measuring assembly increases. Therefore the minimum detectable current increases to around 10 pA.

3.8.3 Conducting Tips

Besides the performance of the acquisition setup the nature and properties of tip probes are very important for the quality of the results. The tip should have low resistance to provide a good electrical contact and it should be sharp enough to produce good quality topographic features. A variety of conducting tips were used to measure the local electrical properties of MgO surface including diamond coated tips, Au coated and Pt/Ir coated tips. Pt/Ir coated tip worked well for the MgO surface. It is an antimony doped Si tip with front side and back side coating with 20 nm Pt/Ir. The front side Pt/Ir coating provides an electrical path from the cantilever to the apex of the tip, while the backside coating serves as a reflective coating and also compensates the stress created by the front side Pt/Ir coating. The apex radius of the tip is in the range of 60 to 140 nm with a spring constant of 2.8 N/m.

3.8.4 Contact Force

Information about contact force is very important for reliable current maps in the CAFM technique. In Topometrix AFM the sensor current along with a feedback circuit keep the contact force constant. When tip moves in feedback, the sensor response curve gives information about the force conversion factor (nN/nA), cantilever deflection (nA) versus piezo displacement (nm) curve and sensor response (nA/nm). By using the force conversion factor and sensor current the exact value of the contact force can be calculated.

3.9 Aspects of CAFM

The aspects of CAFM which are most attractive for nano scale electrical transport measurements are

1) The ability to image samples with high resolution before, during and after the measurements.

2) The ability to record I-V relationships on samples that are highly resistive or surrounded by insulating regions

3) Straightforeword interpretation of the tip position relative to sample (a measured repulsive force indicates intimate tip sample contact)

This makes CAFM ideal for studying electrical transport in micro-fabricated semiconductor devices, nanoparticle assemblies and individual molecules [65].

Chapter 4

Characterization of MgO Tunnel Barriers

This chapter discusses the characterization of MgO barriers in ordered multilayerd structures. The quality of the ultra thin MgO films for the tunnel barrier in the MTJ devices is investigated by employing a modified conducting atomic force microscope. This is a direct technique for studying the conductance locally by making conductance and topographic maps of MgO films simultaneously. The MgO films are investigated by using Ru as bottom electrode and half finished magnetic tunnel junction. Different imaging parameters of the tip-sample contact like contact resistance, radius of contact spot and imaging force were optimized by scanning MgO with Ru bottom electrode. These optimized imaging parameters are used to study the electrical properties of MgO tunnel barriers in MTJ's. A statistical model to study the fluctuations in tunneling transmission through thin insulating barrier proposed by F. Bardou is used to quantify the quality of MgO barrier. The major part of this chapter has been published in the reference [66].

4.1 Introduction

Magnetic tunnel junctions (MTJs) are extensively used as memory cells and read head sensors in hard disk technology. However, these devices must be improved to meet the future requirements of ever increasing data storage capacity of hard disks. It requires MTJs having

maximum signal to noise ratio (SNR) and increase in reading data rate. Submicron MTJs with low resistance and high TMR ratio can fulfill these requirements [67, 68]. The signal is given by $\eta \times i_B \times \Delta$R and noise is determined by the resistance R of the device [69]. Here η is the head efficiency, i_B is the bias current and ΔR is the change in resistance of the device induced by the magnetic field. High data storage capacity requires a small data track width on the disk which decreases the efficiency of the sensor. Furthermore, the decrease in the size of memory cells requires a small bias current i_B so that the rise of temperature can be avoided. Therefore, the decrease in signal due to η and i_B can be compensated by increasing ΔR. Furthermore, the noise is reduced by decreasing the resistance of the device. Hence, the device resistance R should be small enough and the change in resistance (ΔR) should be large enough to obtain a maximum SNR. In conclusion, a low resistance MTJ with ultrahigh TMR ratio is a suitable device for future hard disk technology. This is only possible for an MTJ when it has a thinnest possible closed barrier layer.

4.2 Characterization of Barrier

Magnesium oxide (MgO) is, at the moment, the best candidate for the barrier material in magnetic tunnel junctions, because of its superior tunneling magnetoresistance (TMR) value compared to AlO_x, the possible low Resistanec$\times$ Area (RA) product and high thermal stability [19, 20]. A theoretically predicted TMR value of 6000% has been reported for MTJs with MgO barriers, while the highest experimentally achieved TMR values are up to 500% at room temperature [46, 70, 71, 72, 73, 21]. Imperfections in the MgO barrier induced, e.g., during the deposition of MTJs are potential obstacles to further increase the TMR ratio and to implement extremely low resistive MTJs in read head sensors. A better understanding of these imperfections in ultra thin barriers is of vital significance for controlling the uniformity and other quality parameters and to make them suitable for industrial applications. X-ray photoemission spectroscopy, secondary ion mass spectroscopy and decoration of pinholes by electrodeposition of copper on the insulating barriers are among various techniques that have been developed to study imperfection in insulating barriers [74]. These techniques and their limitations will be briefly discussed in the following paragraphs.

4.2.1 X-ray Photoemission Spectroscopy and Secondary Ion Mass Spectroscopy

X-ray photoemission spectroscopy is a method of measuring the kinetic energy distribution of photoelectrons emitted from the specimen material excited by monochromatic light. It gives complete information about bound electron states in the material; therefore, it is used to study both electronic structure and chemical bonding [75]. This technique is extensively used for the investigation of nano layers and their buried interfaces.

Secondary ion mass spectroscopy is the most sensitive technique to analyze the elemental composition of a surface or thin film. In this technique the surface of a specimen is sputtered by a focused primary ion beam and the ejected secondary ions are collected and analyzed by a spectrometer. It helps to analyze the elemental, isotopic and/or molecular composition of the surface. Both of these techniques provide global information on the chemical composition, surface interface structure and thickness of barrier material. They are, however, unable to determine the quality of the barrier material locally at the nanometer scale.

4.2.2 Decoration of Pinholes by Electrodeposition of Copper

The decoration technique is an important tool to map submicron pinholes in an insulating barrier. It is a classical technique to see the structures which are not accessible by direct imaging. This is done by the galvanic growth of appropriate material at the structure to be detected. Pinholes which are formed in an insulating layer on top of a metal film have an intrinsic large conductivity. By using this property a preferred growth of copper by electrodeposition on the pinholes can be achieved. The growth structures can be imaged by scanning electron microscopy.

The pinhole decoration by electroplating of copper leads to growth of cauliflower-like copper particles of various sizes. Initialization of the growth process requires a short pulse of increased voltage. This causes nucleation of small structures with typical diameter less than 200 nm. Continuation of the growth leads to an increase in the size of these structures. R. Schad et.al. studied the fluctuation in Al_2O_3 barrier thickness by using this technique [76]. The Fig. 4.1 shows the SEM image of their typical sample consisting of bottom

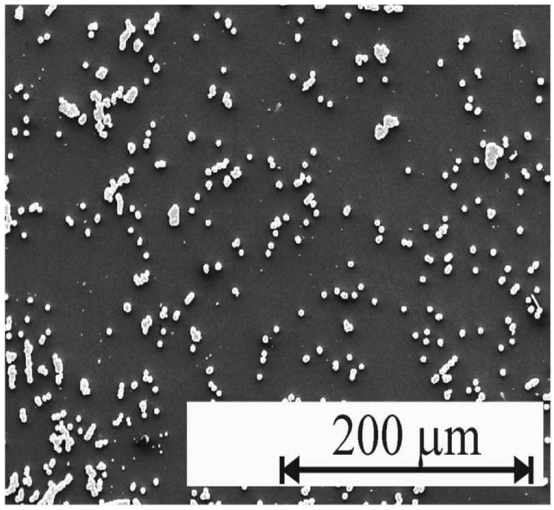

Fig. 4.1: An SEM image of a sample having a bottom ferromagnetic electrode and a 1.8 nm thick insulating layer of Al_2O_3 after nucleation of Cu island on pinholes [76].

ferromagnetic electrode and an insulating layer of 1.8 nm thick Al_2O_3. The image has been taken after applying a short pulse of 0.5 V for 10 seconds followed by the electrodeposition of Cu. The initial voltage pulse leads to the breakdown of all weak links with local insulator thickness of less than 5 $\circ A$. Without the initial voltage pulse copper growth is not observed which indicates that the sample did not have intrinsic pinholes.

4.2.3 Rowell's Criteria

In the 1960s and 1970s, a set of criteria (so-called Rowell criteria) was formulated to identify single-step elastic electron tunneling in superconductor-insulator-superconductor (S-I-S) structures. Only three of those criteria can be applied to identify the tunneling of electron when neither of the electrodes is a superconductor. These are

1) An exponential thickness dependence of the conductance (or resistance),

$$R_{(t_{barrier})} = exp\left(\frac{t_{barrier}}{t_o}\right) \tag{4.2.1}$$

Where t_o is the Wentzel - Kramer - Brillouin (WKB) decay length.

2) The conduction should show a parabolic voltage dependence which should be well fitted to theoretical models of Brinkman - Dynes - Rowell (BDR) or Simmons.

3) The conduction should have an insulating-like temperature dependence i.e., the resistance should decrease with temperature.

In the MTJ literature, the second criterion is most commonly used. Akerman et.al. intentionally created shorts in the ultrathin aluminum oxide barriers and showed that the first two criteria - thickness dependence and the voltage dependence of the conductance - are necessary but not sufficient or reliable in ruling out the presence of pinholes and to identify the quality of the barrier [77, 78]. Bryan Oliver et.al. found tunneling like $R(T)$ dependence in intentionally shorted devices and Venture et.al. observed a mixed $R(T)$ behavior in devices with thin insulating barrier [79, 80]. Therefore to identify the quality of ultrathin barrier some additional tests are needed.

4.3 Conducting Atomic Force Microscopy

Conducting atomic force microscopy (CAFM) is a powerful technique for the simultaneous measurement of conductivity and topography at nanometer scale [81]. It is used to evaluate and rank the merits of new materials and fabrication methods, without producing and testing the final device [82]. This technique has been extensively used for investigating the conductance distribution on metal surfaces, insulator-conductor hetero-structures and granular metal-insulator nano-composites [83, 84]. At low bias voltage, CAFM can resolve the spatial fluctuations of the local current through the barrier and thus reveal defective sites or imperfections. The nature of the tip-sample contact plays an important role for the characterization of a barrier in the CAFM geometry. Any change in shape of the tip leads to a severe change in the image and the results on electrical properties of the sample. Evaluating the contact resistance between tip and sample and the radius of the contact spots will help to understand the transport processes in the CAFM. In the following paragraphs contact resistance and radius of contact spots will be discussed for our CAFM setup.

4.3.1 Measurement of the Contact Resistance

In order to calculate the contact resistance, a test sample with special structures of conducting triangles and squares on a Ru surface were prepared by coating e-beam resist on it. The

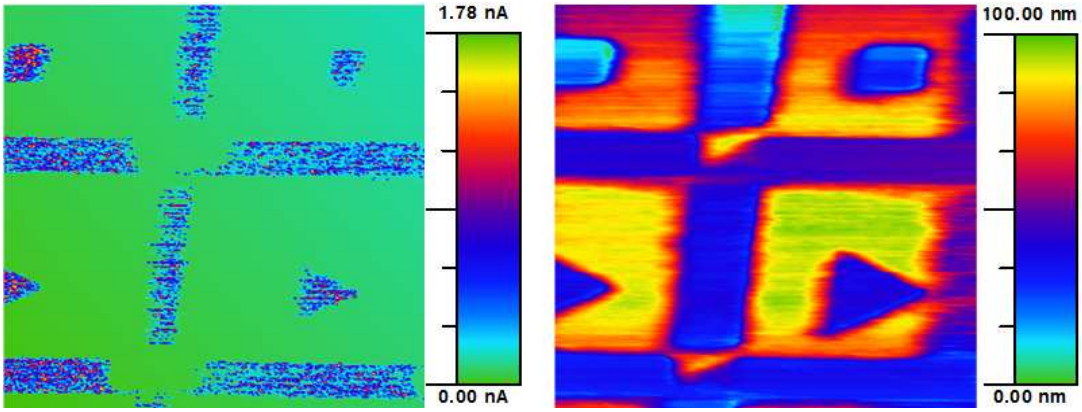

Fig. 4.2: Simultaneously scanned conductance (left) and topography (right) maps of a test sample having conducting triangles and squares made by putting e-beam resist on a Ru surface

sample was scanned with the CAFM setup discussed in section 3.8. An additional resistance of 10 MΩ was introduced to limit the current between tip and sample. The sample was scanned by applying different bias voltages, where the current must be in the range of I/V convertor. At a voltage of 20 mV a maximum current of 1.78 nA was obtained. The contact resistance was then calculated by the circuit equation

$$R_c = \frac{V_b}{I} - R \tag{4.3.1}$$

where R_c is the contact resistance, V_b is the bias voltage and R is the additional resistance. By using the above mentioned values, R_c resulted in 1.23 MΩ.

4.3.2 Area of the Contact Spot

The radius "a" of the mechanical contact spot of the sample and the tip can be calculated by using Hertz' Law [85]

$$a^3 = \frac{3R_tF}{4E^*} \tag{4.3.2}$$

Here R_t is the radius of the tip and F is the force exerted on the sample. This force can be obtained from the deflection of cantilever. E^* is a constant given by

$$E^* = \left[\frac{1-\mu_t^2}{E_t} - \frac{1-\mu_s^2}{E_s}\right]^{-1} \tag{4.3.3}$$

Where;

E_s = Young Modulus of MgO = 248.17 GPa [86]

E_t = Young Modulus of tip (Pt/Ir) = 100 GPa [87]

μ_s = Poisson ratio of MgO = 0.18

μ_t = Poisson ratio of the tip (Pt/Ir) = 0 <μ_t < 0.5 [87]

F = 3.60x10^{-7} N

R_t = 60 nm - 140 nm

Using Eq. 4.3.2, Eq. 4.3.3 and the values of the parameters for the materials used, the radius of the contact spot is evaluated between 6 nm and 8 nm leading to a contact area in the range of $10^{-4}\mu m^2$.

4.3.3 Hotspots

The hotspot density and the resistance of hotspots are considered as parameters to characterize the MgO tunnel barriers. "Hotspots" are defined as areas of the barrier, which show a prominent current signal in the current maps due to defective sites in the barrier. These hotspots can alter the TMR value and degrade the device performance. The current I_{HS} measured by our setup is given by the following equation

$$I_{HS} = I_o + I_{hs} \tag{4.3.4}$$

Where I_o is the typical current or background current at the bias voltage of V_0 from the major parts of the oxide surface and I_{hs} is the current originating from the hotspots additionally to I_o. Only those peaks will be considered as hotspots for which $I_{hs} = 3 \times i_n$ (three times the peak to peak value of noise current). I_{HS} is the hotspot current which can vary between $I_o + 3 \times i_n$ and 2 nA (the maximum limit of our current measuring assembly).

4.4 Characterization of an MgO Tunnel Barrier on Ru Bottom Electrode

CAFM has not been extensively used because of the difficulties in achieving reproducible measurements. The tip sample contact, ambient environment, imaging force and appropriate

interpretation of the results limit a wide range of application of this technique. In this work the imaging conditions of CAFM for characterization of MgO barrier are optimized. This is done by scanning different thicknesses of the MgO barrier using Ru as bottom electrode at different imaging forces and bias voltages.

4.4.1 Sample Preparation

In order to fabricate the samples for this study, multi-layers were deposited at room temperature by DC and RF magnetron sputtering on thermally oxidized Si wafers. This deposition was carried out by using Ru as bottom electrode with sequence SiO_2 (50) / Ta (5) /Ru (20) / MgO (t_B) (all numbers in parentheses are in nm and t_B represents the thickness of the MgO). The samples of this series (Ru_series) are labeled as Ru_0.5, Ru_0.8 and Ru_1.0 corresponding to the bottom electrode Ru and MgO thickness of 0.5, 0.8 and 1.0 nm, respectively.

4.4.2 Results and Discussion

Optimization of Imaging Force

The force between tip and sample surface during imaging plays an important role for studying the imperfections, like "hotspots" in the MgO barriers. To find the optimum imaging force, the sample Ru_0.5 was scanned with different imaging forces at a bias voltage of 10 mV. A force less than 2.0×10^{-7} N was not enough to penetrate the insulating layer of water between the tip and the sample and it was not possible to get a good electrical contact between them [88]. However, by increasing the imaging force from 3.5 $\times 10^{-7}$N to 6.5 $\times 10^{-7}$ N the background current increases from 0.52 nA to 0.56 nA, accordingly a decrease in resistance was observed. The number of hotspots was also increased due to the increased imaging force that might create some additional pinholes in the barrier e.g., a large green area at the bottom of the Fig. 4.4(c) and 4.4(e) appeared due to the damaging of insulating layer of MgO by increased force of the tip. The increased force also damages the conducting layer of the tip which was observed by taking the SEM images of the tip before and after applying a force of 6.5$\times 10^{-7}$N. The SEM images of the tip are shown in Fig. 4.3. In addition, multiple scans of the same area showed nearly same results at 3.5 $\times 10^{-7}$ N as shown

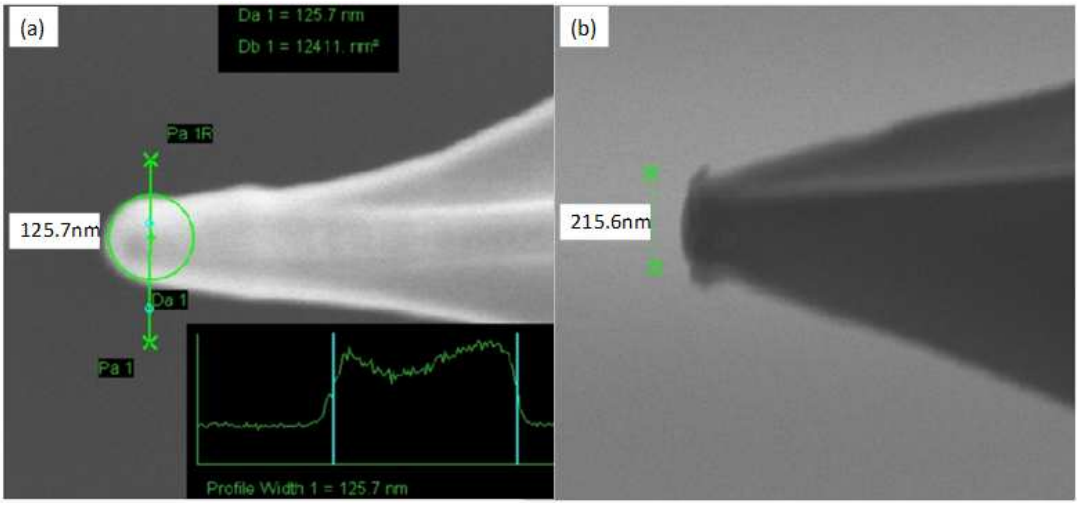

Fig. 4.3: SEM images of the same tip before (a) and after (b) applying a force of 6.5 $\times 10^{-7}$ N

in Fig. 4.5. Therefore, to study the intrinsic hotspots, an imaging force of 3.5 $\times 10^{-7}$ N was considered as safe and used throughout the study. At this contact force, a current of around 1 nA is found at the best conducting regions of the sample at 10 mV. This implies that a contact resistance of 10 MΩ or less is present between the tip and the sample surface.

Hotspot Analysis

The current maps of Ru_series are shown in Fig. 4.6. When the sample Ru_0.5 was scanned at 10 mV, most of the scanned area showed a background current of 0.52 nA with $i_n = 20$ pA. This is considered as typical current for 0.5 nm of MgO with a corresponding resistance of 20 MΩ. However, a large number of current spikes with a current more than 0.58 nA (0.52 + 0.06nA) at the local minima of the topographic profile have been observed, which are called "hotspots" in this thesis (sometimes also termed as pinholes). The resistance of these hotspots lies in the range of 17 MΩ to 5 MΩ and the density of these hotspots at 10 mV is 80 $\pm 5/\mu m^2$, which is high enough to shorten the 0.5 nm thick barrier of Ru_0.5.

Samples Ru_0.8 and Ru_1.0 were scanned for different bias voltages and almost no hotspots were found at the bias voltage of 10 mV (not shown). The first current signals for Ru_0.8 and Ru_1.0 occurred at 20 mV and 300 mV, respectively. By increasing the MgO thickness from 0.5 nm to 0.8 nm the background current decreases from 0.52 nA to 0.17 nA

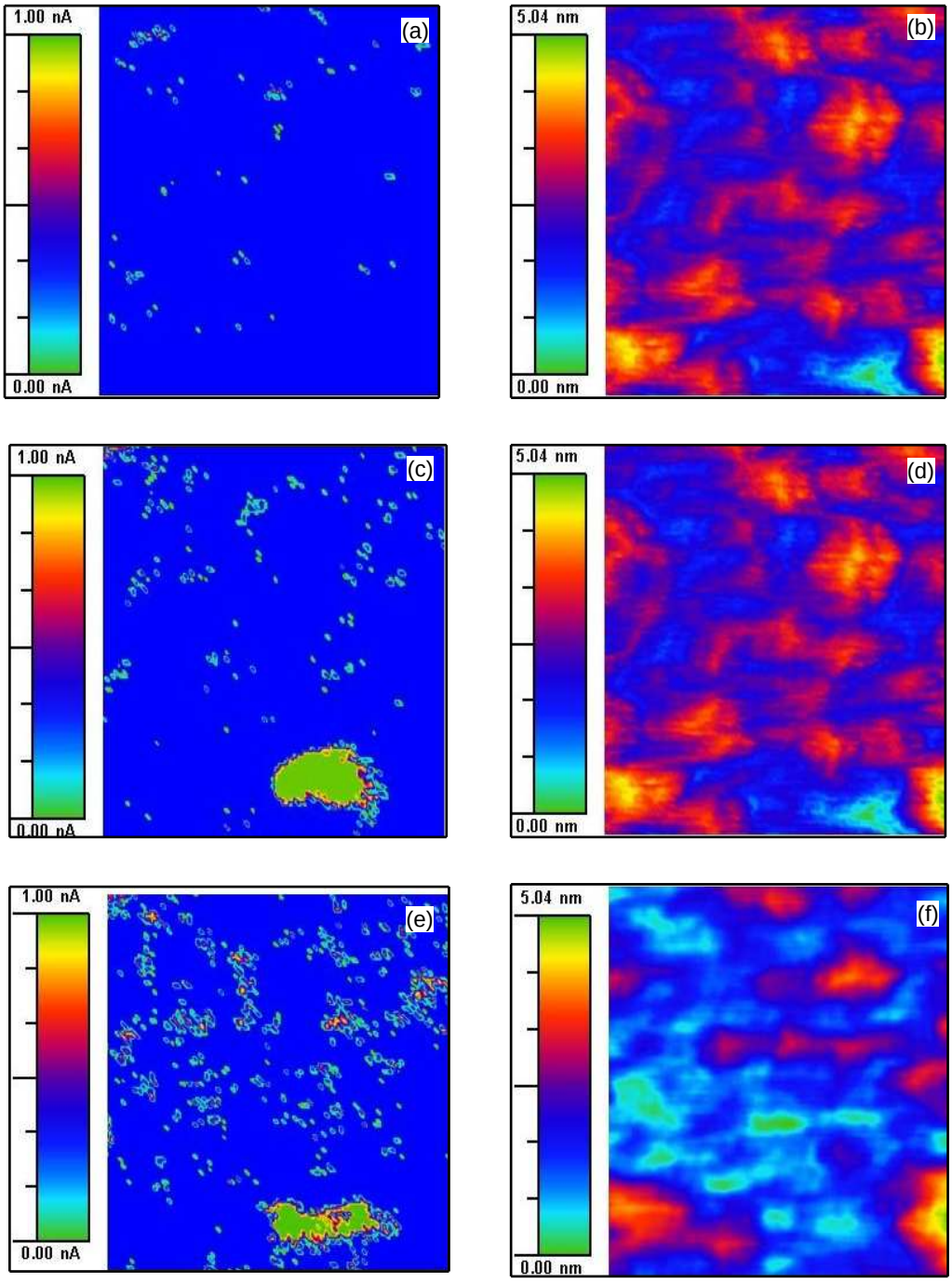

Fig. 4.4: Simultaneous current maps of (left panel) and topography maps (right panel) of Ru_0.5 scanned at bias voltage of 10mV and force of 3.5×10^{-7} N, 5.0×10^{-7}N and 6.5×10^{-7} N are represented in Fig. (a) and (b), in Fig. (c) and (d) and in Fig. (e) and (f) respectively. The green areas in the current maps show current more than 1 nA

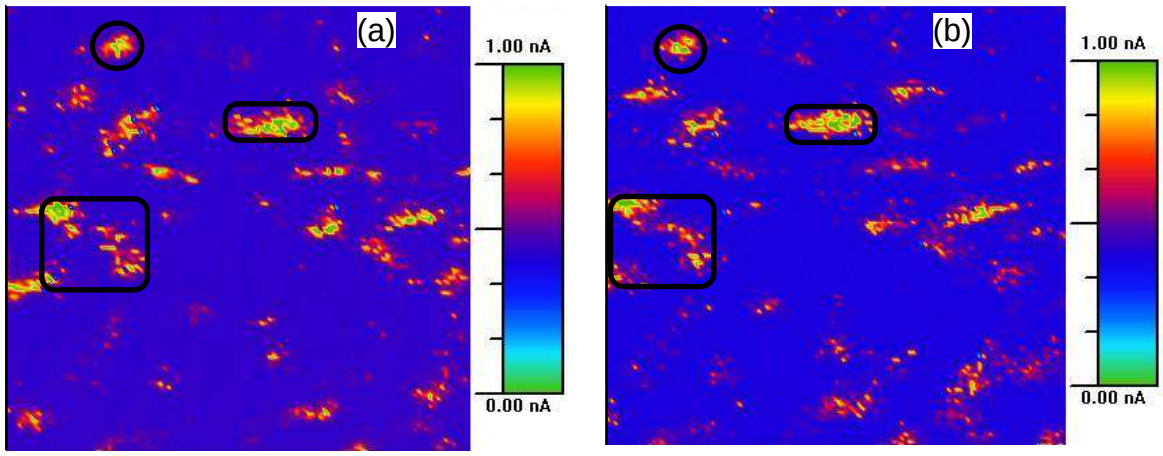

Fig. 4.5: Current maps of the same area scanned at the force of 3.5×10^{-7} N. The marked area in the first scan (a) and in the second scan (b) are identical.

with $i_n = 16$ pA. The density of hotspots decreases from $80 \pm 5/\mu m^2$ at 10 mV (d_{MgO} = 0.5 nm) to $30 \pm 2/\mu m^2$ at 20 mV (d_{MgO} = 0.5 nm). The resistances of these hotspots lie between 100 MΩ to 20 MΩ. Although the resistance of these hotspots is two to ten times more than 10 MΩ but their density is too high to make this junction perfect.

There exists an insulating barrier all over the surface of 1.0 nm thick MgO film because of infrequent hotspots ($5 \pm 1\ /\mu m^2$). The background current and noise current mixes here at 5 pA so the peaks with 15 pA current are considered as hotspots and the resistance of these hotspots is in the range of $10^{10}\Omega$.

Bias Voltage Dependence

The same sample was scanned at different bias voltages and the result is shown in Fig. 4.7. A nonlinear increase in the hotspot density has been observed. To findout whether the defects observed by applying a high voltage were permanent or not, the sample Ru_1.0 was scanned first at a high voltage. The subsequent scans of the same area with lower voltage gave correspondingly reduced density of hotspots. This indicates that the defects seen at higher voltage were not induced by the tip and/or the voltage.

The other important information achieved by scanning of Ru_1.0 at different bias volt-

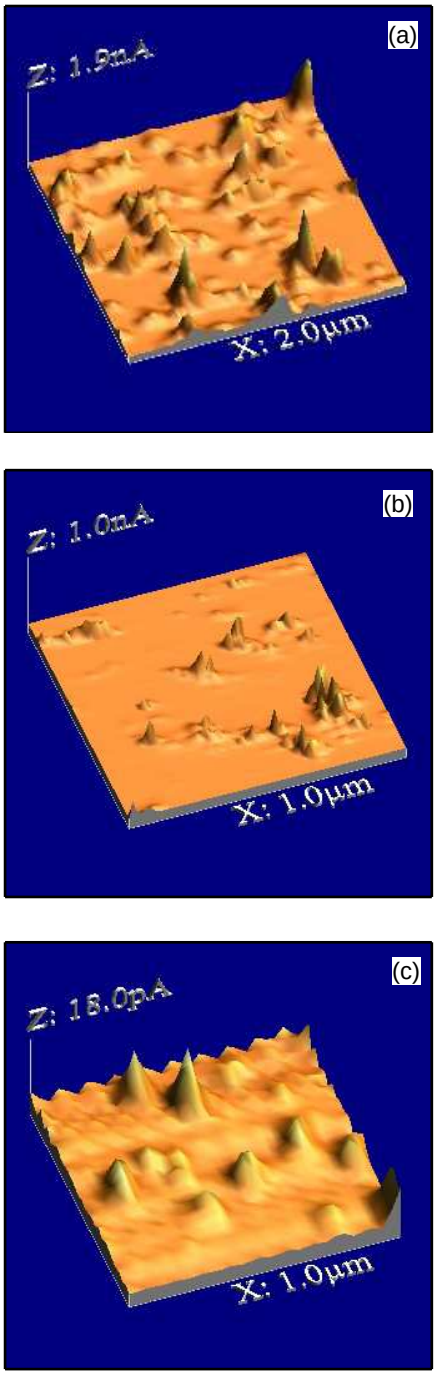

Fig. 4.6: Three dimenssional current maps of Ru_0.5, Ru_0.8 and Ru_1.0 scanned at a bias voltage of 10, 20 and 300 mV depicted in (a), (b) and (c) respectively

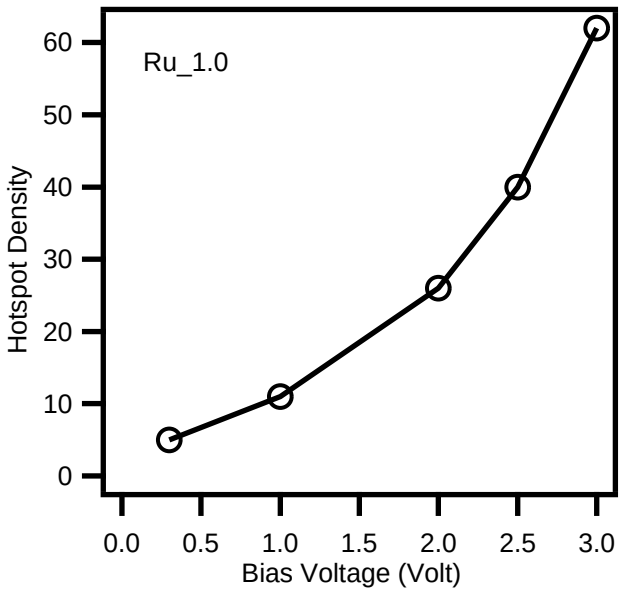

Fig. 4.7: Hotspot density as a function of bias voltage for a 1 nm thick MgO Ru bottom electrode.

ages is the maximum current (I_{max}) as a function of the bias voltage (V_b). Fig. 4.8 shows a graph of I_{max} vs V_b. This graph also shows a nonlinear increase of I_{max} with V_b which indicates that the current at an MgO thickness of 1.0 nm is obtained by tunneling through the 1 nm thick MgO barrier.

Statistical Analysis

F. Bardou presented a statistical model which treated the variation in tunneling transmission due to the fluctuations of the barrier parameters [89]. He predicted that a small fluctuation in the barrier parameters leads to a very large variation in the tunneling current. The total tunneling current is dominated by a small amount of highly conducting sites (hotspots) which are related to the existence of disorder in the barrier. A broad distribution of current with a long tail characterizes a significant spatial variation of the barrier properties. On the other hand, a narrow current distribution indicates a small spatial variation of the tunnel barrier and is a signature of very high quality barrier. We have used his model to quantify the quality of our tunnel barriers.

The probability for a particle of mass M and kinetic energy E to tunnel through a rectan-

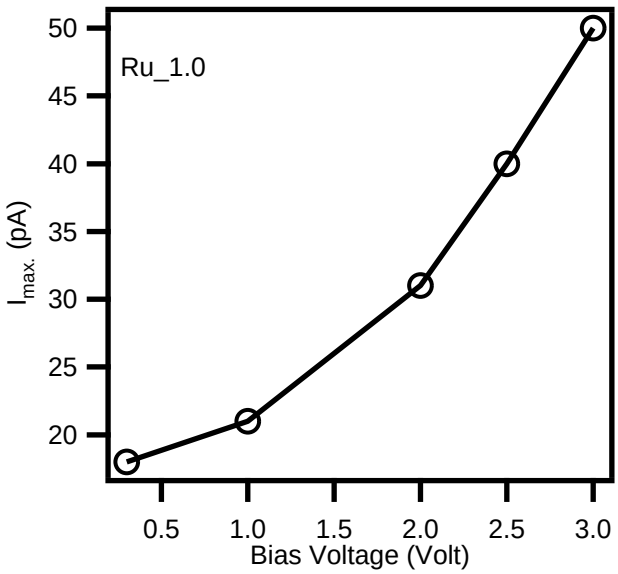

Fig. 4.8: Maximum current as a function of bias voltage for a 1 nm thick MgO layer on a Ru bottom electrode.

gular barrier of height V_o and thickness *l*, where *l* » λ, is given by

$$t = 4Aexp\left(\frac{-l}{\lambda}\right) \tag{4.4.1}$$

Where $\lambda = \frac{\hbar}{2\sqrt{2M(V_o-E)}}$ is the attenuation length in the barrier and *A* = $\frac{4E(V_o-E)}{V_o^2}$. This leads to a log normal probability distribution $P_t(t)$ of the transmission *t*

$$P_t(t) = \frac{1}{\beta\sqrt{2\pi}}\frac{1}{t}exp\left[-\frac{1}{2\beta^2}(ln(t)-\alpha)^2\right] \tag{4.4.2}$$

Here $\alpha = ln(4A) - \frac{\langle l\rangle}{\lambda}$ is a scale parameter, $\beta = \sigma_l/\lambda$ is a fluctuation parameter and σ_l is the standard deviation of the barrier thickness *l*. Since we measure a local current *i* and not local transmission *t*, a proportionality factor η such that *t* = ηi is introduced. This linear transformation leads to a current distribution

$$P_i(i) = \eta P_t(\eta i) \tag{4.4.3}$$

with a new scale parameter

$$\acute{\alpha} = \alpha - ln(\eta) \tag{4.4.4}$$

but the same fluctuation parameter β related to the barrier fluctuations. Then $\acute{\alpha}$ and β can be calculated from the current images as follow

$$\acute{\alpha} - \beta^2 = ln(i_{typ}) \tag{4.4.5}$$

and

$$2\acute{\alpha} + \beta^2 = 2ln(\langle i \rangle) \tag{4.4.6}$$

Where i_{typ} is the most probable local current also called typical current and $\langle i \rangle$is the average local current.

The values of bias voltage, typical current, average current scale parameter $\acute{\alpha}$ and fluctuation parameter β for samples Ru_0.5, Ru_0.8 and Ru_1.0 are given below

Sample	V_b (mV)	i_{typ}(nA)	$\langle i \rangle$(nA)	$\acute{\alpha}$	β
Ru_0.5	10	0.54	0.99	-0.2121	0.63568
Ru_0.8	20	0.17	0.4949	-1.05959	0.844021
Ru_1.0	300	0.005	0.02394	-4.25424	1.021799

Fig. 4.9a shows the normalized probability density distribution and normalized distribution of experimental data for sample Ru_0.5. A broad distribution of local current with a long tail is prominent for 0.5 nm thick barrier. The current extends from the typical value of 0.54 nA to maximum value of I/V convertor 2.0 nA. The current decreases slowly from 0.54 nA to 2.0 nA which indicates the large variation in the thickness of the barrier. This means that the probability of large current for a thinner barrier is high which is due to the existence of low resistance hotspots. An increased probability at the tail of the experimental data curve is prominent which also associates the presence of low resistance hotspots (or pinholes) in the barrier. The current through the barrier is dominated by these hotspots. For a barrier of 0.8 nm thick MgO the distribution of local currents becomes narrower than for the 0.5 nm thick MgO barrier. The distribution curve shows a decrease in the local currents from a typical value of 0.17 nA to the maximum value of 1.0 nA. The experimental distribution appeared to incline upwards at the end which is depicted in Fig. 4.9(b). This upward inclination is due to the presence of a small number of highly conducting sites at this thickness.

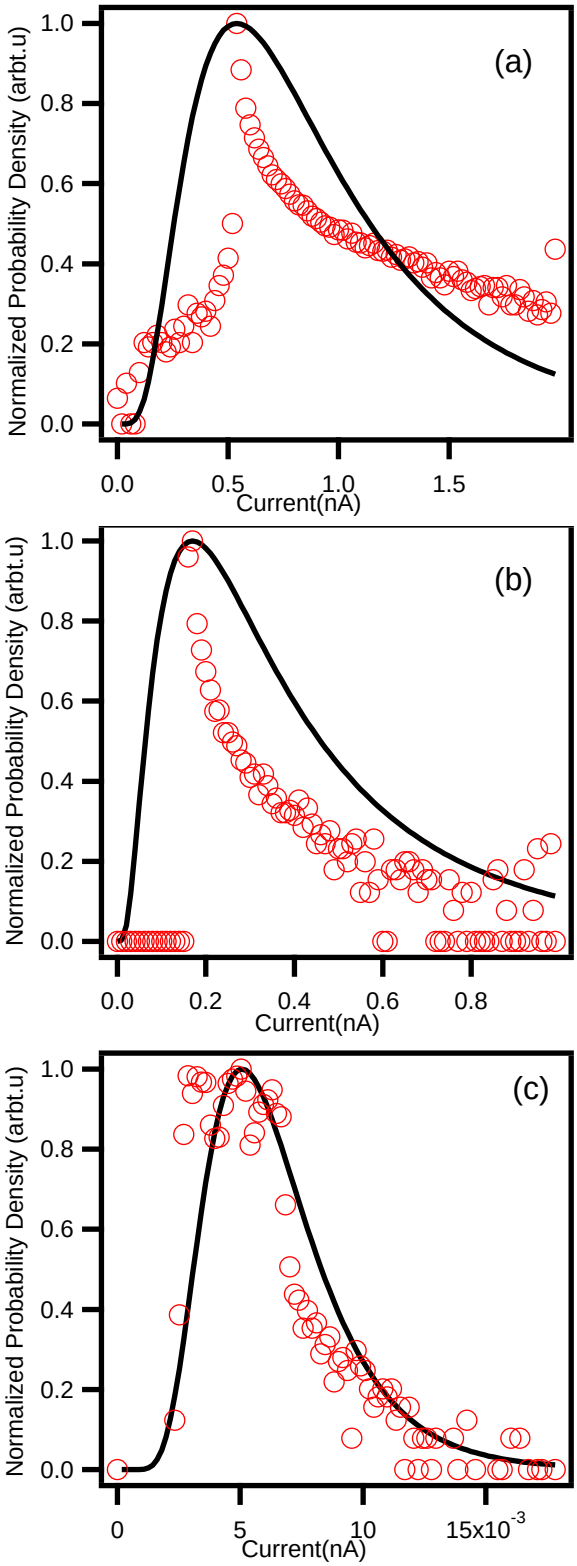

Fig. 4.9: Normalized theoretical current density distribution (-) and normalized experimental distribution (o) of the local currents for samples Ru_0.6 (a) scanned at bias voltage 10 mV, Ru_0.8 (b) scanned at bias voltage 20 mV and Ru_1.0 (c) scanned at bias voltage 300 mV

In Fig. 4.9c (d_{MgO} = 1 nm) the local current distribution decreases quickly from 5 pA to 20 pA and most of the current is distributed in a narrow region around 5 pA. Normalized probability density and normalized distribution of experimental data fit well for 1 nm thickness of MgO. At this thickness the MgO barrier on Ru electrode is complete and approximately free from hotspots.

4.5 Characterization of MgO Tunnel Barrier in Half Finished Magnetic Tunnel Junctions

For industrial application of MTJ as read heads and random access memory in the rapidly developing industry of data storage devices, the resistance of the junctions and the fluctuation in the junction resistance should be as small as possible. This can be achieved by decreasing the thickness of the barrier material and controlling the fabrication conditions. In order to achieve the thinnest possible barrier with small fluctuations in the resistance a local characterization of barrier with the help of CAFM is very helpful.

After optimizing the imaging conditions for the CAFM setup it has been used for the characterization of half finished magnetic tunnel junctions which is the main theme of this thesis. The half magnetic junctions are those junctions (HFMTJ) in which deposition is stopped after the barrier layer. The upper electrodes are not deposited and the tip of the CAFM acts as upper electrode. Such samples are used to study the quality and the local electrical properties of the barrier. In the following paragraph the electrical properties of HFMTJs with various thicknesses of MgO barriers will be studied. In order to get a complete insulating barrier of MgO the images will be analyzed in term of their hotspot density, resistance and resistance area product. Furthermore, the quality of these barriers will be statistically analyzed by the statistical model introduced by F. Badou [89].

4.5.1 Sample Preparation

The samples for this study were prepared by the same procedure as mentioned above. Three samples with varying thickness of MgO were fabricated with sequence SiO_2 (50) / Ta (5) /

Ru (30) / Ta (5) / Ru (5) / MnIr (12) /CoFeB (2.5) /MgO (t_B) (all numbers in parentheses are in nm unit and t_B represents the thickness of MgO). The samples are labeled as CoFeB_0.6, CoFeB_0.8 and CoFeB_1.0 corresponding to the bottom electrode CoFeB and MgO thickness of 0.6, 0.8 and 1.0 nm respectively.

4.5.2 Results and Discussion

The conductance images of the samples CoFeB_0.6, CoFeB_0.8 and CoFeB_1.0 are presented in Fig. 4.10. When the sample CoFeB_0.6 was scanned at a bias voltage of 10 mV, a background current of 0.64 nA with $i_n = 20$ pA was observed. The current map in Fig. 4.10(a) indicates a large number of higher current signals originating from uncovered or very thinly MgO covered CoFeB. The current of these hotspots was ranging from 0.7 nA to 2 nA with corresponding resistance from 14 MΩ to 5 MΩ. These low resistance hotspots can thus easily short a 0.6 nm thick MgO film. As the thickness of the MgO film increases from 0.6 nm to 0.8 nm, the background current and the noise current deceases to 0.32 nA and 16 pA with a decrease of the maximum current to 1.4 nA. There is also a rapid decrease in the density of the hotspots with the corresponding resistance ranging between 26 MΩ and 7 MΩ. The previously occurring conductance from hotspots (i.e. at 0.6 nm) is converted into tunneling conductance but still, there exist some hotspots ($20 \pm 2\ /\mu m^2$) with the resistance in the range of 10 MΩ which can make the working of the junction device unreliable.

Almost no hotspots were found in CoFeB_1.0 (1 nm MgO) at a bias voltage of 10 mV (not shown), the first current signals with a background current 18 pA with $i_n = 6$ pA and a maximum current of 200 pA appeared at a bias voltage of 20 mV. The conductance of this sample at a bias voltage of 20 mV is shown in Fig. 4.10(c). This conductance map reveals only nominal hotspots, which have a resistance in the range between 550 MΩ and 100 MΩ. These hotspots correspond to points of reduced thickness of MgO film rather than contact pinholes as the minimum resistance of these hotspots is ten times larger than contact resistance. Therefore, one can easily say that a complete insulating barrier exists at 1.0 nm of MgO.

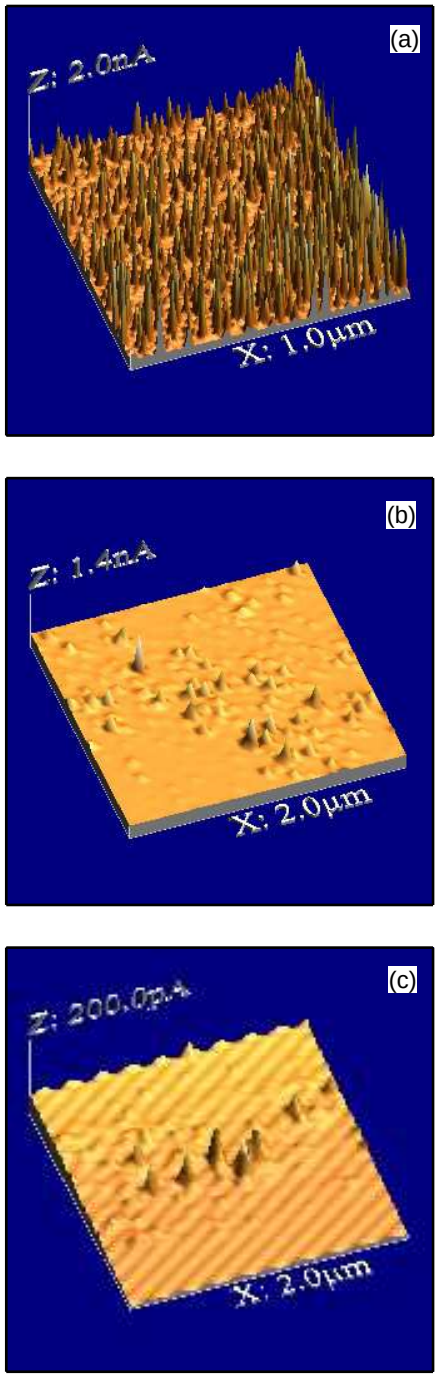

Fig. 4.10: Three dimenssional current maps of CoFeB_0.6, CoFeB_0.8 and CoFeB_1.0 scanned at a bias voltage of 10, 10 and 20 mV depicted in (a), (b) and (c) respectively

4.5.3 Statistical Analysis

From the current maps of HFMTJs, the probability density distribution of the local current has been calculated in the same way as for the Ru bottom electrodes to quantify the quality of the insulating barrier and results are shown in Fig. 4.11. The table below represents the values of parameters $\acute{\alpha}$, β bias voltage V_b and typical current i_{typ} for samples CoFeB_0.6, CoFeB_0.8 and CoFeB_1.0 calculated from the respective current images.

Sample	V_b (mV)	i_{typ}(nA)	$\langle i \rangle$(nA)	$\acute{\alpha}$	β
CoFeB_0.5	10	0.64	0.99	-0.1554	0.5392
CoFeB_0.8	10	0.323	0.667	-0.6466	0.6952
CoFeb_1.0	20	0.018	0.099	-2.8808	1.0660

It has already been explained that a broad distribution of the current with a long tail characterizes a significant spatial variation of the barrier properties [89, 90]. On the other hand, a narrow current distribution indicates a very small spatial variation of the tunnel barrier and is a signature of very high quality tunnel barrier. It is clear from Fig. 4.11 that for sample CoFeB_1.0, the distribution decreases quickly form the typical currents 18 pA to 200 pA and most of the current is distributed in a narrow region around 18 pA. Normalized probability density and normalized experimental distribution fit well for 1 nm thickness of MgO. This indicates a complete insulating barrier approximately free from hotspots. For samples CoFeB_0.8 and CoFeB_0.6 the currents extend from typical value of 0.32 nA to 1.4 nA and 0.64 nA to 2 nA, respectively. The current distribution curves are broad with a relatively slow decrease for larger currents. This means that the probability of the large current for thinner barrier is high which is due to the existence of low resistance hotspots. A peak in the experimental curve at the end is prominent which also shows the existence of low resistance hotspots in this barrier. Normalized probability density show a very poor fit to the experimental distribution for thinner barriers because of the existance of highly conducting hotsopts.

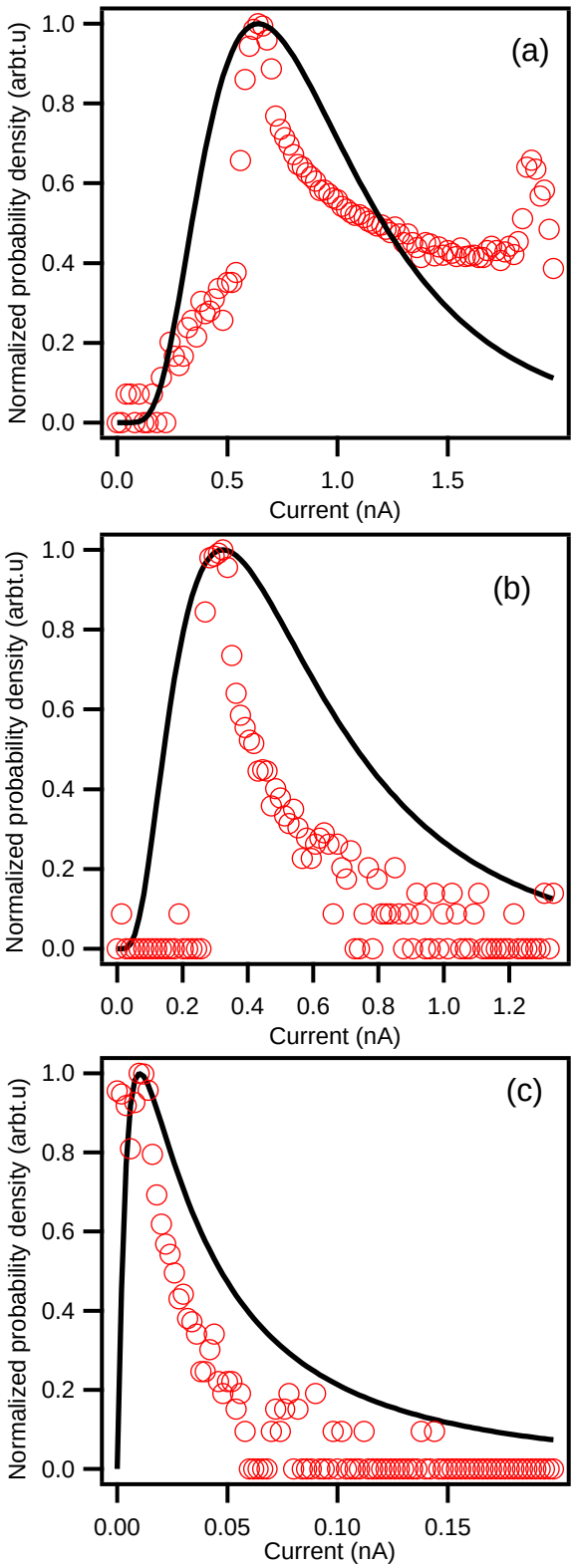

Fig. 4.11: Current versus normalized density distribution (-) and normalized experimental distribution (o) of the local currents for samples CoFeB_0.6 (a) , CoFeB_0.8 (b) scanned at bias voltages of 10 mV and CoFeB_1.0 (c) scanned at bias voltage 20 mV

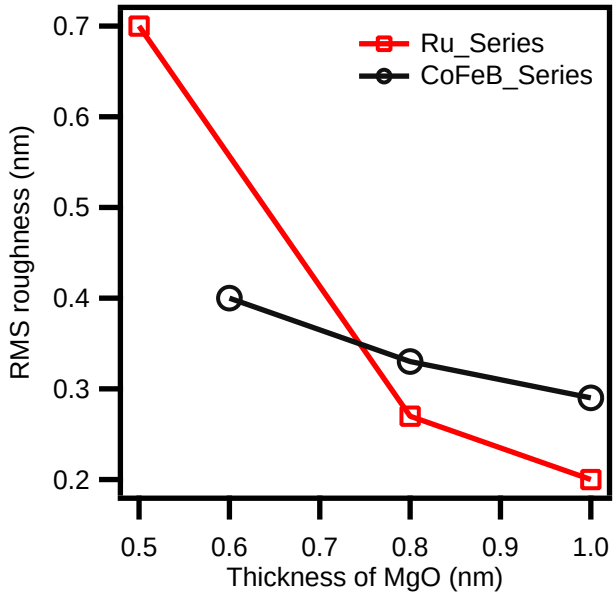

Fig. 4.12: The RMS roughness versus the thickness of MgO on Ru bottom electrode (Ru_Series) and on CoFeB bottom electrode (CoFeB_Series).

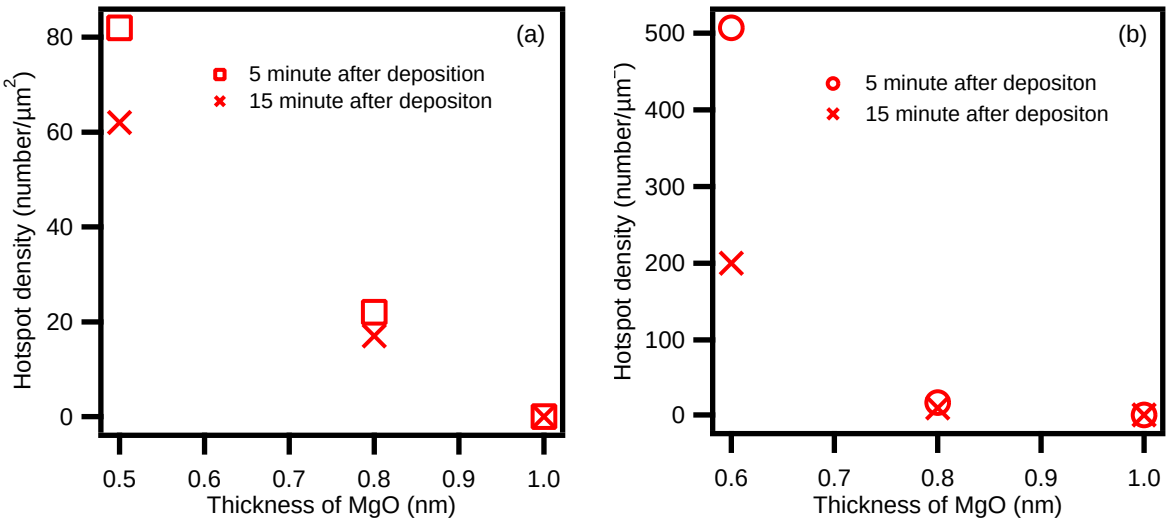

Fig. 4.13: Hotspot density versus thickness of MgO taken after 5 and 15 minutes of deposition for Ru_series (a) and CoFeB_series (b).

4.6 Comparison of Hotspots, Resistance and Resistance Area Product with Complete MTJ's

The resistance area product (RA) can be estimated by using the radius of the contact spot of the tip as calculated in Eq. 4.3.2 and the applied bias voltage divided by the measured current. The expected metal - metal resistance (R) and RA product in this setup lie in the range of $10^6\ \Omega$ and $10^2\ \Omega\mu m^2$ respectively, whereas those of metal - insulator - metal are in the range of $10^9\ \Omega$ and $10^5\ \Omega\mu m^2$ respectively. RA product of 300 $\Omega\ \mu m^2$ has been measured for CoFeB/MgO/CoFeB MTJs with 1.05 nm MgO thickness [57]. If tip of CAFM is considered as a second electrode, CoFeB/MgO/tip acts as a nano scale tunnel junction. In this setup, the measured RA product for 1 nm of MgO is in the range of $10^5\ \Omega\mu m^2$ due to additional contact resistance. The R and RA product for most of the hotspots of sample Ru_0.5 at bias voltage of 10 mV are in the range of $10^6\ \Omega$ and $10^2\ \Omega\mu m^2$ respectively. This implies that the conductance is mainly due to metallic contacts. For sample Ru_0.8, the R and RA product of those hotspots which appear at low a bias voltage are still in the range of $10^8\ \Omega$ and $10^4\ \Omega\mu m^2$ respectively. The number of these hotspots is very small at low bias voltage. This means that most of the conductance is due to a thin insulating layer between the tip and the bottom electrode, but the presence of low resistance hotspots makes this barrier imperfect. The conductance in Ru_1.0 is purely due to the tunneling, because the R and RA product are larger than $10^{10}\ \Omega$ and $10^6\ \Omega\mu m^2$ respectively. The MgO film is thus already closed and a perfect insulating barrier exists at 1 nm thick MgO film.

The comprehensive analysis of the current map of sample CoFeB_0.6 indicates that although most of the hotspots have a current less than 1 nA, there is a significant number of hotspots ($150/\mu m^2$) having a current of more than 1 nA. The R and RA product of these hotspots are $10^6\Omega$ (10 mV/2nA) and $10^2\ \Omega\mu m^2$ respectively. These low resistance hotspots can thus easily short a 0.6 nm thick MgO film. Most of the conductance in CoFeB_0.8 is due to tunneling but still, there exist some hotspots (20 $/\mu m^2$) with current exceeding 300 pA at 10 mV bias voltage. The R and RA product of these hotspots are $10^7\ \Omega$ (10 mV/1.4nA) and $10^3\ \Omega\mu m^2$ respectively, which can make the working of the junction device unreliable. The MgO film is again completely closed at thickness of 1.0 nm. Only few hotspots

(4 $/\mu m^2$) indicated by a high tunneling current of 100 pA at a bias voltage of 20 mV in CoFeB_1.0. The values of R and RA product of these hotspots are $10^8\ \Omega$ (20 mV/200pA) and $10^4\ \Omega\mu m^2$ respectively. The comparison of Ru_ series and CoFeB_ series reveals that the hotspots density in MgO on polycrystalline Ru film is smaller than that of MgO on an amorphous CoFeB.

4.7 Effect of Interface Roughness in Resistance of Barrier

The variation of resistances with the thickness of MgO in both series of samples is different. The background resistances of sample Ru_0.5, Ru_0.8 and Ru_1.0 are 20 MΩ, 117 MΩ and 60 GΩ respectively. For the samples of CoFeB_series the background resistances are 15 MΩ, 31 MΩ and 1 GΩ. This variation may be due to a different growth of MgO on polycrystalline Ru and on amorphous CoFeB. In order to investigate this assumption, topographic images have been taken and the rms-roughness was evaluated. The RMS roughness versus thickness of MgO is shown in Fig. 4.12 for both series. The roughness analysis shows that MgO deposited on the amorphous CoFeB is smooth (rms- roughness 0.3 - 0.4 nm) for all thicknesses but is much larger on polycrystalline Ru in the beginning. The reason of the smooth deposition of MgO on amorphous CoFeB is the smoothness of CoFeB. There is, however, a large lattice misfit between the polycrystalline Ru and MgO (a lattice misfit of 11.3% between Ru ($10\bar{1}3$) and MgO) [91, 92].

4.8 Effect of Air on Hotspot Density

To observe the effects of air on hotspot density, all samples were scanned 5 and 15 minutes after deposition and the results are presented in Fig. 4.13. A decrease in hotspot density with time in the barriers has been observed. MgO can readily absorb water from the air because of its hygroscopic nature. Therefore, for an accurate study of the hotspots, measurements just after the deposition are very crucial. It was observed that the decrease in the hotspot density was less in the Ru_ series as compared to the CoFeB_ series i.e., Ru and CoFeB as bottom electrodes respectively. This may be due to the fact that the uncovered CoFeB sites oxidized

rapidly when it is kept in air as compared to Ru. Hence, a rapid decrease in conductance of the MgO film in case of the CoFeB as bottom electrode as compared to Ru as bottom electrode is expected.

4.9 Conclusion

In conclusion, for the electric characterization of MgO barriers by CAFM in ambient environment, a tip - sample force of 3.5×10^{-7} N was required to achieve electrical contact between tip and the MgO surface. Our results showed that at a thickness of 0.6 nm MgO, the barrier was incomplete because a large number of pinholes or hotspots existed in the barrier. The barrier starts completing around a thickness of 0.8 nm. The density of hotspots is much smaller in the case of 0.8 nm thick barrier as compared to 0.6 nm thick barrier. However, at this density of hotspots it is not possible to use the barrier for a quality devices because even a single hotspot can short the tunneling current and deteriorate the performance of the MTJs. The barrier with thickness of 1 nm was approximately free from hotspots. A complete insulating MgO barrier has been established at a thickness of 1 nm for both Ru and CoFeB bottom electrodes. A comparison of the resistance of the CoFeB_series and the Ru_series showed that the resistance for the CoFeB_series is smaller by a factor of 60 at a 1 nm thick MgO barrier. The reason of this large difference is due to the deposition of MgO on amorphous CoFeB and polycrystalline Ru. MgO grows much more continuously on CoFeB for all thicknesses but shows a rough growth on polycrystalline Ru in the beginning.

Chapter 5

Discontinuous Multilayers of CoFeB/MgO

The conductance analysis of MgO tunnel barriers with the help of a CAFM using different metallic sub-layers concluded that the MgO tunnel barrier with a thickness less than 1 nm is discontinuous. This conclusion provides a favorable ground to construct disordered (granular) system of CoFeB/MgO by sequential sputtering of MgO and CoFeB. This system is very helpful to study the spin dependent transport in CoFeB granules through the MgO barrier. In this study the thicknesses of CoFeB and MgO layers will be optimized for a disordered system to show maximum granular- (g-)TMR ratio. The results of disordered system will be compared with their structure. The role of the MgO barrier and the possible coherent transport in disordered system will be discussed.

5.1 Granular System

The granular systems of this thesis consist of magnetic particles embedded in immiscible non-metallic (insulator) matrix with a size distributed from a few nanometers to tens of nanometers. The material of the matrix helps the magnetic granules to be magnetically separated from each other to avoid the metallic percolation and to protect them from environmental degradation (e.g. oxidation) [44]. The key features of these materials are a large number of degrees of freedom like particle size, shape and size distribution, volume fraction of metal

and the nature of the interface between the metal-insulator and film thickness. To achieve the required properties, these degrees of freedom can be controlled during the sample preparation and post fabrication processes. Because of the unique microstructures of the magnetic granules, these materials exhibit some physical properties which bulk materials cannot display. For example, the magnetoresistance effect originates from the spin dependent tunneling of electrons between the granules, superparamagnetism and enhanced coercivity can be understood in uncorrelated and randomly oriented nano-scale magnetic granules. Furthermore, the granular systems show a rich variety of hybrid physical properties which are determined by the chemical composition and microstructures of the constituent elements. For example, Ag-Al_2O_3 and Ni-Al_2O_3 show high optical reflectivity and magnetic properties of Ag and Ni in combination with the mechanical hardness of Al_2O_3 [93].

The important point to keep in mind in the selection of components for granular system is their immiscible nature, because otherwise a homogeneous alloy would be formed. The recent development in film fabrication technology has made it easy to prepare different kinds of granular systems. The most commonly used techniques are sol gel, solid state reaction, pulsed laser ablation, co-sputtering and sequential sputtering.

Granular materials have been extensively studied because they have industrial application, are easy to fabricate and stable both chemically and electrically [94]. The phenomenon of spin polarized tunneling in these materials make them usable in magnetic sensors. Furthermore, their ability to store electrical charge for a long retention time makes these materials suitable for building nonvolatile memory devices [95]. In most of the granular systems the ferromagnetic granules are usually crystalline. Due to high crystalline anisotropy energy of these granules a large magnetic field is required to reach the parallel orientation of all magnetizations and a reasonable g-TMR effect. The crystalline anisotropy energy is, however, absent in case of amorphous granules and therefore the required field for the parallel orientation of their magnetic moments should be reduced.

Th CoFeB/MgO system has been found to be a proper candidate granular system to study the origin of the g-TMR and to examine the temperature dependence of the resistivity and the g-TMR near the percolation threshold. The reasons are: its amorphous nature, the low anisotropy energy and the magnetic softness of CoFeB granules and possibly coherent

electron tunneling through an MgO barrier [96, 46, 70].

The maximum value of the g-TMR determined at room temperature in some granular systems, their structure and their saturation fields are shown in the following table.

System	Structure	MR ratio	Saturation Field(kOe)	Reference
Co-Al_2O_3	Crystalline	8%	10/12	[97]
Co-SiO_2	Crystalline	4%	10	[98]
Fe-SiO_2	Crystalline	4%	15	[99]
Fe-MgF_2	Crystalline	3.5%	10	[100]
CoFeB-SiO_2	Amorphous	3.4%	15	[101]
Co-AlN	Amorphous	4.6%	10	[102]
CoFeB-MgO	Amorphous	5.9%	3	This thesis

The saturation field in all samples listed in the above table except our sample is 10 or more than 10 kOe which is very large for read head. In case of our sample the saturation field is 3 to 5 times less than that of the other systems of this kind. This low saturation field is helpful for application purposes.

5.2 Influence of CoFeB Layers Thickness on Electric and Magnetotransport Properties

The layer thicknesses of magnetic and non magnetic materials strongly influence the transport properties of discontinuous films. The size of clusters of the magnetic material and the distance between them can be controlled by varying the thicknesses of the layers. In the following section we will discuss the effect of the CoFeB layers thickness in discontinuous multilayers of CoFeB/MgO.

5.2.1 Sample Preparation

Granular samples are prepared by subsequent deposition of nine bilayers of CoFeB and MgO by DC and RF magnetron sputtering respectively. As a seed layer a 1.5 nm thick MgO layer

on a thermally oxidized silicon wafer is used. Furthermore, a cap layer is also added to avoid the oxidation of CoFeB. This study was performed to investigate the influence of the CoFeB layers thickness on the electrical transport and on the magnetoresistance. The samples prepared for this study are labeled as S_1 to S_6 corresponding to the CoFeB layers thickness ranging from 0.5 nm to 1.0 nm in 0.1 nm steps. Fig. 5.1 gives a schematic representation of the sample S_3. For transport properties measurements, samples are prepared in a rectangular shape of 2 mm $\times$ 15 mm using a mask. In this case four parallel gold stripes are sputtered on the sample surface and used as electrodes. For AGM meaurements the samples, are in the shape of a sheet of 4 mm $\times$ 4 mm and for XRR measurements, the sample are also in the form of sheets of 10 mm $\times$ 10 mm. For TEM measurements the samples are further processed by a Focused Ion Beam (FIB) with mechanical thinning and Gallium milling with a final beam voltage of 2 kV to 5 kV.

5.2.2 Structural Characterization

A granular system prepared by discontinuous metal and insulator layers is formed at the early stage of the film growth of CoFeB. The surface energy of the metal is always higher than that of insulators. Therefore, metallic CoFeB splits into nano sized granules in the begining when deposited on the MgO seed layer. By further deposition, these granules join to form a complete layer. When MgO is deposited on the CoFeB clusters, it fills the space between and above the clusters. The repetition of CoFeB and MgO layers form a granular system in which CoFeB granules are separated by the MgO matrix. The clusters of CoFeB dispersed in MgO matrix are shown schematically in Fig. 5.2. The structural properties of this granular system is investigated by HRTEM and XRR. The maximum g-TMR value in nine bilayers of CoFeB and MgO system is obtained when the thickness of each layer of CoFeB and MgO is 0.7 nm (referred as sample S_3). Therefore, the structural properties of only this sample are discussed here.

The HRTEM cross sectional image of the sample S_3 in the as prepared state is shown in Fig. 5.3. Directly on top of the amorphous layer of SiO_2 a seed layer of crystalline MgO appears. A granular system of CoFeB/MgO with small crystallites inside the multilayers can

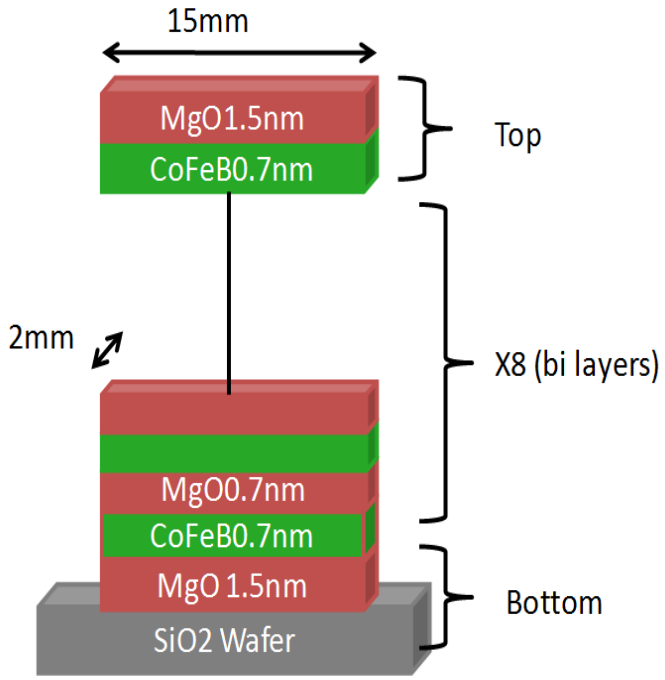

Fig. 5.1: Schematic representation of a multilayers stack of CoFeB/MgO for $d_{MgO} = 0.7nm$.

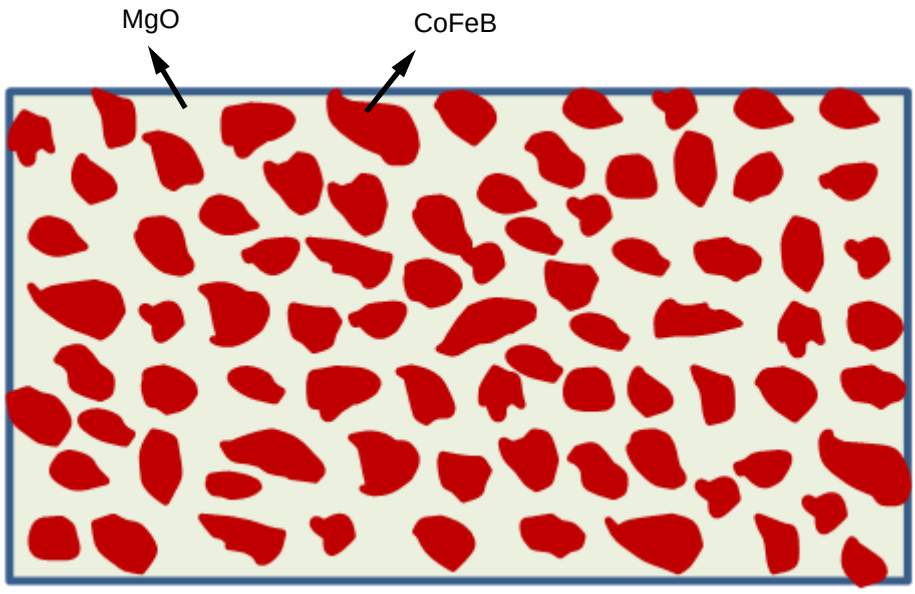

Fig. 5.2: Schematic representation of CoFeB granules dispersed in an MgO matrix.

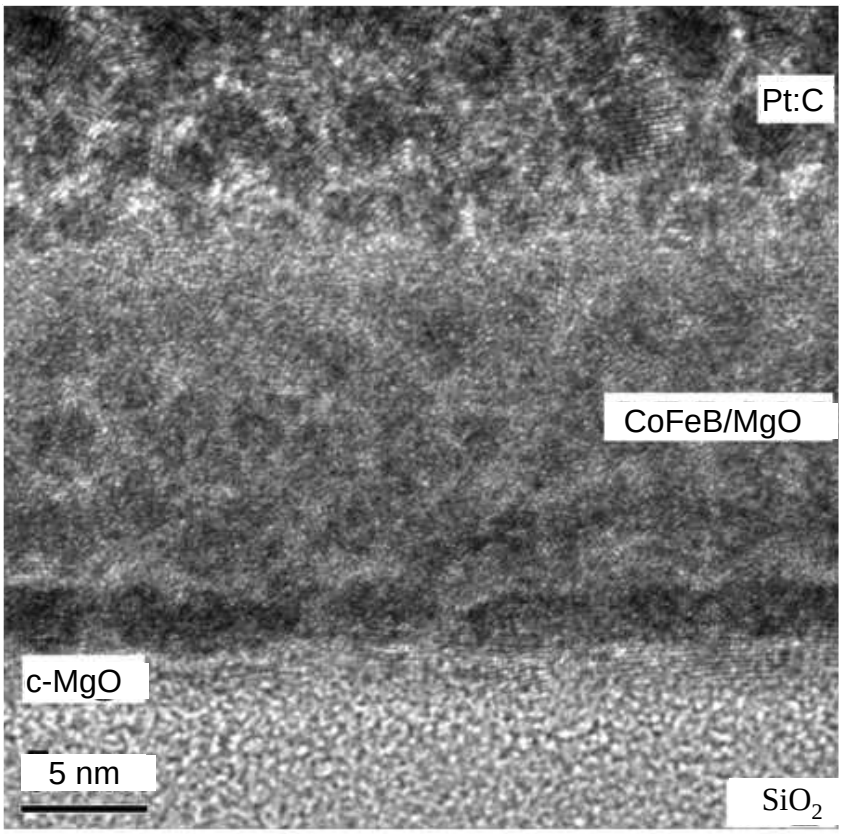

Fig. 5.3: Cross sectional HRTEM image of the as prepared CoFeB/MgO sample. Bottom is SiO_2 and the top is covered by a Pt:C granular film.

be identified. On top, the Pt:C granular film appears which was used to cover the sample in order to process the sample by Focused Ion Beam for the HRTEM characterization.

CoFeB grains with average grain size of 2-3 nm are randomly dispersed in the MgO matrix. The interface between CoFeB and MgO is not clearly visible in the as prepared state and the grains are irregular in shape. The film thickness is approximately 16.1 $\pm$ 1.7 nm which is nearly equal to the deposited thickness i.e., 14.9 nm.

Fig. 5.4 shows a HRTEM image of the same sample when annealed at 250° C for 1 hour in vacuum. The annealed sample appears similar as the sample in the as prepared state except a better contrast of the CoFeB grains and the MgO matrix. Some small granules merge with each other to form larger grains (see fig. 5.4). This reduces the bridging between grains and make them more spherical in shape.

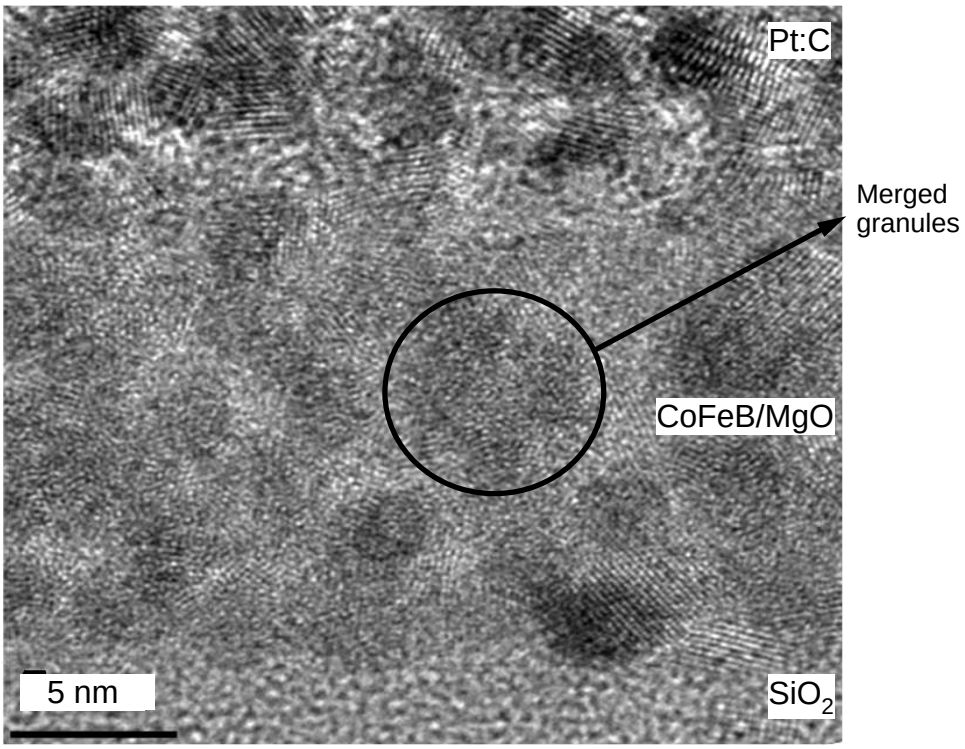

Fig. 5.4: Cross sectional HRTEM image of CoFeB/MgO sample annealed at 250° C. Bottom is SiO_2 and the top is covered by a Pt:C granular film.

The X-ray reflectometry analysis used to calculate the film thickness, bilayer thickness and interface roughness of the sample is shown in Fig. 5.5. This is done by analyzing the Kiessig fringes and Bragg peaks. Due to discontinuous structure, an analysis of the interface roughness was not possible here. The film thickness can be determined using the relation

$$d \approx \frac{\lambda}{2\Delta_{Kiessig}} \tag{5.2.1}$$

by measuring the distance between adjacent interference maxima $\Delta_{Kiessig}$ [103]. For an accurate calculation of the film thickness the *WinGixa* programme is used. From the XRR scan the film thickness of the as prepared sample is estimated as 15.145 ± 0.01 nm which is near to the deposited value i.e., 14.9 nm. The film thickness of the annealed sample is the same as that of as prepared sample. The only difference is the shape of the Kiessig fringes which is attributed to the size and shape of the granules.

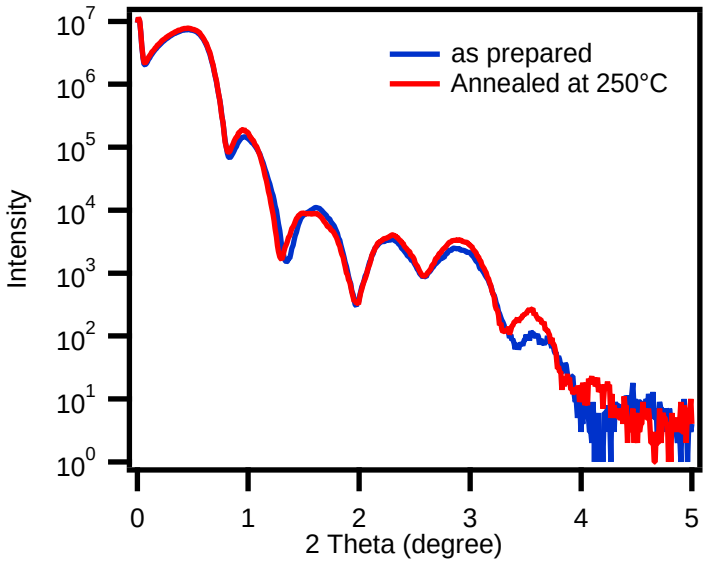

Fig. 5.5: XRR scans of the as prepared sample and a sample annealed at 250° C for $d_{MgO} = 0.7nm$.

5.2.3 Magnetic Properties

Information about the magnetic properties and the magnetic size of the granules in sample S_3 can be extracted from the magnetization measurements. These measurements were performed in a superconducting quantum interference device (SQUID) at temperatures between 350 K and 5 K. Fig. 5.6 shows a magnetization loop of sample S_3 at room temperature. The magnetization curve shows no hysteresis and follows the Langvin function of the form

$$\frac{M}{M_s} = coth\left(\frac{\mu H}{k_B T}\right) - \frac{k_B T}{\mu H} \tag{5.2.2}$$

Where M_s is the saturation magnetization, μ the magnetic moment of the unit magnetic granule, T the temperature and k_B the Boltzmann constant. The saturation magnetization M_s and the magnetic moment μ of the sample S_3 is 1070 emu/cm^3 and 10855 μ_B respectively. To calculate the magnetic size of the CoFeB granules the magnetic moment of CoFeB is taken as the average of the magnetic moments of Co and Fe i.e., (1.92 + 2.2)μ_B /2. The calculation gives a magnetic radius of 3.6 nm of the granules which is nealy double to the magnetic size measured by HRTEM images (2-3 nm).

Low field magnetization measurements were done for sample S_3 by SQUID magnetometer after the sample was cooled from 350 K to 5 K either in zero field (ZFC) or in 10 Oe (FC).

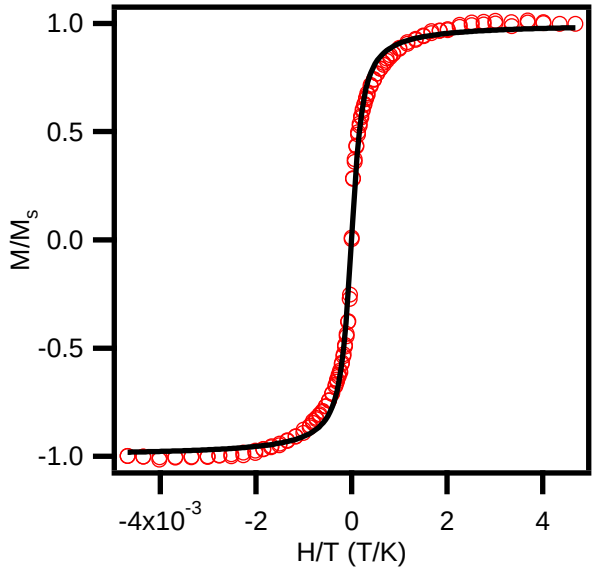

Fig. 5.6: Magnetization curve of sample S_3 after annealing at 250° C. Red markers show the experimental curve and the solid black line indicates the curve calculated by the Langvin function given by Eq. 5.2.2

For both cases the moment was recorded during the heating of the sample (from 5 K to 350 K). Fig. 5.7 shows the ZFC and FC magnetization curves of discontinuous multilayers of sample S_3 measured in 10 Oe. The ZFC-magnetization increases by increasing temperature between 70 K and 120 K. Below 70 K the magnetization of most of the granules remains blocked. Above 70 K the progressive unblocking of the moments occurres as a result of the distribution in size and shape of the magnetic CoFeB granules. The smaller units become superparamagnetic at lower temperature than the larger units. The blocking temperature $T_B \approx$ 130 K in ZFC-FC data corresponds to the temperature at which the largest unit becomes superparamagnetic. It should be noted that the FC curve does not become completely flat at low temperature, instead it shows a continuous change in magnetization below T_B. This behavior is in contrast to the one observed in Co-SiO_2 in granular films, CoFe-Ag metallic alloy and Co/SiO_2 discontinuous layers [104, 105, 106, 94]. This feature indicates the weak magnetic interaction between the magnetic granules and there is no diffusion of granules into the matrix material (immisible nature). Another important feature of the ZFC curve is the presence of a plateau representing the residual moment even at very low temperature.

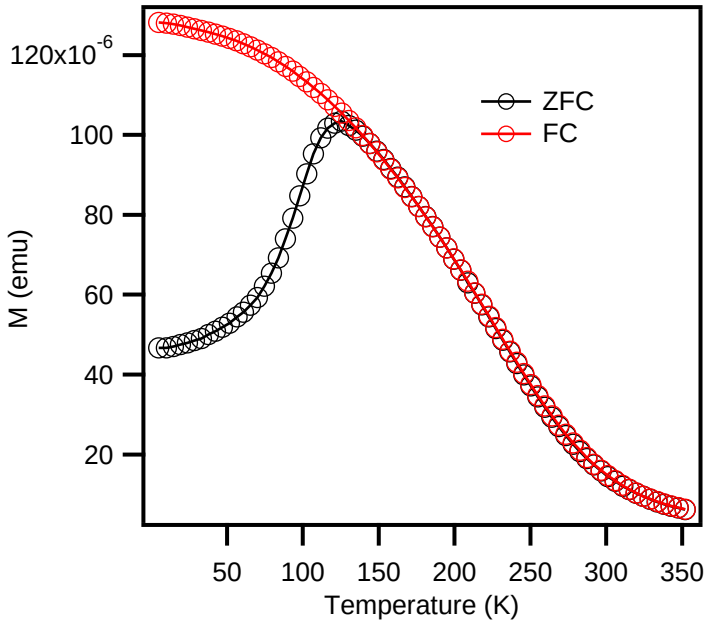

Fig. 5.7: Temperature dependence of the FC and ZFC magnetization of sample S_3. The magnetization was recorded at 10 Oe.

Normally, for granular systems the moment should approach zero because of the freezing of disordered spins at low temperature. The observed residual moment may arise because of unfrozen spins of Co and Fe in the magnetic granules.

5.2.4 Transport Measurements

Fig. 5.8 shows the dependence of the resistivity and the g-TMR value on the varying thickness of the CoFeB layers for constant thickness of MgO at room temperature. The resistivity decreases strongly with the increase of the CoFeB layers thickness as expected for percolating network of CoFeB [107]. A crossover from a granular to continuous CoFeB films is observed. This is supported by appearence of Brag peak in XRR scan.

The g-TMR value recorded for samples S_1 to S_6 are -2.6%, -3.9%, -4.6%, -2.41%, 0% and 0.08% respectively. The g-TMR magnitude first increases to a maximum of 4.6% and then decreases. The same results have been observed by X. Batlle et. al., in film where Co particles are dispressed in a matrix of Zr_2 O_3 [108]. The small g-TMR values for samples S_1

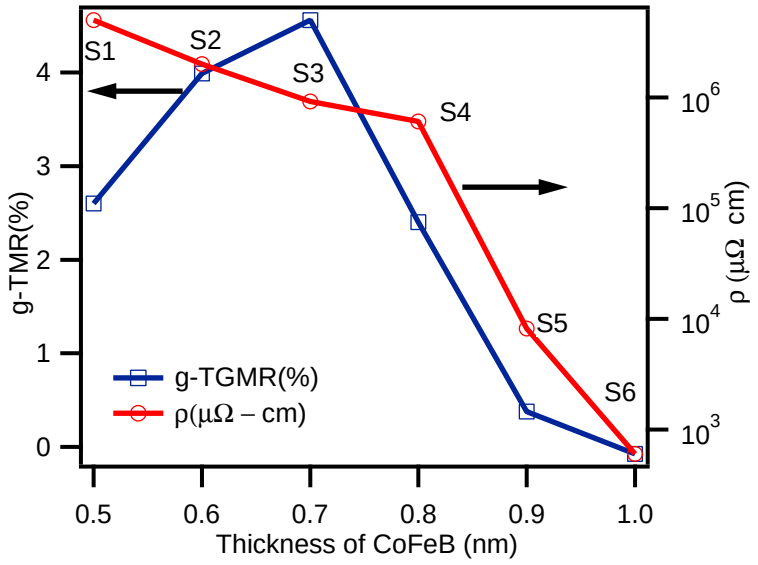

Fig. 5.8: Dependence of the g-TMR and the resistivity on the thickness of the CoFeB layers for $d_{MgO} = 0.7nm$.

and S_2 are due to the fact that the thin CoFeB films leads to a low spin dependent tunneling rate. For thicker CoFeB films (S_4 and S_5) the tunneling rate is strongly reduced due to the increasing continuity in the CoFeB network.

Fig. 5.9 shows the magnetoresistance versus magnetic field of all samples at room temperature. The g-TMR and magnetic field for samples S_1 to S_5 are drawn along the left and bottom axes respectively. The magnetoresistance and magnetic field for sample S_6 are drawn along the right and top axes respectively. A crossover is observed in sample S_6 where the magnetoresistance changes its sign as shown in Fig. 5.9. The origin of this magnetoresistance is different from the rest of the samples. The magnetoresistance in samples S_1 to S_5 is due to the spin dependent tunneling of electrons between the granules of CoFeB. But in sample S_6 the granules are joined up to form a complete films of CoFeB, therefore, the tunneling is not the dominant transport mechanism. The magnetoresistance in this sample is due to the spin orbit interaction of electron which is anisotropic magnetoresistance.

To understand the temperature dependence of the electron transport in this granular system, the electrical resistivity of samples $S_1 - S_5$ were measured between 15 K and 330 K. These results are shown in Fig. 5.10 and Fig. 5.11. All samples show a nearly exponential

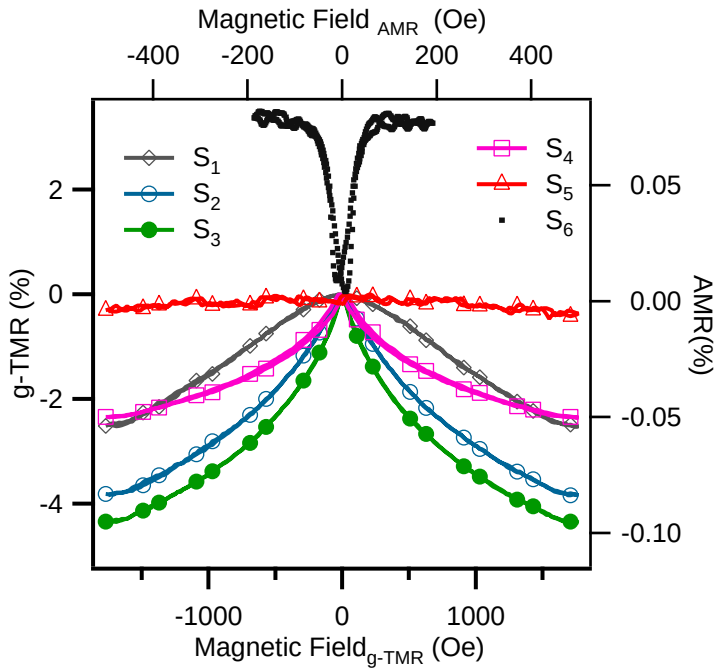

Fig. 5.9: g-TMR versus magnetic field of samples S_1 to S_5 (left and bottom axes) and AMR versus magnetic field for sample S_6 (right and top axes) at room temperature.

increase of the resistivity by decreasing temperature, which is a common feature of granular systems [109].

Sample	Resistivity at 330 K (ρ_{330})	Resistivity at 15 K (ρ_15)	ρ_{15}/ρ_{330}
S_1	4.2624$\times10^6\mu\Omega$ -cm	1.9179$\times10^9\mu\Omega$ -cm	449.95
S_2	1.7564$\times10^6\mu\Omega$ -cm	9.4594$\times10^7\mu\Omega$ -cm	53.85
S_3	1.0482$\times10^6\mu\Omega$ -cm	2.3335$\times10^6\mu\Omega$ -cm	22.26
S_4	548322$\mu\Omega$ -cm	4.1944$\times10^6\mu\Omega$ -cm	7.64
S_5	8192.75$\mu\Omega$ -cm	8833.67$\mu\Omega$ -cm	1.07

The ratio ρ_{15}/ρ_{330} represents the temperature dependence of the corresponding sample. The sample S_1 shows a strong temperature dependence of the resistivity over the entire range of temprature as shown in Fig. 5.10. The ratio of the resistivity at 15 K to the resistivity at 330 K i.e., ρ_{15}/ρ_{330} is (449.95) nearly three order of magnitude. Therefore the sample S_1 shows a strongly localized behavior. The sample S_2, S_3 and S_4 show a progressively decreasing localized behavior as the resistivity increases with the decrease of temperature

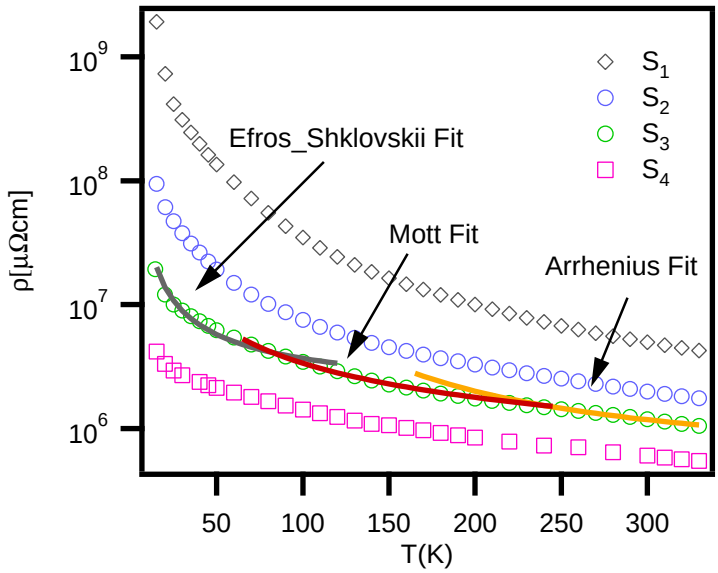

Fig. 5.10: The temperature dependence of the resistivity of samples S_1 to S_4 between 330 K and 15 K.

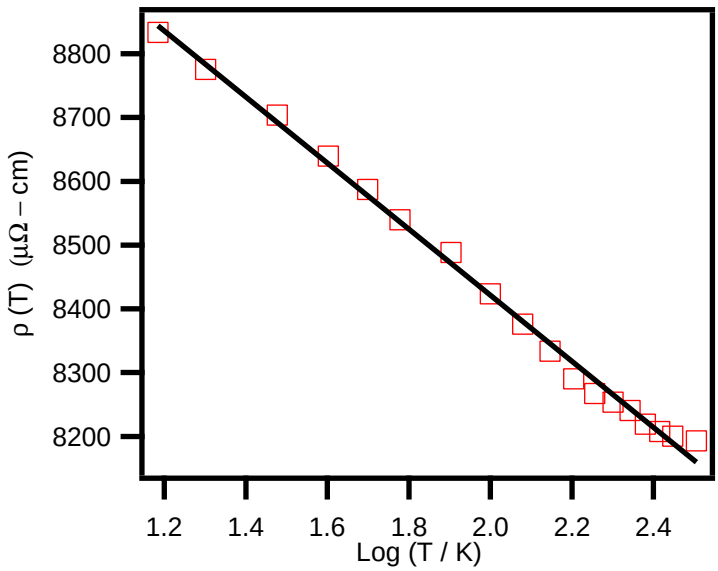

Fig. 5.11: The resistivity $\rho(T)$ of sample S_5 as a function of Log(T/K).

but the increase is not as prominent as for S_1. The ratios ρ_{15}/ρ_{330} for samples S_2, S_3 and S_4 are 53.85, 22.26 and 7.64 respectively. The ratio ρ_{15}/ρ_{330} for S_5 is 1.07 which shows a very small dependence of the resistivity on temperature. When the metal concentration is high, the transport of charge mainly takes place through the conduction bands of CoFeB. Such behavior can be seen in Fig. 5.11, where the resistivity $\rho(T)$ is plotted as a function of log(T/K). The linear dependence in this plot shows, that the increase of $\rho(T)$ is rather logarithmic than exponential, indicating that this system is not in the localized regime of conduction.

In conclusion, all samples show negative coefficients of resistivity i.e., the resistivity increases with decreasing of temperature. However, the dependence of the resistivity on the temperature decreases with increasing the layer thickness of CoFeB. Finally, when the concentration of CoFeB granules is high, they overlap each other and lose their localized character. Therefore, the transport of charge takes place through the conduction band of CoFeB.

The temperature dependence of the resistivity of a granular system follows a general relationship over a wide range of temperature:

$$\rho = \rho_{ox} exp \left(\frac{T_{ox}}{T} \right)^{1/n} \tag{5.2.3}$$

The exponent *n* has values 1, 4 and 2 for an Arrhenius Law of nearest neighbor hopping (NNH), Mott hopping (MH) and Efros Shklovskii (ES)' Law of variable range hopping (VRH) respectively. ρ_{ox} is a pre-exponential factor whose value is different for different kinds of hopping mechanisms and T_{ox} = T_{OA}, T_{OM} and T_{ES} correspond to different transport phenomena. At low concentration, the CoFeB granules are well separated from each other so that they become localized. Transport of charge takes place by hopping of electrons from occupied to unoccupied localized states. Such hopping processes in connection with doped semiconductors has been suggested in many references [110, 111]. This hopping process is temperature dependent. At high temperature the transport is carried out by hopping to the nearest sites which obeys an Arrhenius Law [112]. As temperature decreases a crossover from Arrhenius to Mott's law is observed in all samples except S_5 [50, 113]. The crossover temperature is around 200 K. Below this temperature, it is more favorable for electrons to

hop beyond nearest sites. By further decrease of the temperature the resistivity starts deviating from Mott's Law at around 60 K. This is the onset of another type of hopping mechanism which is governed by ES, Law of VRH ($n = 1/2$). This law assumes that the density of state near the Fermi level shows a Coulomb gap.

The values of the pre-exponential factors ρ_{ox} and coefficients T_{ox} coressponding to different tunneling laws for samples S_1 to S_4 can be calculated by fitting the curves (The curves are shown in Fig. 5.12 and 5.13) for different temperature regions. They are shown in the following table.

Sample	T_{OA} (K)	ρ_A $\mu\Omega$ -cm	T_{OM} (K)	$\rho_M \mu\Omega$ -cm	T_{ES}(K)	ρ_{ES} $\mu\Omega$ -cm
S_1	438.86	1.15×10^6	315495	18896	420.25	7.378×10^6
S_2	364.86	5.889×10^5	65585	47388	153.9	3.86×10^6
S_3	317.93	4.085×10^5	25445	62097	106.56	1.703×10^6
S_4	305.51	2.177×10^5	7619	72923	32	9.41×10^5

The g-TMR dependence on temperature was already shown in Fig. 5.9. The g-TMR is zero at room temperature for sample S_5 and remains the same even at 15 K. For sample S_4, the g-TMR value is 2.2% at room temperature and slightly increases at lower temperature. In samples with CoFeB layer thickness 0.7 nm and less (sample S_3 to S_1), the CoFeB granules are as much separated from each other that they form a network of nanometer sized tunnel junctions through the surrounding MgO matrix. At low temperature a remarkable increase in g-TMR is observed which is due to higher order tunneling of electrons between the CoFeB granules [114]. This will be explained in section 5.4

5.3 Influence of the MgO Layer Thickness on Electric and Magnetotransport Properties

5.3.1 Sample Preparation

The samples were prepared by the same procedure as described in section **??**. The only difference in these samples is that the thickness of MgO layers is changed and CoFeB layers

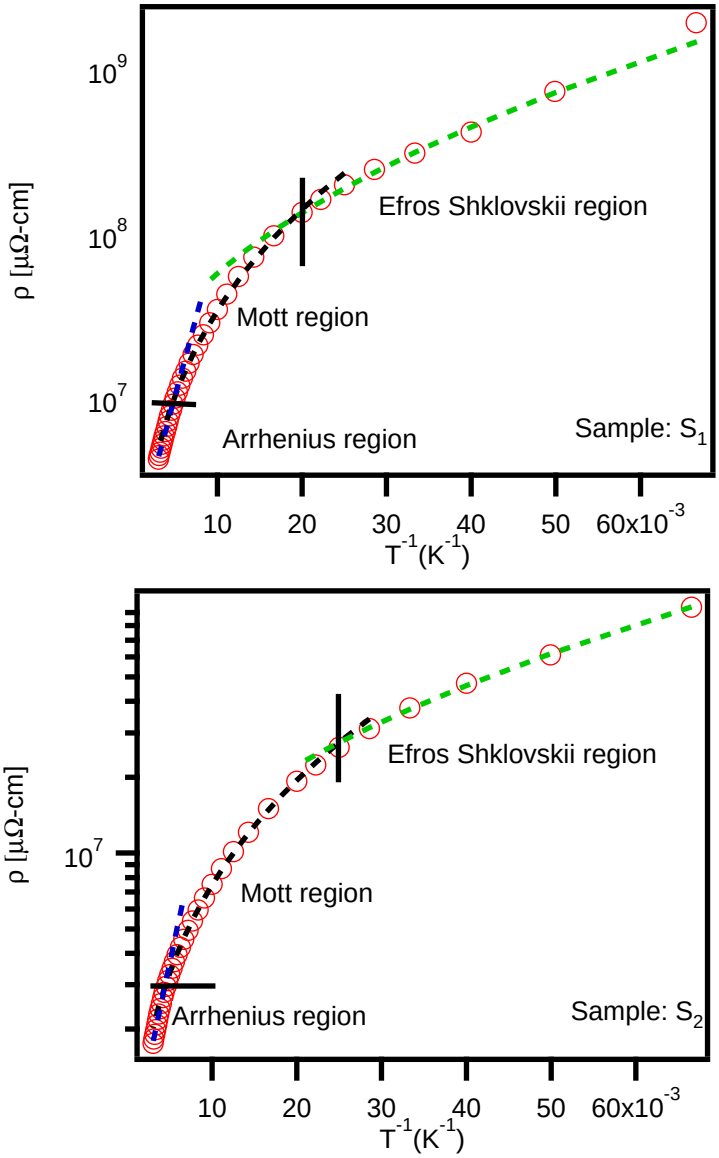

Fig. 5.12: Dependence of the resitivity on T^{-1} of samples S_1 and S_2 along with the fitting curves of the tunneling laws in different temperature regions.

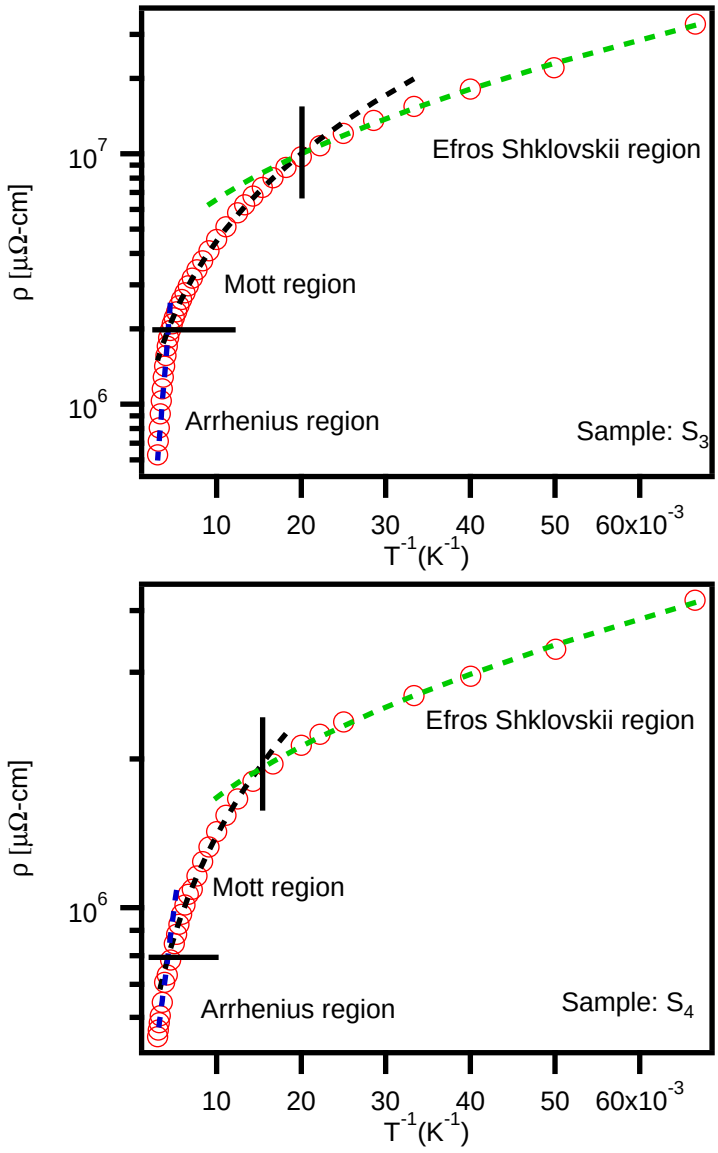

Fig. 5.13: Dependence of the resitivity on T^{-1} of samples S_3 and S_4 along with the fitting curves of the tunneling laws in different temperature regions.

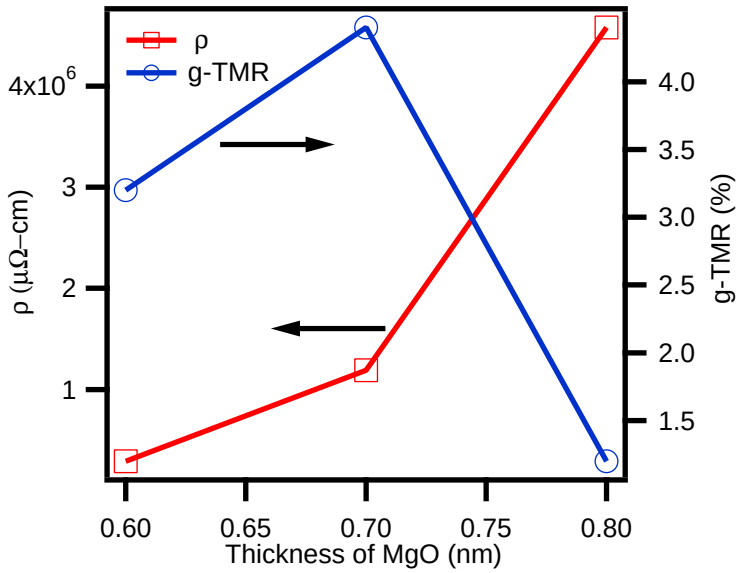

Fig. 5.14: Dependence of the resistivity and g-TMR versus thickness of MgO at room temperature for $d_{CoFeB} = 0.7nm$

thicknesses are kept constant at 0.7 nm. The samples are labeled as MgO_6, MgO_7 and MgO_8 corresponding to MgO layers thickness of 0.6 nm, 0.7 nm and 0.8 nm, respectively.

5.3.2 Results and Discussion

The resistivity of the samples MgO_6, MgO_7 and MgO_8 is measured by applying a bias voltage of 100 mV at room temperature using a four point contact technique. The values of the resistivity of these samples at room temperature are $2.8932\times10^5\mu\Omega$ -cm, $1.1889\times10^6\mu\Omega$ -cm and $4.5812\times10^6\mu\Omega$ -cm respectively. The magnetoresistance of these samples was also measured by applying a magnetic field of $\pm$ 1770 Oe in plane of the film. The magnetic field and current are parallel and in the film plane. The g-TMR values of MgO_6, MgO_7 and MgO_8 are 3.2%, 4.6% and 1.2% respectively. The results are shown in the Fig. 5.14.

The increase in resistivity with increasing MgO thickness is due to the fact that transport is dominated by the activated tunneling of electrons between the CoFeB granules through an MgO barrier, where the barrier gets thicker with increasing MgO thickness. Note that this increase in resistivity is not as pronounced as with decreasing CoFeB thickness (Fig.

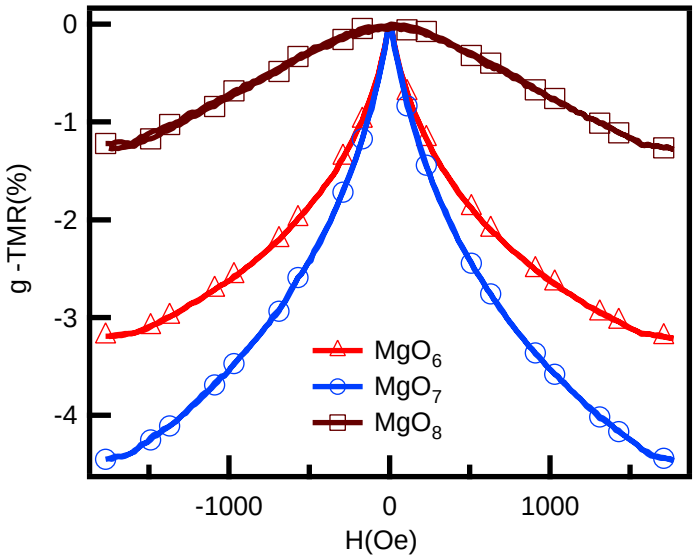

Fig. 5.15: The g-TMR versus magnetic field for samples MgO_6, MgO_7 and MgO_8 at room temperature

5.8). The size of the granules is expected to be same in all three samples because the layers thickness of CoFeB are same for all samples. However, the separation at least in one direction between the CoFeB granules is different for different thickness of MgO layers. Therefore, the tunneling resistance for thinner MgO barrier is smaller than that of thicker MgO barrier.

The g-TMR value first increases with the thickness of MgO and reaches its maximum value of 4.6 % at $d_{MgO} = 0.7nm$ and then decreases for further increasing thickness of MgO. Although no saturation was reached , this tendency seems to be clear from Fig. 5.15. This change in g-TMR with the thickness of MgO is due to the fact that the hopping of charges between the granules in sample MgO_8 is through a thick tunnel barrier and in sample MgO_6 is small because the number of tunneling events are reduced [115]. The shapes of magnetoresistance curves shown in Fig.5.15 are also very interesting. The magnetoresistance is highly field sensitive around zero field for the MgO_7 sample. The sensitivity decreases with increasing thickness of MgO. This can be explained as follow: one of the necessary conditions to observe a maximum g-TMR in ferromagnetic-insulator granular films is the superparamagnetic nature of the magnetic granules at room temperature [116]. The size of the magnetic granules and the distance between them both play an important role in the oc-

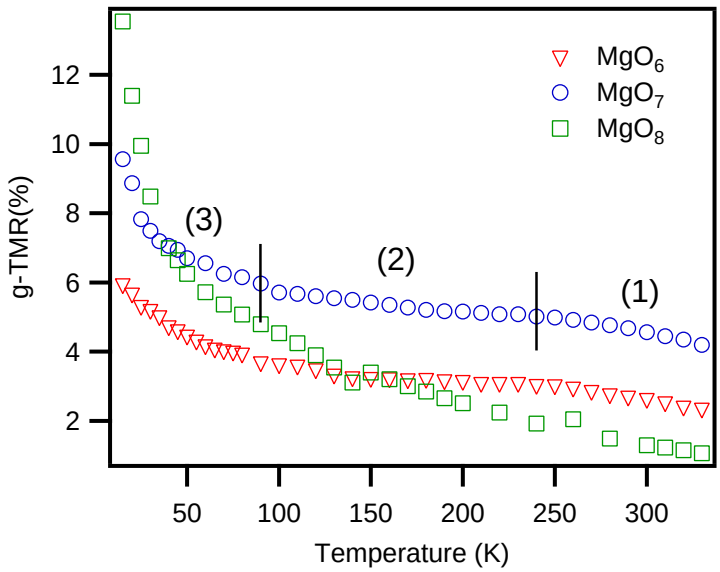

Fig. 5.16: The tempeature dependent g-TMR for samples MgO_6, MgO_7 and MgO_8. The different regions (1) - (3) are discussed in the text.

currence of superparamagnetism [109]. The distance between the magnetic granules should be such that the interactions between their magnetic moments become negligible. In the MgO_8 sample the CoFeB magnetic granules are more separated and the interaction between them is negligibly small, therefore, a larger field is required to align them in parallel.

The temperature dependence of the resistivity and the g-TMR of samples MgO_6, MgO_7 and MgO_8 were also measured between 330 K and 15 K. All samples show an exponential increase in the resistivity with temperature which is a common feature of granular systems [109]. The results are shown in the Fig. 5.16 and Fig. 5.17. The values of resistivities at 330 K and 15 K and their ratios for samples MgO_6, MgO_7 and MgO_8 are given in table below

Sample	Resistivity at 330 K	Resistivity at 15 K	ρ_{15}/ρ_{330}
MgO_8	$3.7983\times10^{6}\mu\Omega$ -cm	$2.09194\times10^{10}\mu\Omega$ -cm	5514
MgO_7	$1.0482\times10^{6}\mu\Omega$ -cm	$2.3335\times10^{6}\mu\Omega$ -cm	22.26
MgO_6	$2.2992\times10^{5}\mu\Omega$ -cm	$3.36169\times10^{6}\mu\Omega$ -cm	14.62

At the room temperature the maximum g-TMR is achieved for sample MgO_7. The g-TMR of MgO_8, however, incereases sharply with decreasing of temperature. There are three promi-

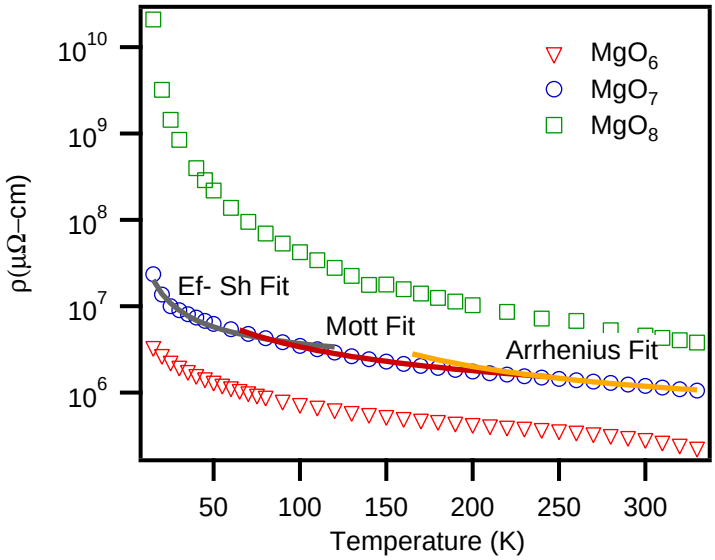

Fig. 5.17: The temperature dependence of the resistivity of samples MgO_6, MgO_7 and MgO_8 between 330K and 15 K

nent regions in the graph for MgO_7. At high temperature (1) the g-TMR is slightly temperature dependent, at intermediate temperature (2) it remains the same between 220K and 70K and for low temperature (3) it is strongly temeperature dependent. The sample MgO_6 shows a simillar but smaller temperature dependence as that of MgO_7 nearly for the whole range of temperature. We will discuss the temperature dependence of the g-TMR in the light of references of many models proposed for the electron transport in granular films in the next section. The values of the pre exponential factors ρ_{ox} and coefficients T_{ox} corressponding to different tunneling laws for different samples can be calculated by fitting the curves for different temperature regions. The results are shown in the following table.

Sample	T_{OA} (K)	ρ_A $\mu\Omega$-cm	T_{OM} (K)	ρ_M $\mu\Omega$ -cm	T_{ES}(K)	ρ_{ES} $\mu\Omega$ -cm
MgO_8	——	——	581540	6723.2	1100	1.9492×10^6
MgO_7	317.93	4.085×10^5	25445	62097	106.56	1.703×10^6
MgO_6	760.95	2.3013×10^4	111.3	26135	53.79	4.5647×10^5

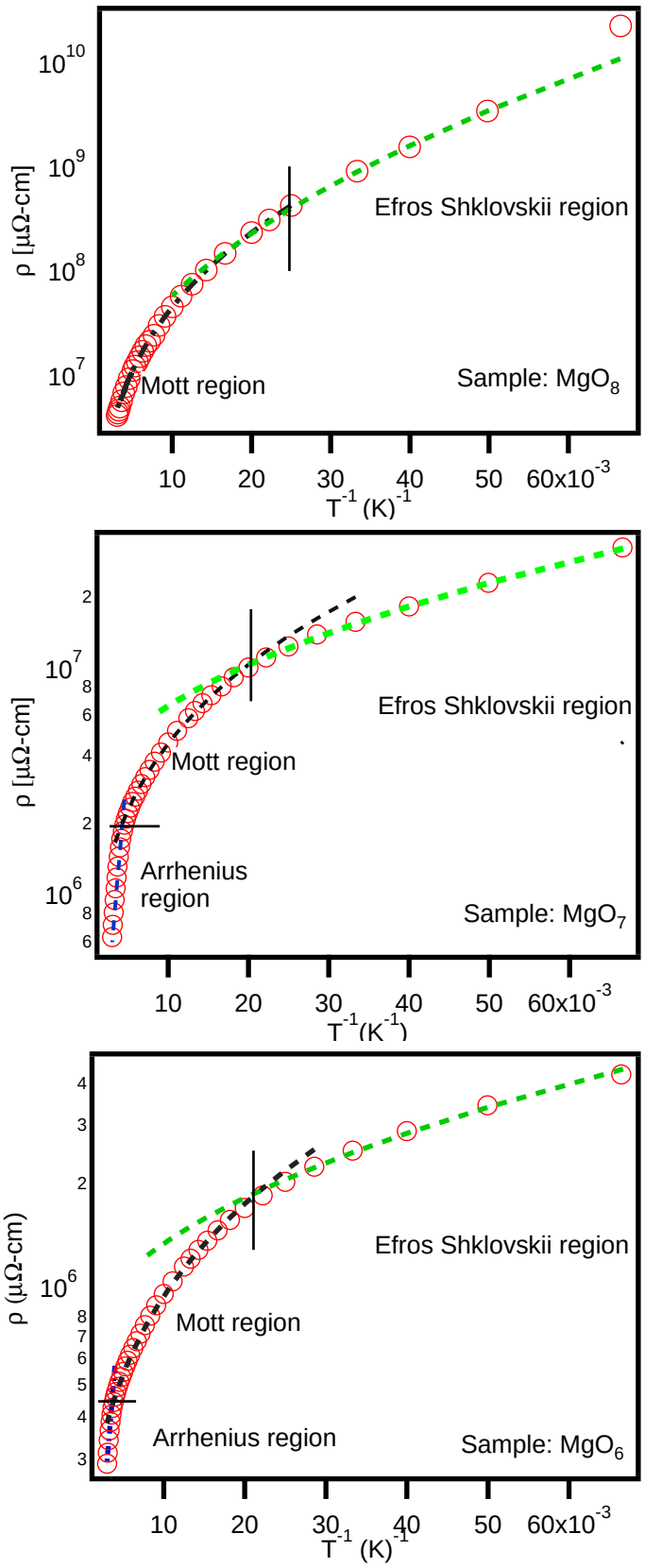

Fig. 5.18: Dependence of resitivity on T^{-1} for samples MgO_6, MgO_7 and MgO_8 along with the fitting curves of tunneling laws in different temperature regions.

5.4 Higher Order Tunneling at Low Temperature

At low temperature, a remarkable increase in g-TMR has been observed in all these samples, which is explained as follows: According to B. Abeles et. al., at low temperature the conductivity of a non-magnetic granular system depends on the temperature as $\rho \propto exp\left(\frac{1}{T}\right)^{1/2}$ [109]. This explanation was based on the assumptions that the granules are equal in size *d* and separated by a barrier thickness *s* and the ratio s/d for a given metal -insulator composition remains constant. Afterward, J. Inoue et. al., extended this model to magnetic granular systems including the effect of spin dependent tunneling of electrons among the granules and yielding the magnetoresistance as:

$$\frac{\Delta\rho}{\rho} = \left(\frac{P^2}{1+P^2}\right) \tag{5.4.1}$$

where *P* is spin polarization [117]. These models were based on the assumption that the tunneling was only possible between granules of the same size. However, the broad distribution of granular sizes is inevitable in granular systems. Mitani et.al, and Zhu et.al, studied Co-AlO_x and Fe-AlO_x granular films and measured the temperature dependent resistivity and magnetoresistance [114, 118, 119]. They found that the resistivity and the magnetoresistance are both temperature dependent and introduced the idea of higher order tunneling. The large grains are well separated from each other and there may be small granules in between them. In "ordinary" tunneling electrons tunnel from large granules to small ones which are nearest to them; at low temperature however, the tunneling is governed by higher order processes. This higher order tunneling process has been schematically represented in Fig. 5.19. During this process, an electron is transferred from a large charged granule to another large neutral granule through the small granules in between them. Using this concept Mitani et. al., derived

$$\frac{\Delta\rho}{\rho} = 1 - \left(1 + m^2P^2\right)^{-(n^*+1)} \tag{5.4.2}$$

with $n^* = \left(\langle E_c\rangle / 8\widetilde{\kappa}\langle s\rangle T\right)^{1/2}$ and $\widetilde{\kappa} = \kappa + (1/4\langle s\rangle)\, ln\left[(g/\pi)^2 + \left(\langle E_c\rangle / 2\pi T\right)^2\right]$. Where $m = \frac{M}{M_s}$ is the magnetization normalized to the saturation magnetization, κ is the tunneling parameter related to the barrier height ($\kappa = \frac{2m^*\varphi}{\hbar}$, m^* is the effective mass of electron, φ is

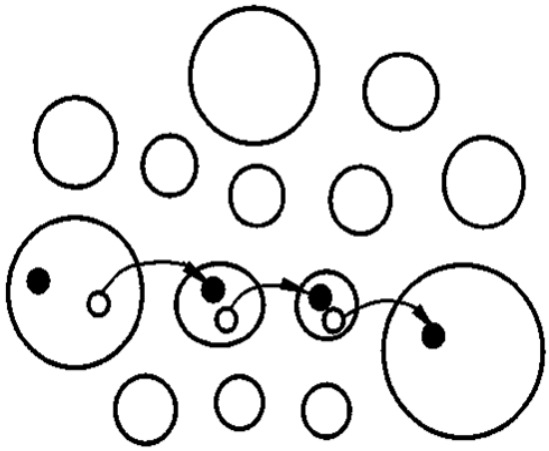

Fig. 5.19: Schematic representation of a higher order tunneling process in which an electron transferred from a large charged granule to another large neutral granule through small granules in between them [114].

the barrier height and $\hbar$ is the Plank's constant), $\langle E_c \rangle$ is the average charging energy $\langle s \rangle$ is the average grain spacing and *g* is the temperature dependent factor arising from the electron and hole excitation in the energy interval of πT around the Fermi level [120]. When the spin polarization is very small then the above equation reduces to

$$\frac{\Delta\rho}{\rho} = m^2 P^2 \left(1 + \sqrt{C/T}\right) \tag{5.4.3}$$

Where $C = \langle E_C \rangle / 8\tilde{\kappa} \langle s \rangle$ and P and C are used as fit parameters. Our experimental result for sample S_3 fits well to the equation 5.4.3 as shown in Fig. 5.20. The resulting value of the spin polarization is 19% which is small as compared to the recently reported value for CoFeB i.e. 53% [121]. The reason for this difference may be due to the fact that in our case the barrier between the two granules is not uniform and the sample has not been annealed to the crystallization temperature of CoFeB. Furthermore our sample is a complicated structure of a large number of tunnel junctions and the result reflects the average of all the junctions in the network.

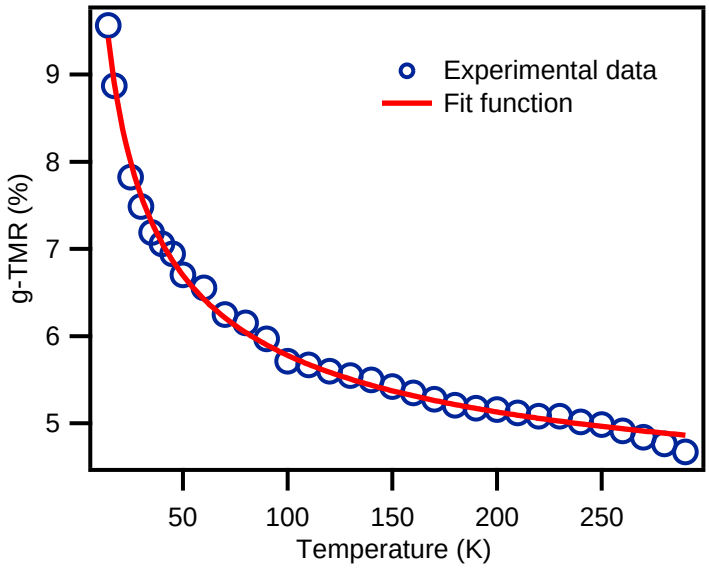

Fig. 5.20: Temperature dependence of the g-TMR of sample S_3. Markers belong to the experimental data and the solid line is a fit of equation 5.4.3.

5.5 Coulomb Gap

The crossover from Mott-type to ES-type hopping suggests a coulomb gap in this material. Therefore, tried to measure the coulomb gap energy in this multilayer system. Different samples were cooled to a temperature lower than 4.2 K where a considerable increase in resistance has been observed. The value of this resistance was more than the upper limit of Keithly 2000 multimeter (106 MΩ). However, the sample MgO_6 when cooled to 1.25K in a ^{4}He cryostat showed some promising results. Fig. 5.21 shows the I-V curve and the conductance dI/dV at this temperature. The full width at half maximum corresponding to the gap energy ($\Delta V_{1/2}$) is found to be 10 meV. In VRH, some of the localized states around the Fermi level are involved in the hopping process; these states are called optimal bands. The full width energy of these bands is given by the relation $E_c = \xi_c \times T$ where ξ_c is called the critical parameter which can be calculated by the equation 5.5.1 using experimental data [122]

$$\xi_c = \sqrt{\frac{T_{ES}}{T}} = ln\left(\frac{R_T}{R_o}\right) \tag{5.5.1}$$

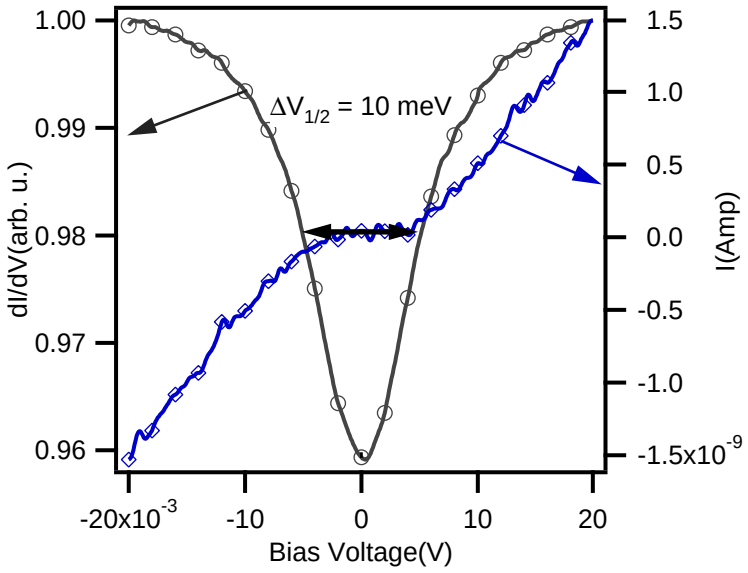

Fig. 5.21: dI/dV versus V and I versus V curve of sample S_3 at 1.25 K.

At $T = 1.25K$ and with $T_{ES} = 53.79K$, we get $\xi_c = 6.56$ and therefore $E_c = 8.2K = 0.707meV$. This satisfies the condition for ES law i.e., $E_c << \Delta V_{1/2}$. The crossover temperature T^* is given by the relation

$$T^* = \frac{1}{T}\left(\frac{\Delta V_{1/2}}{2k_B}\right)^2 \tag{5.5.2}$$

which gives T^* = 63.5 K. Within the accuracy of the fitting, this theoretical value agrees to our experimental value $T_{expt.} = 60K$.

5.6 Effect of Annealing

5.6.1 Effect of Long Duration Annealing

To investigate the effect of long duration annealing at a constant temperature, the sample S_3 was annealed in a vacuum furnace at a pressure of 2×10^{-7} mbar at 250° C in four steps. The duration of each annealing step was 5 hours. Fig. 5.22 shows the variation of the resistivity and the g- TMR after each annealing step. Both the resistivity and the g-TMR ratio increased first and reached maximum values up to $2.22 \times 10^6 \mu\Omega$ -cm and 5.9% respectively.

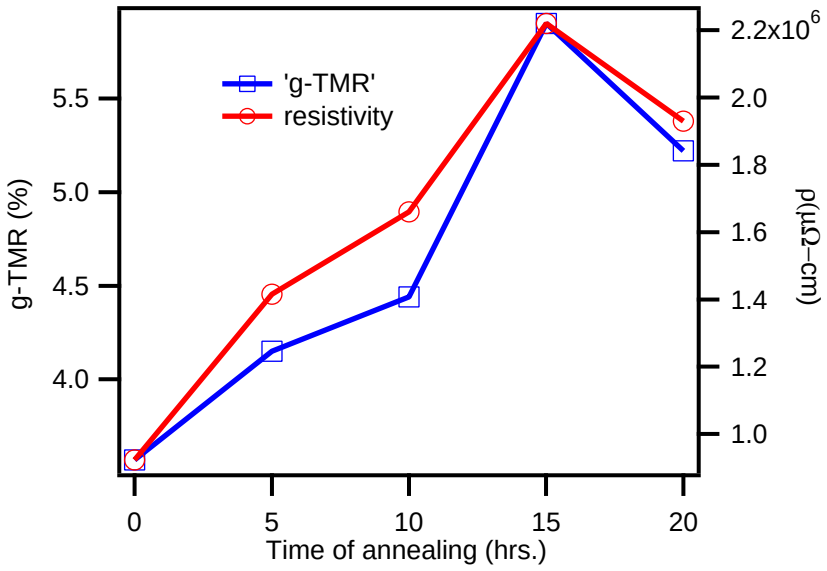

Fig. 5.22: The resistivity and g-TMR of sample S_3 after 5 hours, 10 hours, 15 hours and 20 hours of annealing at constant temperature of 250^o C.

After deposition, the films are under residual stress and there are bridges among the neighboring granules, which decrease the resistivity and the g-TMR value. The annealing is used to relieve the residual stress and it reduces the bridging among neighboring granules by sharpening the interface between granules and insulating matrix [94]. The magnetic granules become well separated from each other and their size increases which results in a decrease of the charging energy E_c. In accordance to this, it was observed that the increase in resistivity and g-TMR at low temperature were more prominent in annealed sample as compared to as prepared sample.

5.6.2 Effect of High Temperature Annealing

In order to study the effect of high temperature annealing the sample S_3 was annealed at 300° C. The structural and magnetic properties were studied by XRR scans, TEM and magnetization measurements at room temperature. The electrical and electromagnetic properties were also studied. The XRR scans of as prepared and of samples annealed at 300° C are shown in Fig. 5.23. The film thickness of the as prepared sample is 15.145 nm which increases to

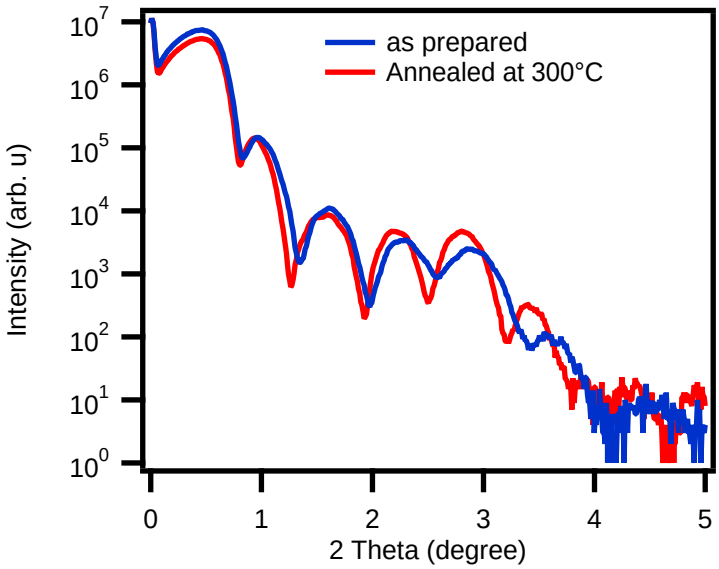

Fig. 5.23: The XRR scans of as prepared sample and sample annealed at 300° C.

15.564 nm on annealing at 300° C. This is attributed to an increase in size and crystallization of CoFeB granules. The increase in magnitude of Kiessig fringes is due to increase in interface and surface roughness [103]. TEM and diffraction images of sample S_3 annealed up to 300° C are shown in Fig. 5.24. The CoFe granules appear to be completely crystalline. The different lattice contrast is the result of different tilts of single granules. Diffraction image belongs to a large area beginning from the Si substrate into the carbon glue. Such a large area is the limit of the smallest available Selected Area Diffraction (SAD)-aperture of the TEM. The diffraction pattern is not very clear due to this large SAD-aperture. The prominent black diffraction spots (circled in Fig. 5.24 b) belong to Si substrate and the small scattered spots belong to granules tilted in different directions.

The magnetization versus magnetic field curves of sample S_3 in as prepared state and annealed state at 300° C are shown in Fig. 5.25. The saturation magnetization M_s (1125 emu/cm^3) decreases a little (1070 emu/cm^3) when annealed at 250° C but increases considerably (1600 emu/cm^3) on annealing at 300° C. This behavior is contrary to the many granular thin films where M_s decreases due to occurence of interdiffusion during annealing [123]. The possible reason of this unusual increase upon annealing at 300° C might be the diffusion of boron atoms away from CoFeB. This decreases the magnetic impurities and thus

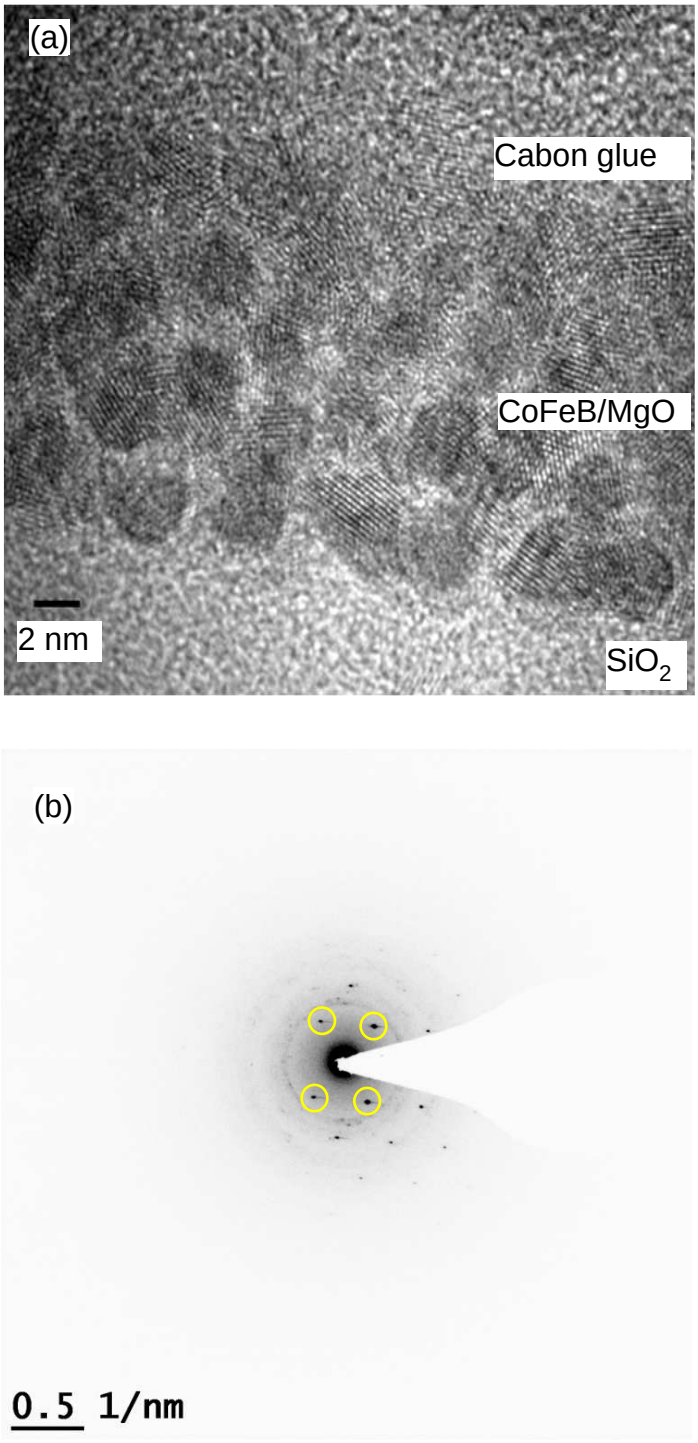

Fig. 5.24: Cross sectional HRTEM image of CoFeB/MgO sample annealed at 300 ° C (a) and diffraction image (b) begining from Si into the Carbon glue. The circled diffraction spots belong to the Si substrate.

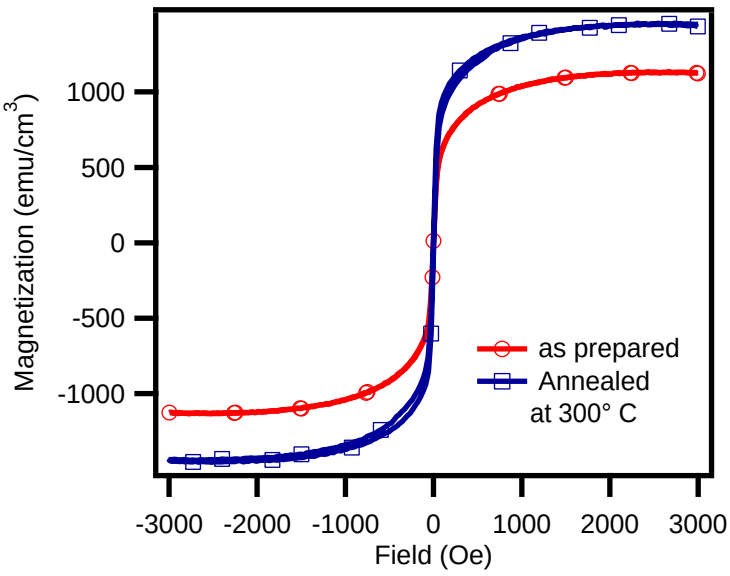

Fig. 5.25: Magnetization loop of the as prepared sample and the same sample annealed at 300° C.

inreases the magnetic moment. The rigid bond model suggests that the moment of transition metals like Co and Fe increases on decreasing metalloid (boron) concentration [124].

The g-TMR ratio of sample S_3 first increases with increase of the annealing temperature and reaches a maximum value of 4.95% at 275° C. A rapid decrease in g-TMR has been observed with further increase of temperature in all samples. But the resistivity continuously increases with the increase of temperature. The results are shown in Fig. 5.26. The increase in resistivity and decrease in g-TMR above 275° C is due to the crystallization of CoFeB granules. To achieve a high TMR value on crystallization of CoFeB granules due to coherent tunneling highly oriented (001) MgO barrier/CoFeB crystalline electrodes are required [125]. However, in our case the granules are tilted in different lattice direction which has been observed in differaction images shown in Fig. 5.24. Therefore, coherent tunneling between CoFeB granules through the MgO barrier has not been observed in our samples.

5.7 Conclusion

In conclusion, granular films of CoFeB and MgO were prepared by sequential deposition of MgO and CoFeB layers in the form of discontinuous multilayer. XRR and TEM mea-

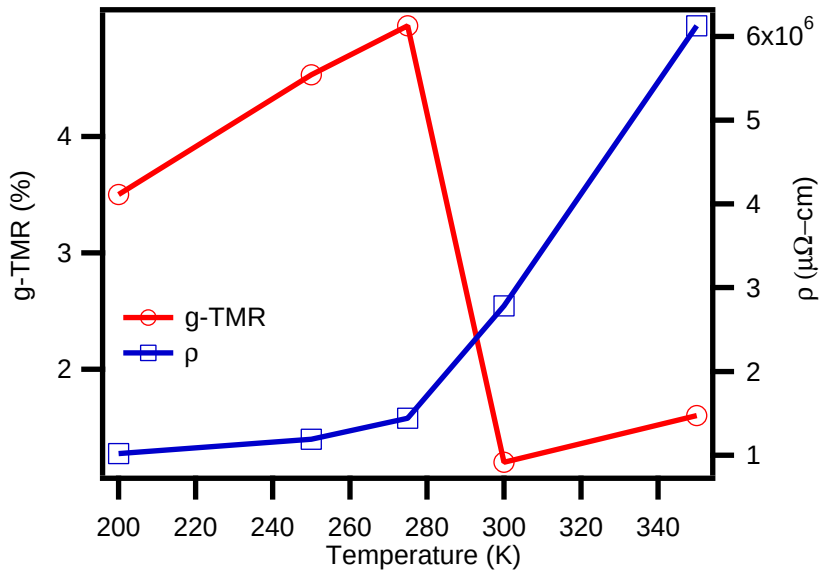

Fig. 5.26: The resistivity and g-TMR of sample S_3 annealed at different temperature.

surements showed the granular nature of the samples with 2-3 nanometer sized granules of CoFeB dispersed in the MgO matrix. Resistivity and magnetoresistance measurements carried out by four probe technique showed that the magnetoresistance diminished for very low and high CoFeB concentration and changed to mettalic AMR when metallic percolation of CoFeB was reached. The CoFeB and MgO layers thicknesses were optimized to achieve maximum g-TMR value.

AGM and SQUID magnetometers were used to investigate the magnetization of the samples. The measurements demonstrated the superparamagnetic nature of the magnetic entities at room temperature. FC-ZFC measurements showed a reversible magnetic behavior near the percolation threshold below room temperature. This means that a phase transition from ferromagnetism to superparamagnetism was observed around a temperature of 130 K.

A well annealed sample at 250° C near the percolation threshold showed both enhanced g-TMR value and resistivity at all temperatures which was due to the improvement of the microstructures by annealing. However, a decrease in g-TMR value was observed by annealing to 300° C which was associated to the crystallization of CoFeB granules tilted in different lattice orientations.

An exponential increase in the resistivity with decreasing temperature observed in this

system followed the tunneling laws of nearest neighbor hopping, Mott hopping and Efros-Shklovskii variable range hopping. The three temperature regions were prominent near the percolation threshold and therefore tunneling of the electrons followed different transport mechanism in different temperature regions. A sharp increase of the g-TMR observed at low temperature was attributed to the higher order tunneling of electrons between large granules of CoFeB via small granules situated in between them. The Coulomb gap energy was measured by cooling the sample below 4.2 K in He cryostat. The onset temperature of Efros Shklovskii region was calculated which agreed with our measured temperature.

Chapter 6

Summery and Outlook

Magnesium oxide is extensively used as barrier material in MTJs after the discovery that an MTJ with a highly -(001) oriented MgO barrier produces ultrahigh TMR values. Many thousands % have been predicted in MTJs with MgO. However, 500% TMR value has been achieved experimentally. Thus the difference in theory and experiment is very high. The main source of this difference is the tunneling through the barrier material. Large changes in electron transmission occur due to defects with localized electron states, fluctuation in thickness and pinholes in the barrier layer. All these defects are buried inside very thin MTJ layers so it is difficult to investigate them with usual techniques. CAFM technique has been used to investigate the MgO barrier in this thesis.

At the first stage of this work MgO barriers using Ru bottom electrode have been investigated by CAFM. Different imaging parameters like contact resistance, contact area, imaging force and bias voltage were optimized for this barrier. Using these optimized parameters, the electrical integrity of the MgO barrier in MTJs was studied. For this purpose half finished MTJs were used. Different thicknesses of MgO were studied and results of their resistances (R) and resistance Area product $(R \times A)$ were compared with CAFM measurements.The growth of the barrier on polycrystalline Ru and amorphous CoFeB was also a part of this study. A statistical model proposed by F. Bardou for the study of the tunneling transmission variations due to inhomogeneity of a barrier was used to quantify the quality of the barrier. A homogeneous and electrically high quality barrier was achieved at a thickness of 1 nm.

Local tunneling spectroscopy of ultra thin MgO barrier with the help of an improved

CAFM will be an interesting technique for the future studies. This can be applied to investigate local electrical properties such as local dielectric breakdown voltage, time dependent dielectric breakdown, carrier transport and interface states. The dielectric degradation process can also be investigated by studying I-V characteristics. This will help to understand the breakdown mechanism in MgO barrier locally.

In order to study the spin transport phenomenon in CoFeB through MgO barrier, disordered system of CoFeB and MgO in the form of CoFeB granules embedded in a MgO matrix was prepared. The thickness of the CoFeB and MgO layers were varied to achieve a maximum g-TMR. The value of the g-TMR is assumed to be related to the features of CoFeB grains like size, shape and size distribution. Concerning the effect of these features, most of the experimental work has been focused on post deposition annealing.

The samples were studied for long duration annealing at a particular temperature and increase in the g-TMR value and resistivity has been observed for a certain duration of annealing which is associated to an increase in the grain size and an improvement in the grains/barrier interface. A decrease in both g-TMR value and resistivity has been observed after further annealing which was due to reaching the metallic percolation of CoFeB grains.

The samples were also studied after annealing at high temperature. An increase in the g-TMR and resistivity with temperature was observed up to $275\,^{\circ}$ C. However, a decrease in g-TMR and an increase in resistivity after annealing at $300\,^{\circ}$ C has been observed. These changes are the result of crystallization of CoFeB granules.

Different transport phenomena in connection with the tunneling laws for semiconductors were identified in this disordered system and the Coulomb gap energy was measured. The magnetic characterization showed a magnetic reversibility at temperature below room temperature and superparamagnetic behavior at room temperature.

The occurrence of a single pinhole in planar junctions can produce a short for the current and stop it from functioning. Therefore, the reduced performance of planar junctions is a major problem posed by the presence of pinholes. On the other hand, there exists no continuous path for electrons in granular films. The conduction electrons have to tunnel through the MgO insulator. This implies that tunneling is achievable even in the presence of a finite density of pinholes. Moreover, in case of granular films the increased resistivity to

the large applied voltages is attributed to the distribution of voltage over a large number of junctions. Therefore, the value of the bias voltage for a tunnel junction is reduced and the dielectric break down can be avoided.

The saturation magnetic field for the parallel alignment of the magnetic moments in disordered systems is very large. This large value of the saturation field is great hindrance to use them in data storage devices. The saturation field of CoFeB/MgO, however, is three to five times less than comparable systems. This small value of saturation field is helpful for application purposes.

Granular films have wide spread potential applications in magnetic sensors technology and magnetic data storage devices. Further studies of resistive switching and microwave permeability measurements in these films will make them highly attractive for applications in resistance random access memory and microwave absorbers.

Bibliography

[1] SA Wolf, DD Awschalom, RA Buhrman, JM Daughton, S. Von Molnar, ML Roukes, AY Chtchelkanova, and DM Treger. Spintronics: A spin-based electronics vision for the future. *Science*, 294(5546):1488–1495, 2001.

[2] PP Freitas, R. Ferreira, S. Cardoso, and F. Cardoso. Magnetoresistive sensors. *Journal of Physics Condensed Matter*, 19(16):165221, 2007.

[3] J. R. Childress and Jr R. E. Fontana. Magnetic recording head sensor technology. *Comptes Rendus Physique*, 6:997, 2005.

[4] SN Piramanayagam. Perpendicular recording media for hard disk drives. *Journal of Applied Physics*, 102:011301, 2007.

[5] G. Binasch, P. Grünberg, F. Saurenbach, and W. Zinn. Enhanced magnetoresistance in layered magnetic structures with antiferromagnetic interlayer exchange. *Phys. Rev. B*, 39:4828, 1989.

[6] M.N. Baibich, J.M. Broto, A. Fert, F. Dau, and F. Petroff. Giant Magnetoresistance of (001)Fe/(001)Cr Magnetic Superlattices. *Physical Review Letters*, 61:2472, 1988.

[7] S. S. P. Parkin. The magic of magnetic multilayers. *IBM Journal of Research and Development*, 42(1):3–6, 1998.

[8] G.A. Prinz. Magnetoelectronics applications. *J. Magn. Magn. Mater.*, 200:57, 1999.

[9] MM Miller, GA Prinz, P. Lubitz, L. Hoines, JJ Krebs, SF Cheng, and FG Parsons. Novel absolute linear displacement sensor utilizing giant magnetoresistance elements. *Journal of Applied Physics*, 81:4284, 1997.

[10] AE Berkowitz, JR Mitchell, MJ Carey, AP Young, S. Zhang, FE Spada, FT Parker, A. Hutten, and G. Thomas. Giant magnetoresistance in heterogeneous Cu-Co alloys. *Physical Review Letters*, 68(25):3745–3748, 1992.

[11] J.Q. Xiao, J.S. Jiang, and CL Chien. Giant magnetoresistance in nonmultilayer magnetic systems. *Physical Review Letters*, 68(25):3749–3752, 1992.

[12] M. Jullière. Tunneling between ferromagnetic films. *Physical Letters*, 54:225, 1975.

[13] J.S. Moodera, L.R. Kinder, T.M. Wong, and R. Meservey. Large Magnetoresistance at Room Temperature in Ferromagnetic Thin Film Tunnel Junctions. *Physical Review Letters*, 74:3273, 1995.

[14] T. Miyazaki and N. Tezuka. Giant magnetic tunneling effect in Fe/Al_2O_3/Fe junctions. *J. Magn. Magn. Mater.*, 139:L231, 1995.

[15] D. Wang, C. Nordman, J.M. Daughton, Z. Qian, and J. Fink. 70% TMR at room temperature for SDT sandwich junctions with CoFeB as free and reference Layers. *Magnetics, IEEE Transactions on*, 40:2269– 2271, 2004.

[16] I. Niarchos D. Christodoulidis Y. Zhang Y. Stavroyiannis, S. Panagiotopoulos and G. C. Hadjipanayis. New copt/ag films for high density recording media. *Journal of Applied Physics*, 85:4304–4306, 1999.

[17] Y. Moser A. Weller D. Yu, M. Liu and D. J. Sellmyer. Nanocomposite copt:c films for extremmely high density recording media. *Applied Physics Letters*, 75(25):3992–3994, 1999.

[18] M. Taga Y. Morikawa, T. Suzuki. Soft magnetic properties of co-cr-o granular films. *Journal of Applied Physics*, 83:6664–6666, 1998.

[19] S.S.P. Parkin, C. Kaiser, A. Panchula, P.M. Rice, B. Hughes, M. Samant, and S.H. Yang. Giant tunnelling magnetoresistance at room temperature with MgO (100) tunnel barriers. *Nature Materials*, 3(12):862–867, 2004.

[20] S. Yuasa, T. Nagahama, A. Fukushima, Y. Suzuki, and K. Ando. Giant room-temperature magnetoresistance in single-crystal Fe/MgO/Fe magnetic tunnel junctions. *Nature Materials*, 3(12):868–871, 2004.

[21] Y.M. Lee, J. Hayakawa, S. Ikeda, F. Matsukura, and H. Ohno. Effect of electrode composition on the tunnel magnetoresistance of pseudo-spin-valve magnetic tunnel junction with a MgO tunnel barrier. *Applied . Physcs Letters.*, 90:212507, 2007.

[22] J.S. Moodera, E.F. Gallagher, K. Robinson, and J. Nowak. Optimum tunnel barrier in ferromagnetic–insulator–ferromagnetic tunneling structures. *Applied Physics Letters*, 70:3050, 1997.

[23] T. Mitsuzuka, K. Matsuda, A. Kamijo, and H. Tsuge. Interface structures and magnetoresistance in magnetic tunnel junctions. *Journal of Applied Physics*, 85:5807, 1999.

[24] C. Yoshida, H. Noshiro, Y. Yamazaki, T. Iizuka, Y. Stoh, M. Aoki, S. Umehara, M. Satoh, and K. Kobayashi. Reliability of MgO tunneling barrier for MRAM device. In *IEEE International Reliability Physics Symposium Proceedings, 2006. 44th Annual.*, pages 697–698, 2006.

[25] P.W. Selwood. *Magnetochemistry*. Swinburne Press, 2008.

[26] D.R. Inglis. Energy Relations in Complex Spectra. *Physical Review*, 38(5):862–872, 1931.

[27] K. Scroerder. *Magnetism in Atoms*. 36 Spring school. Institute of Solid State Research, Forschungszentrum Jülich GmbH, 2005.

[28] G.A. Prinz. Magnetoelectronics. *Science*, 282(5394):1660, 1998.

[29] W. Thomson. On the electro-dynamic qualities of metals:–effects of magnetization on the electric conductivity of nickel and of iron. *Proceedings of the Royal Society of London*, 8:546–550, 1856.

[30] PM Tedrow and R. Meservey. Spin-dependent tunneling into ferromagnetic nickel. *Physical Review Letters*, 26(4):192–195, 1971.

[31] P.M. Tedrow and R. Meservey. Spin Polarization of Electrons Tunneling from Films of Fe, Co, Ni, and Gd. *Phys. Rev. B*, 7:318, 1973.

[32] R. Meservey, PM Tedrow, and P. Fulde. Magnetic field splitting of the quasiparticle states in superconducting aluminum films. *Physical Review Letters*, 25(18):1270–1272, 1970.

[33] P. Fulde. High field superconductivity in thin films. *Advances in Physics*, 22(6):667–719, 1973.

[34] T. McGuire and R. Potter. Anisotropic magnetoresistance in ferromagnetic 3d alloys. *IEEE Transactions on Magnetics*, 11(4):1018–1038, 1975.

[35] PA Grünberg. Exchange anisotropy, interlayer exchange coupling and GMR in research and application. *Sensors & Actuators: A. Physical*, 91(1-2):153–160, 2001.

[36] SSP Parkin, R. Bhadra, and KP Roche. Oscillatory magnetic exchange coupling through thin copper layers. *Physical Review Letters*, 66(16):2152–2155, 1991.

[37] WP Pratt Jr, S.F. Lee, JM Slaughter, R. Loloee, PA Schroeder, and J. Bass. Perpendicular giant magnetoresistances of Ag/Co multilayers. *Physical Review Letters*, 66(23):3060–3063, 1991.

[38] A. Chaiken, GA Prinz, and JJ Krebs. Magnetotransport study of Fe-Cr-Fe sandwiches grown on ZnSe (100). *Journal of Applied Physics*, 67:4892, 1990.

[39] M. T. Johnson, S. T. Purcell, N. W. E. McGee, R. Coehoorn, J. aan de Stegge, and W. Hoving. Structural dependence of the oscillatory exchange interaction across cu layers. *Physical Review Letters*, 68(17):2688–2691, Apr 1992.

[40] Eric E. Fullerton, David M. Kelly, J. Guimpel, Ivan K. Schuller, and Y. Bruynseraede. Roughness and giant magnetoresistance in fe/cr superlattices. *Physical Review Letters*, 68(6):859–862, Feb 1992.

[41] F. Tsui, Baoxing Chen, D. Barlett, Roy Clarke, and C. Uher. Scaling behavior of giant magnetotransport effects in co/cu superlattices. *Physical Review Letters*, 72(5):740–743, Jan 1994.

[42] B. Dieny, VS Speriosu, SSP Parkin, BA Gurney, DR Wilhoit, and D. Mauri. Giant magnetoresistive in soft ferromagnetic multilayers. *Physical Review B*, 43(1):1297–1300, 1991.

[43] A. Camley R. E. Grünberg P. Barna, J. Fuss and W. Zinn. Novel magnetoresistance effect in layered magnetic structures: Theory and experiment. *Phys. Rev. B*, 42(13):8110–8120, Nov 1990.

[44] CL Chien. Magnetism and Giant Magnetotransport Properties in Granular Solids. *Annual Review of Materials Science*, 25:129–160, 1995.

[45] H. Zabel and S. D. Badar. *Magnetic Heterostructures*. Springer, Berlin, 2008.

[46] W.H. Butler, X.-G. Zhang, T.C. Schulthess, and J.M. MacLaren. Spindependant tunneling conductance of fe/mgo/fe sandwiches. *Phys. Rev. B*, 63:054416, 2001.

[47] T. Nagahama, S. Yuasa, E. Tamura, and Y. Suzuki. Spin-dependent tunneling in magnetic tunnel junctions with a layered antiferromagnetic cr(001) spacer: Role of band structure and interface scattering. *Physical Review Letters*, 95(8):086602, Aug 2005.

[48] Roger W. Cohen and B. Abeles. Superconductivity in granular aluminum films. *Phys. Rev.*, 168(2):444–450, Apr 1968.

[49] Ping Sheng, B. Abeles, and Y. Arie. Hopping conductivity in granular metals. *Physical Review Letters*, 31(1):44–47, Jul 1973.

[50] N. F. Moot and E. A. Davis. *Electron processes in non crystalline materials* . Clarendon press, Oxford, 1979.

[51] AL Efros and BI Shklovskii. Coulomb gap and low temperature conductivity of disordered systems. *J. Phys. C*, 8, 1975.

[52] J. Schotter. *Development of a magnetoresistive biosensor for the detection of biomolecules*. Universität Bielefeld, Doctoral thesis, 2004.

[53] V. Hñink. *Exchange Bias und Ionenbestrahlung in magnetischen Tunnelelementen*. Universität Bielefeld, Diplomarbeit in Physik, 2003.

[54] S. Kämmerer. *The Heusler alloy Co2MnSi in thin films*. Universität Bielefeld, Doctoral thesis, 2004.

[55] R.A. Faction. Britannica Encyclopedia Online, 2008.

[56] A. Thomas. *Preparation and Characterisation of magnetic single and double barrier junctions*. Universität Bielefeld, Diss., 2003.

[57] V. Drewello. *Untersuchung der Spinpolarisation von 3d-Ferromagneten in MgO Tunnelsystemen*. Universität Bielefeld, Diplomarbeit in Physik, 2006.

[58] O. Schebaum. *Direkte Messung der Spinpolarization mit der Meservey-Tedrow Methode*. Universität Bielefeld, Diplomarbeit in Physik, 2007.

[59] M. Sacher. *Präparation und Charakterisierung von Mehrfachbarrieren magnetischer Tunnelelemente*. Universität Bielefeld, Diplomarbeit in Physik, 2002.

[60] B. Seeber. *Handbook of applied superconductivity*. Inst of Physics Pub Inc, 1998.

[61] S.D. Jackson and J.S.J. Hargreaves. *Metal oxide catalysis*. Vch Pub, 2008.

[62] B. Fultz and J.M. Howe. *Transmission electron microscopy and diffractometry of materials*. Springer Verlag, 2007.

[63] I. Ennen. *Magnetische Nanopartikel als Bausteine füur granulare Systeme: Mikrostruktur, Magnetismus und Transporteigenschaften* . Universität Bielefeld, Diplomarbeit in Physik, 2007.

[64] D.A. Bonnell. *Scanning probe microscopy and spectroscopy: theory, techniques, and applications*. Wiley-VCH, 2001.

[65] T.W. Kelley, E.L. Granstrom, and C.D. Frisbie. Conducting Probe Atomic Force Microscopy: A Characterization Tool for Molecular Electronics. *Advanced Materials*, 11(3):261–264, 1999.

[66] KM Bhutta, J. Schmalhorst, and G. Reiss. Study of MgO tunnel barriers with conducting atomic force microscopy. *Journal of Magnetism and Magnetic Materials*, 2009.

[67] S. Araki, K. SATO, T. KAGAMI, S. SARUKI, T. UESUGI, N. KASAHARA, T. KUWASHIMA, N. OHTA, J. Sun, K. NAGAI, et al. Fabrication and electric properties of lapped type of TMR heads for 50 Gb/in? 2 ? and beyond. *IEEE transactions on magnetics*, 38(1):72–77, 2002.

[68] A. Tanaka, Y. Shimizu, Y. Seyama, K. Nagasaka, R. Kondo, H. Oshima, S. Eguchi, and H. Kanai. Spin-valve heads in the current-perpendicular-to-plane mode for ultrahigh-density. recording. *IEEE Transactions on Magnetics*, 38(1 Part 1):84–88, 2002.

[69] M. Takagishi, K. Koi, M. Yoshikawa, T. Funayama, H. Iwasaki, and M. Sahashi. The applicability of CPP-GMR heads for magnetic recording. *IEEE Transactions on Magnetics*, 38(5 Part 1):2277–2282, 2002.

[70] J. Mathon and A. Umerski. Theory of tunneling magnetoresistance of an epitaxial fe/mgo/fe(001) junction. *Phys. Rev. B*, 63:220403, 2001.

[71] X.-G. Zhang and W. H. Butler. Large magnetoresistance in bcc co/mgo/co and feco/mgo/feco tunnel junctions. *Phys. Rev. B*, 70(17):172407, Nov 2004.

[72] J. Faure-Vincent, C. Tiusan, E. Jouguelet, F. Canet, M. Sajieddine, C. Bellouard, E. Popova, M. Hehn, F. Montaigne, and A. Schuhl. High tunnel magnetoresistance in epitaxial fe/mgo/fe tunnel junctions. *Applied Physics Letters*, 82(25):4507–4509, 2003.

[73] Shinji Yuasa, Akio Fukushima, Taro Nagahama, Koji Ando, and Yoshishige Suzuki. High tunnel magnetoresistance at room temperature in fully epitaxial fe/mgo/fe tun-

nel junctions due to coherent spin-polarized tunneling. *Japanese Journal of Applied Physics*, 43(4B):L588–L590, 2004.

[74] J. C. Read, P. G. Mather, and R. A. Buhrman. X-ray photoemission study of cofeb/mgo thin film bilayers. *Applied Physics Letters*, 90(13):132503, 2007.

[75] S. Hufner. *Photoelectron Spectroscopy*. Springer-Verlag, Berlin, Heidelberg.

[76] R. Schad, D. Allen, G. Zangari, I. Zana, D. Yang, M. Tondra, and D. Wang. Pinhole analysis in magnetic tunnel junctions. *Applied Physics Letters*, 76:607, 2000.

[77] B. J. Jönsson-Åkerman, R. Escudero, C. Leighton, S. Kim, Ivan K. Schuller, and D. A. Rabson. Reliability of normal-state current–voltage characteristics as an indicator of tunnel-junction barrier quality. *Applied Physics Letters*, 77(12):1870–1872, 2000.

[78] Johan J. Åkerman, J. M. Slaughter, Renu Whig Dave, and Ivan K. Schuller. Tunneling criteria for magnetic-insulator-magnetic structures. *Applied Physics Letters*, 79(19):3104–3106, 2001.

[79] Bryan Oliver, Qing He, Xuefei Tang, and Janusz Nowak. Tunneling criteria and breakdown for low resistive magnetic tunnel junctions. *Journal of Applied Physics*, 94(3):1783–1786, 2003.

[80] J. Ventura, J. M. Teixeira, J. P. Araujo, J. B. Sousa, P. Wisniowski, and P. P. Freitas. Pinholes in thin low resistance mgo-based magnetic tunnel junctions probed by temperature dependent transport measurements. volume 103, page 07A909. AIP, 2008.

[81] A. Olbrich, B. Ebersberger, C. Boit, J. Vancea, H. Hoffmann, H. Altmann, G. Gieres, and J. Wecker. Oxide thickness mapping of ultrathin AlO at nanometer scale with conducting atomic force microscopy. *Applied Physics Letters*, 78:2934, 2001.

[82] KM Lang, DA Hite, RW Simmonds, R. McDermott, DP Pappas, and J.M. Martinis. Conducting atomic force microscopy for nanoscale tunnel barrier characterization. *Review of Scientific Instruments*, 75:2726, 2004.

[83] F. Houze, R. Meyer, O. Schneegans, and L. Boyer. Imaging the local electrical properties of metal surfaces by atomic force microscopy with conducting probes. *Applied Physics Letters*, 69:1975, 1996.

[84] EZ Luo, JX Ma, JB Xu, IH Wilson, AB Pakhomov, and X. Yan. Probing the conducting paths in a metal-insulator composite by conducting atomic force microscopy. *JOURNAL OF PHYSICS-LONDON-D APPLIED PHYSICS*, 29:3169–3172, 1996.

[85] K L Johnson. One hundred years of hertz contac. *Proc. Inst. Mech. Eng*, 196:363, 1982.

[86] D. H Chung. Elastic Moduli of Single-Crystal and Polycrystalline Magnesium Oxide. *Phil. Mag.*, 8:833, 1963.

[87] JG Park, SH Lee, B. Kim, and YW Park. Electrical resistivity of polypyrrole nanotube measured by conductive scanning probe microscope: The role of contact force. *Applied Physics Letters*, 81:4625, 2002.

[88] E. Meyer. *Nanoscience: friction and rheology on the nanometer scale*. World Scientific Pub Co Inc, 2002.

[89] F. Bardou. Rare events in quantum tunneling. *Europhysics letters*, 39(3):239–244, 1997.

[90] V. Da Costa, C. Tiusan, T. Dimopoulos, and K. Ounadjela. Tunneling Phenomena as a Probe to Investigate Atomic Scale Fluctuations in Metal/Oxide/Metal Magnetic Tunnel Junctions. *Physical Review Letters*, 85(4):876–879, 2000.

[91] CY Chou, YD Yao, PC Kuo, KW Cheng, C. Yu, and SC Chen. Microstructure and magnetoresistance of MgO thin film with CoFeB and CoFeC underlayers. *Journal of Magnetism and Magnetic Materials*, 310(2P3):2245–2247, 2007.

[92] GR Harp and SSP Parkin. Epitaxial growth of metals by sputter deposition. *Thin Solid Films*, 288(1-2):315–324, 1996.

[93] TE Schlesinger, RC Cammarata, A. Gavrin, J.Q. Xiao, CL Chien, MK Ferber, and C. Hayzelden. Enhanced mechanical and magnetic properties of granular metal thin films. *Journal of Applied Physics*, 70:3275, 1991.

[94] B. Dieny, S. Sankar, M. R. McCartney, D. J. Smith, P. Bayle-Guillemaud, and A. E. Berkowitz. Spin-dependent tunneling in discontinuous metal/insulator multilayers. *Journal of Magnetism and Magnetic Materials*, 185(3):283 – 292, 1998.

[95] DM Schaadt, ET Yu, S. Sankar, and AE Berkowitz. Charge storage in Co nanoclusters embedded in SiO by scanning force microscopy. *Applied Physics Letters*, 74:472, 1999.

[96] YW Du, H. Sang, QY Xu, WN Wang, and SY Zhang. Intergranule interaction in magnetic granular films. *Materials Science & Engineering A*, 286(1):58–64, 2000.

[97] S. Mitani, H. Fujimori, and S. Ohnuma. Temperature dependence of tunnel-type gmr in insulating granular systems. *Journal of Magnetism and Magnetic Materials*, 177-181(Part 2):919 – 920, 1998. International Conference on Magnetism (Part II).

[98] A. Gerber, A. Milner, G. Deutscher, M. Karpovsky, and A. Gladkikh. Insulator-superconductor transition in 3D granular Al-Ge films. *Physical Review Letters*, 78(22):4277–4280, 1997.

[99] S. Honda, T. Okada, and M. Nawate. Tunneling giant magnetoresistance in Fe-SiO 2 multilayered and alloyed films. *J Magn Magn Mater*, 165(1):153–156, 1997.

[100] T. Furubayashi and I. Nakatani. Giant magnetoresistance in granular Fe–MgF films. *Journal of Applied Physics*, 79:6258, 1996.

[101] Y.E. Kalinin, AV Sitnikov, OV Stognei, IV Zolotukhin, and PV Neretin. Electrical properties and giant magnetoresistance of the CoFeB–SiO2 amorphous granular composites. *Materials Science & Engineering A*, 304:941–945, 2001.

[102] M. Li, J. Shi, Y. Nakamura, and R. Yu. Magnetoresistance of nanocrystalline Co-AlN films. *Applied Physics A: Materials Science & Processing*, 89(3):807–812, 2007.

[103] Sonja. Heitmann. *Cobalt/Copper Multilayers: Interplay of Microstructure and GMR and Recrystallization as the Key Towards Temperature Stability*. Universität Bielefeld, Diss., 2004.

[104] S. Sankar, A. E. Berkowitz, and David J. Smith. Spin-dependent transport of $co-sio2$ granular films approaching percolation. *Phys. Rev. B*, 62(21):14273–14278, 2000.

[105] X. Batlle, V. Franco, A. Labarta, and K. O'Grady. Remanence breakdown in granular alloys at magnetic percolation. *Journal of Applied Physics*, 88(3):1576–1582, 2000.

[106] S R. Teixeira, B. Dieny, A. Chamberod, C. Cowache, S. Auffret, P. Auric, J L. Rouviere, O. Redon, and J. Pierre. Giant magnetoresistance in sputtered $(co_{70}fe_{30})_x ag_{1-x}$ heterogeneous alloys. *Journal of Physics: Condensed Matter*, 6:5545–5560, 1994.

[107] Scott Kirkpatrick. Percolation and conduction. *Rev. Mod. Phys.*, 45(4):574–588, Oct 1973.

[108] X. Batlle and A. Labarta. Finite-size effects in fine particles: magnetic and transport properties. *JOURNAL OF PHYSICS-LONDON-D APPLIED PHYSICS*, 35(6):15–42, 2002.

[109] B. Abeles, Ping Sheng, M. D. Coutts, and Y. Arie. Structural and electrical properties of granular metal films. *Advances in Physics*, 24:407–461, 1975.

[110] Esther M. Conwell. Impurity band conduction in germanium and silicon. *Phys. Rev.*, 103:51–61, Jul 1956.

[111] NF Mott. On the transition to metallic conduction in semiconductors. *Canadian Journal of Physics*, 34(12A):1356–1368, 1956.

[112] JMD Coey. Viret M., von Molnar S. *Adv. Phys*, 48(2):167–293, 1999.

[113] BI Shklovskii and AL Efros. Electronic properties of doped semiconductors (Russian book). *Moscow, Izdatel'stvo Nauka, 1979. 416 p, In Russian*, 1979.

[114] S. Mitani, S. Takahashi, K. Takanashi, K. Yakushiji, S. Maekawa, and H. Fujimori. Enhanced magnetoresistance in insulating granular systems: Evidence for higher-order tunneling. *Physical Review Letters*, 81(13):2799–2802, 1998.

[115] A. Frydman and RC Dynes. Magnetoresistance of granular ferromagnets-observation of a magnetic proximity effect? *Arxiv preprint cond-mat/9810061*, 1998.

[116] BAI Haili and JIANG. Enyong. Tunnel magnetoresistance (TMR) in ferromagnetic metal insulator granular films . *Chinese Science Bulletin*, 46(9):529–537, 2001.

[117] J. Inoue and S. Maekawa. Theory of tunneling magnetoresistance in granular magnetic films. *Physical Review B*, 53(18):11927–11929, 1996.

[118] S. Mitani, H. Fujimori, K. Takanashi, K. Yakushiji, J. G. Ha, S. Takahashi, S. Maekawa, S. Ohnuma, N. Kobayashi, T. Masumoto, M. Ohnuma, and K. Hono. Tunnel-mr and spin electronics in metal-nonmetal granular systems. *Journal of Magnetism and Magnetic Materials*, 198-199:179 – 184, 1999.

[119] T. Zhu and Y. J. Wang. Enhanced tunneling magnetoresistance of $Fe-Al_2O_3$ granular films in the Coulomb blockade regime. *Phys. Rev. B*, 60(17):11918–11921, 1999.

[120] J. Unguris, RJ Celotta, and DT Pierce. Observation of two different oscillation periods in the exchange coupling of Fe/Cr/Fe (100). *Physical Review Letters*, 67(1):140–143, 1991.

[121] PV Paluskar, JJ Attema, GA de Wijs, S. Fiddy, E. Snoeck, JT Kohlhepp, HJM Swagten, RA de Groot, and B. Koopmans. Spin tunneling in junctions with disordered ferromagnets. *Physical Review Letters*, 100(5):57205, 2008.

[122] I. Shlimak, M. Kaveh, R. Ussyshkin, V. Ginodman, SD Baranovskii, P. Thomas, H. Vaupel, and RW Van der Heijden. Temperature-induced smearing of the Coulomb gap: Experiment and computer simulation. *Physical review letters*, 75(26):4764–4767, 1995.

[123] F. Bensmina, P. Humbert, A. Dinia, D. Muller, V. S. Speriosu, and B. A. Gurney. Annealing effect on the magnetic properties of Ta 50 Å/Cu 50 Å/Co 75 Å/Cu 50 Å/Ta 50 Å sandwiches. *Journal of Magnetism and Magnetic Materials*, 198-199:338 – 340, 1999.

[124] T. Dimopoulos, G. Gieres, J. Wecker, N. Wiese, and MD Sacher. Thermal annealing of junctions with amorphous and polycrystalline ferromagnetic electrodes. *Journal of Applied Physics*, 96:6382, 2004.

[125] S. Ikeda, J. Hayakawa, Y.M. Lee, F. Matsukura, and H. Ohno. Dependence of tunnel magnetoresistance on ferromagnetic electrode materials in MgO-barrier magnetic tunnel junctions. *Journal of Magnetism and Magnetic Materials*, 310(2P3):1937–1939, 2007.

Acknowledgement

All recommendations to Almighty Allah who imparted me the resoluteness and fortitude for the accomplishment of this thesis, I also offer the sincerest and the humlest words of thanks to His Messenger Muhammad (Peace Be Upon Him), who is forever a source of guidance and knowledge for humanity.

At the first place I would like to express my deepest gratitude and obligation to Prof. Dr. Günter Reiss for his supervision, advice and guidance from the early stage of my research and giving me extraordinary attention and confidence throughout my work. In addition, he was always accessible and willing to help me in my research. I learnt true scientific attitude, patience and determination in research from him. I will definitely benefit from this learning throughout my research career.

I gratefully acknowledge Dr. Jan Schmallhorst for his advice and valuable contribution to my work. His involvement in my work with his intellectual maturity and originality was very helpful for shaping up my ideas and improving the quality of my work.

I acknowledge the support of Patrik Thomas and Britta Vogel for X-ray Reflectometery (XRR) and Alternating Gradient Magnetometery (AGM) measurements. I am thankful to Henning Schuhmann from Georg-August-Universität Göttingen for providing me HRTEM images of my samples on priority basis and Syed Rizwan Ali from RWTH Aachan University for providing me Superconducting Quantum Interference Device (SQUID) results. I am also very grateful to Assad Farooq from Technical University Dresden and Malik Shahzad from Technical University Clausthal for their encouragement and guidance at all stages of my work and A. G. Venkatesh for editing my thesis.

I also acknowledge the Higher Education Commission of Pakistan for providing financial support and Deutscher Akademischer Austauschdienst for administrative support.

I wish to express my love and gratitude to my sons Ahmad Hassan and Muhammad Umer who sacrificed my presence during my stay in Bielefeld, Germany. Finally, I am indebted to my mother and my wife whose moral support, exemplary patience and prayers have sustained me to complete this work.